^{236}U in-situ production in High-Grade Mineralization at Cigar Lake, Athabasca Basin, Northern Saskatchewan

Maria Stefanescu

Thesis submitted to the Faculty of Graduate and Postdoctoral Studies in partial fulfillment of the requirements for the degree of Master's in Earth Sciences

Ottawa-Carleton Geoscience Centre
Department of Earth
Sciences Faculty of Science
University of Ottawa

Abstract

Canada accounts for 15% of the world's uranium production (World Nuclear Association). The Athabasca Basin in northern Saskatchewan Canada contains a number of high grade, uranium ore deposits which occur at, or immediately below, an unconformity between Archean and Paleoproterozoic metasediments and intrusive rocks and overlying Proterozoic sandstones. The uranium ores are largely composed of high concentrations of uraninite and Pitchblende with naturally occurring $^{238}U/^{235}U$ ratios. U-236 (*half-life of 23.42 Myr*) will be produced when ^{235}U absorbs a neutron and the nucleus does not fission. Because it is so long lived, a small amount ^{236}U can be maintained at equilibrium levels in the natural uranium ores.

One of the main questions of this research is whether or not these equilibrium levels reflect higher grades or larger amounts of uranium minerals as a result of elevated neutron fluxes from ^{238}U and subsequent neutron absorption on ^{235}U. As well, are there other elements within the system that will absorb these neutrons, thereby reducing that which will impinge on ^{235}U. In this study, we have estimated the amount of ^{236}U that is produced by calculating the neutron flux from uranium and evaluating the effects of spatially related elements such as B, Sm and Gd using their elemental neutron cross-sections and abundances.

In this project we have calculated and simulated theoretically the production of ^{236}U and then test the theoretical calculations using measurements of uranium isotopes by accelerator mass spectrometry (AMS). Once we understand the factors controlling the ^{236}U concentration, we hypothesize that the relationship between ^{236}U and ^{238}U can be used as a geochemical vector within uranium exploration, with the equilibrium level possibly distinguishing between primary mineralization and remobilization and reprecipitation of this U within spatially associated secondary U mineralization.

Résumé

Le Canada représente 15% de la production mondiale d'uranium (World Nuclear Association). Le bassin de l'Athabasca, dans le nord de la Saskatchewan, contient un certain nombre de gisements uranifères de haute teneur qui se trouvent à ou bien immédiatement en dessous d'une discordance entre des métasédiments archéens et paléoprotérozoïques et des roches intrusives et des grès protérozoïques sus-jacents. Les minerais d'uranium sont en grande partie composés de fortes concentrations d'uraninite et de Pitchblende avec des rapports naturels $^{238}U/^{235}U$. L'^{236}U (*demi-vie de 23,42 Ma*) sera produite lorsque l'^{235}U absorbera un neutron et que le noyau ne fissionnera pas. En raison de sa longue durée de vie, une petite quantité d'^{236}U va être maintenue à des niveaux d'équilibre dans les minerais d'uranium naturel.

Une des principales questions de cette recherche est de savoir si ces niveaux d'équilibre reflètent des teneurs plus élevées ou des quantités plus importantes de minéraux d'uranium en raison des flux neutroniques élevés due à l'^{238}U et de l'absorption subséquente de neutrons par l'^{235}U. De plus, y a-t-il d'autres éléments dans le système qui absorberont ces neutrons, réduisant ainsi ce qui affectera l'^{235}U?
Dans cette étude, nous avons estimé la quantité d'^{236}U produite en calculant le flux neutronique et en évaluant les effets d'éléments spatialement liés à l'absorption de neutron tels que B, Sm et Gd, utilisant leurs sections-neutroniques élémentaires et leurs abondances.

Ce projet a permis de calculer et de simuler théoriquement la production d'^{236}U, puis de tester ces calculs théoriques en utilisant des mesures d'isotopes d'uranium par spectrométrie de masse par accélérateur (AMS). Une fois les facteurs contrôlant la concentration d'^{236}U compris, nous supposons que la relation entre ^{236}U et ^{238}U peut être utilisée comme vecteur géochimique dans l'exploration uranifère, distinguant éventuellement la minéralisation primaire de la remobilisation et reprécipitation de l'uranium.

Acknowledgements:

I would like to dedicate this work to Dr. Jack Cornett, my supervisor at the University of Ottawa. Thank you for believing in me and never giving up on me. I will never be able to formulate in enough words the gratitude I have for having been able to work with you. Thank you for your dedication, support and for always being there in time of need.

Many thanks to Tom Kotzer for his expertise, time and curiosity making this project possible. A special thanks goes to the marvelous group at Cameco Cigar Lake for their help and access to more information and samples then one could hope for; and to the SRC team for their fast analysis.

This project would not have been possible without the help of the A. E. Lalonde AMS lab team, particularly Dr. Xiaolei Zhao. I would also like to thank the amazing team of the Earth Science department that rallied together in the saddest of moments to bring this project to its end especially Zakir Kazi and Barbara Francisco.

Last but not least, thank you to my family and friends for understanding the frustrations and euphoria that came with the completion of this project but especially my dad, that dedicated time and effort into reading and trying to understand a thesis very far from this field of study.

Table of Contents

^{236}U in-situ production in High-Grade Mineralization at Cigar Lake, Athabasca Basin, Northern Saskatchewan i

Abstract ii

Résumé iii

Acknowledgements: iv

Liste of Figures vii

Liste of Tables xi

1. Introduction 1

2 Concepts and Definitions 7

2.1 Radioactive decay 7
2.2 Half-life and Decay constant 9
2.3 Nuclide 10
2.4 Isotopes 10
2.5 Nuclear reactions 10
2.6 Reaction Cross-Section 11
2.7 Macroscopic Cross-Section 11
2.8 Particle flux 11
2.9 Neutron capture and thermal neutrons. 12
2.10 The decay chains 12
2.11 Coulomb explosion 13

3. A model of ^{236}U production and distribution 14

3.1 The sources of neutrons in the system 15
3.1.1 Alpha - neutron reaction (α,n) 17
3.1.2 Fission 17
3.2 Neutron production rate 19
3.3 The main neutron absorbers 20
3.4 Calculating the neutron flux 21
3.5 The prediction model and production of ^{236}U 22

4 Accelerator mass spectrometer (AMS) 25

4.1 Sample preparation 26
4.1.1 Sample assessments and separation 26
4.1.2 Uranium extraction 27
4.1.3 Column separation 27
4.1.4 AMS Targets 29
4.1.5 Standards and blanks 30
4.2 The AMS set-up and how it works 31
4.3 Sample analyses and machine parameters setup 34
4.3.1 Issues and problems 37
4.4 Calibration and data processing 41
4.5 Determining the concentration of ^{236}U (atoms/g), (pg/kg) and the ^{236}U/^{238}U ratio from the counts given by the AMS 44

4.5.1 Method 1: using ^{233}U and ^{236}U counts ... *44*
4.5.2 Method 2: using $^{236}U/^{238}U$ ratio measured with the AMS ... *46*
4.5.3 Prepared Standards ... *48*

5 The Geology ... **49**
5.1 Regional Geology ... 50
5.1.1 The Basement ... *50*
5.1.2 Basin Geology ... *54*
5.2 Local geology ... 54
5.3 Alterations ... 56
5.3.1 The basement ... *56*
5.3.2 The basin ... *58*
5.4 The deposit ... 59
5.5 Main Minerals and origin of Boron, Samarium and Gadolinium ... 62
5.6 Location of samples collected ... 63

6 Elemental composition and testing the Prediction Model ... **65**
6.1 Elemental composition and statistical distribution ... 65
6.2 Elemental correlation ... 67
6.2.1 Individual regression between B and U, Sm and U and Gd and U ... *67*
6.2.2 Simultaneous regression of B, Sm and Gd on U ... *70*
6.2.3 Paired regression on U ... *70*
6.2.4 Fission products ... *70*
6.3 Results of the model ... 71
6.3.1 ^{236}U results ... *71*
6.3.2 The $^{236}U/^{238}U$ ratio results ... *72*
6.3.3 Correlation between $^{236}U/^{238}U$ atom/atom ratio and the absorbers B, Sm, Gd ... *73*
6.4 Error sensitivity ... 76
6.4.1 5% error in the B concentration ... *76*
6.4.2 5% error in the Sm concentration ... *79*
6.4.3 5% error in the Gd concentration ... *82*
6.4.4 5% error in the U concentration ... *85*
6.5 Conclusions regarding the model ... 88

7 Results of AMS Measurements ... **90**
7.1 Range of the results ... 91
7.2 Comparison to other measurements ... 92
7.3 The AMS results ... 93
7.4 Conclusions from the AMS measurements ... 96

8 Discussion ... **98**
8.1 Results of AMS measurements versus the prediction model ... 98

9 Conclusion ... **123**

Annex A: $^{236}U/^{238}U$ found in literature ... **127**

Annex B: Elemental composition and analyses ... **128**

Annex C : Tunning setup ... **137**

References ... **138**

Liste of Figures

Figure 1.1 Representing the range of $^{236}U/^{238}U$ atom/atom ratio as found in previous studies. Note the logarithmic scale. A table of the data can be found in Annex A 4
Figure 2.1: Distribution of induced fission fragments of ^{238}U (U-238 NF) and ^{235}U (U-235 NF) and spontaneous fission fragments of ^{238}U (U-238 SF) done using the JAEA Nuclear Data Center plotting tool..... 9
Figure 2.2: The three natural occurring decay chains ^{232}Th, ^{235}U and ^{238}U.....13
Figure 3.1: Neutron production profile in High Ca-granite taken from Fabryka-Martin, 1988. It shows the processes by which neutrons are produced in meters of water equivalent (mwe). Depth in mwe is a normalized way of expressing depth independent of rock density and is conveyed as $\boldsymbol{dmwe} = \boldsymbol{h}(\boldsymbol{\rho r}\boldsymbol{\rho w})$ where h is the absolute depth in meters, $\boldsymbol{\rho r}$ is the average bulk density of the overlying rock (g cm-3) at depth and $\boldsymbol{\rho w}$is the density of water (1g cm-3). At Cigar Lake, the average bulk density is between 2.5g cm-3 for minerals not containing U ore and 7.5 g cm-3 for ore (Fabryka-Martin et al., 1994), hence, below 30m, only fission and (α,n) reactions produce neutrons. .16
Figure 3.2 ^{238}U generalized spontaneous fission 17
Figure 3.3: the ^{235}U neutron-induced fission.....18
Figure 3.4 Fission Cross-Sections for neutron induced fission created using https://www-nds.iaea.org/exfor/endf.htm using the ENDF/B-VII.1 database and modified. 19
Figure 3.5: Neutron Cross-Sections of the major neutron absorbing elements. Created using https://www-nds.iaea.org/exfor/endf.htm using the JEFF-3.2 database and modified. 21
Figure 3.6: Template of the model made in excel. 24
Figure 4.1: Diagram from Horowitz et al., 1992. The left diagram shows the high absorption of U(VI) by NHO_3 at 4M and above. The second diagram depicts the relationship of HCl with the column and the elements. A 4-6M HCl solution allows the selective elution of Thorium (Th) from the resin once the sample has been loaded. A low molarity of HCl allows the elution of U. 29
Figure 4.2: Overview of the AEL-AMS (modified from Kieser et al. 2015).....32
Figure 4.3: Diagram showing the different elements of the EAL-AMS. 36
Figure 4.4: Summary of the high energy ESA performances for $^{236}UO^- \rightarrow {}^{236}U^{+3}$.....38
Figure 4.5 Typical current of ^{238}U for different samples 39
Figure 4.6: Comparison of Ta and Si for boosting UO^- current (Zhao, 2016) 40
Figure 4.7: Comparisons of different powders for boosting UO^- current (Zhao, 2016) 41
Figure 4.8: $^{236}U/^{233}U$ atom-to-atom ratio measured versus expected 48
Figure 5.1 Map of Canada with the location of the Athabasca Basin and Cigar Lake. Taken from Farquharson and Craven, (2009). The dark square is the Athabasca Basin and the star is the location of the Cigar Lake ore deposit.....50

Figure 5.2: Major subdivisions of the exposed Precambrian shield in northern Saskatchewan and Alberta. (Card et al., 2007) 51
Figure 5.3: Geology and structures of the Athabasca Basin (modified from Jefferson et al.,2007), include the A-A' cross-section of figure 4.4 Legend C=Carswell, D=Douglas, FP=Fair Point, LL=Locker Lake, LZ=Lazenby Lake, MF=Manitou Falls (members: b=Bird (l=lower, u=upper) c=Collins, d=Dunlop, r=Raibl (up=upper pebbly), w=Warnes (up=upper pebbly)), O=Otherside, RD=Read, S=Smart, W=Wolverine Point, d=diabase. Members of LZ, LL, and O are indicated by lines and labels but only one shade is used per formation. "Wollaston-Mudjatik transition zone". CIS=Carswell Structure. Generalized fault zones include multiple ductile movements before deposition of Athabasca Group and brittle transcurrent and dip-slip movements during and after deposition; they are named as: A=Allan, BB=Black Bay, BL=Black Lake, BR=Beatty River, BU=Bustard, CB=Cable Bay, CH=Charlot, CHB=Charbonneau, CL=Charles Lake, CT=Clut, D=Dufferin, ER=East Rim, F=Fidler, FN=Fowler–Net Lake, GR=Grease River, H=Harrison, HT=Hudsonian thrusts (general trajectory), LL=Leland Lakes, MAY=Maybelle, NF=Needle Falls, PL=Parker Lake, P2=P2 fault at McArthur River, R=Richardson, RI=Riou, RL=Reilly Lake, RO=Robillard, RON=Robillard north, ROS=Robillard south, SL=St. Louis, T=Tabbernor, VR=Virgin River array (Dufferin is one named fault of many in VR), Y=Yaworski, YH=Yatsore-Hill Island. Arrays of faults with similar orientation and offset are indicated by colour groups. 53
Figure 5.4: Cross-section of the Athabasca Basin taken and modified from (Ramaekers et al., 2007). The emplacement of the cross-section can be seen on Figure 5.3..... 55
Figure 5.5: A - Alteration zones and B - associated alteration minerals, taken and modified from (Jefferson et al., 2007)..... 56
Figure 5.6: Plan view of the emplacement of the cores used in this study. Note that the samples collected are described in Table B-1 in Annex B above Legend: yellow phase 1 (eastern pod), red phase 2 (western pod). Figure sent from Cameco by Stephen Zubowski..... 64
Figure 6.1: Log-normal distribution of the concentration of neutron absorbers in the samples..... 66
Figure 6.2: Correlation between the concentration of uranium and boron..... 68
Figure 6.3: Correlation between the concentration of uranium and samarium. 69
Figure 6.4: Correlation between the concentration of uranium and gadolinium..... 69
Figure 6.5: Model calculated ^{236}U vs ^{238}U, log-normally distrbuted, this figure shows the percent change in ^{236}U with the percent change of ^{238}U. The correlation shows that ^{236}U increases at a slower rate then ^{238}U. 72
Figure 6.6: Histogram depicting the range of the $^{236}U/^{238}U$ ratio results from the prediction model. Note the logarithmic scale..... 73
Figure 6.7: Correlation between $^{236}U/^{238}U$ atom/atom ratio from the model vs the concentration of B. Note the logarithmic scale and relation..... 74
Figure 6.8: Correlation between $^{236}U/^{238}U$ atom/atom ratio from the model vs the concentration of Gd. Note the logarithmic scale and relation. 74

Figure 6.9: Correlation between $^{236}U/^{238}U$ atom/atom ratio from the model vs the concentration of Sm. Note the logarithmic scale and relation. 75
Figure 6.10: ±5% error in B concentration introduced to the calculation of ^{236}U production 77
Figure 6.11: Resulting propagated error (relative change) of a +5% B concentration in the initial elemental composition. 78
Figure 6.12: Resulting propagated error (relative change) of a -5% B concentration in the initial elemental composition. 78
Figure 6.13: ±5% error in Sm concentration introduced to the calculation of ^{236}U production. 80
Figure 6.14: Resulting propagated error (relative change) of a +5% Sm concentration in the initial elemental composition. 81
Figure 6.15: Resulting propagated error (relative change) of a -5% Sm concentration in the initial elemental composition. 81
Figure 6.16: ±5% error in Gd concentration introduced to the calculation of ^{236}U production 83
Figure 6.17: Resulting propagated error (relative change) of a +5% Gd concentration in the initial elemental composition. 84
Figure 6.18: : Resulting propagated error (relative change) of a -5% Gd concentration in the initial elemental composition. 84
Figure 6.19: ±5% error in U concentration introduced to the calculation of ^{236}U production 86
Figure 6.20: Resulting propagated error (relative change) of a +5% U concentration in the initial elemental composition. 87
Figure 6.21 : Resulting propagated error (relative change) of a -5% U concentration in the initial elemental composition. 87
Figure 7.1 : Range and distribution of the $^{236}U/^{238}U$ atom ratios for 91
Figure 7.2 : Comparison in distribution between the 26 AMS measured samples and 20 measurements done in previous studies on uranium ore samples. 92
Figure 7.3: Comparison of the range of $^{236}U/^{238}U$ atom-to-atom ratio of the measured values of this study and published measurements 93
Figure 7.4: Concentration of ^{236}U (atoms/g) measured with the AMS vs the concentration of ^{238}U (atoms/g) measured at SRC. Note that the ^{236}U is calculated based on the $^{236}U/^{238}U$ measured with the AMS and the concentration of ^{238}U (atoms/g) measured at SRC. Both concentrations are expressed on the logarithmic scale and the linear relation is done on the log values of the concentration because they are normally distributed on the log scale as explained in Chapter 6. 94
Figure 7.5: $^{236}U/^{238}U$ atom-to-atom ratio in the samples measured by AMS. Samples are ordered based on U concentration: Lowest concentration of U (CL-M-58 (0.64ppm)) to highest concentration of U (CL-M-40 (66.2%)). Note the logarithmic scale. 96
Figure 8.1: ^{236}U (atoms/g) prediction model vs AMS measurements with a one-to-one line. Note that both the concentration of ^{236}U (atoms/g) of the prediction model and the concentration of ^{236}U (atoms/g) of the AMS measurements are expressed on logarithmic scales as the values are wide-spread and that the

error bars are smaller than the data symbols in this logarithmic visualization. 100
Figure 8.2 : Represents the same data as Figure 8.1, color-coded to the geology and U content of each sample. ^{236}U (atoms/g) prediction model vs AMS measurements with a one-to-one line. Note that both the concentration of ^{236}U (atoms/g) of the prediction model and the concentration of ^{236}U (atoms/g) of the AMS measurements are expressed on logarithmic scales as the values are wide-spread. The circled values represent outliners. 101
Figure 8.3 (left) and Figure 8.4(right): Profile of the concentration in ppm of U, B, Sm and Gd through non-mineralized sandstone away from known mineralization (Figure 8.3) and through mineralized ore (Figure 8.4). Note the logarithmic scale of concentrations. 109
Figure 8.5: Compilation of the 236U/238U atom ratio of previously published studies and our AMS results. Note the logarithmic scale. (Berkovits et al., 2000; Hotchkis et al., 2000; Steier et al., 2008; Wilcken et al., 2007; Zhao et al., 1994) 117
Figure 8.6: Concentration of ^{236}U (pg/kg) measured with the AMS vs the concentration of U (ppm) measured at SRC. Both concentrations are expressed on the logarithmic scale as they span on a wide range. Note that this Figure represents the same data presented in Figure 8.5 but converted from atoms/g to pg/kg. 118
Figure 8.7 (on the left) and Figure 8.8 (on the right): Depth profile of the concentration in pg/kg of ^{236}U through non-mineralized sandstone away from known mineralization (Figure 8.10) and through mineralized ore (Figure 8.11). Note the logarithmic scale of concentrationThe ^{236}U concentration (pg/kg) of the measurements done with the AMS are illustrated as dots and the results of the prediction model are expressed as a dashed-line. 120

Liste of Tables

Table 3-1: Summary of the neutron production due to spontaneous and induced fission (* Shulits and Faw, 2008; ** from IAEA-CRP-STD)....18
Table 4-1: Setup parameters used to tune the AMS before and during the analyses of the samples....34
Table 4-2: Summary of the blanks used for calibration during the ^{236}U experiments using the AMS....42
Table 4-3: Procedural Blanks used for calibration during the experiment....43
Table 5-1: Cigar Lake mineral resources as indicated by Cameco in the IN 43-101 report 2016, last updated December 31, 2016 (Bishop et al., 2016)....60
Table 5-2: Cigar Lake mineral reserves as indicated by Cameco in the IN 43-101 report 2016, last updated December 31, 2016 (Bishop et al., 2016)....60
Table 8-1: Table comparing the results from AMS measurements calculation from the prediction model. A more complete table can be found in the Annex B, Table B-4....99
Table 2 -2: Samples originating from perched mineralization. Results of the AMS measurements and values obtained from the prediction model. A more complete table can be found in the Annex B, Table B-3....115

1. Introduction

According to the World Nuclear Association, Canada is accounted for 15% of the world's uranium production and the Athabasca basin is host to the highest grade uranium (U) deposits in the world ("IAEA UDEPO," 2017). These deposits are all unconformity related deposits, implying that the mineralization, the ore, is situated at the unconformity between the granitic basement rock and the overlying sandstone (Ramaekers et al., 2007). The mineralization is localized and surrounded by alteration haloes in faulted zone. A lot of the unconformity related uranium deposits in the Athabasca basin have the same characteristic marks including: general structural setting, age of mineralogy, host rock association mineralogy and geochemistry but the deposits differ in size, intensity of alteration and associated clay minerals and mostly by the concentration of high grade uranium mineralization (Bishop et al., 2016). Cigar Lake and McArthur River are the highest-grade deposits known in the world. Due to the interest in their high grade, the exploration for similar deposits has been and continues to be intensive. Geological features such as intersecting steeply dipping faults and favorable structural sites have been identified and geophysical tools such as seismic reflection have been used to provide the structural framework (Jefferson et al., 2007). Lake water geochemistry, sediment geochemistry, surficial geochemistry and alteration geochemistry have all been used as tools to target and identify where these deposits are or could be situated (Jefferson et al., 2007). Exploration also includes ground and airborne gravity to detect alteration zones, electromagnetic methods to survey alteration zones and crudely map fault offsets of the unconformity. But actually most of these deposits have been found by

luck with drilling, as the geophysical and geochemical tools that exist do not always give positive results. Additional possible tools are always investigated, as drilling is expensive. In many cases, the mineralization is localized in such way that it is hard to find them in large exploration campaigns.

A potentially geochemical feature for these deposits is the presence of ^{236}U. In nature, uranium primarily exists as three long lived α-emitting isotopes: primordial ^{238}U ($t_{1/2}$ = 4.47 billion years), ^{235}U ($t_{1/2}$ = 700 million years); and radiogenic ^{234}U ($t_{1/2}$ = 246,000 years). ^{236}U is a radionuclide with a half-life of 23.48Ma that is formed when ^{235}U absorbs a neutron. This radionuclide persists 18% of the time and fissions 82% of the time. In a deposit such as Cigar Lake, dated to 1.3Ga (Cumming and Krstic, 1992) with high grade uranium that is almost completely isolated from groundwater, ^{236}U could be accumulating in the ore and in the alteration halo and could possibly be used as a tracer for detecting high-grade U deposits.

Geochemical prediction models for the concentration of certain radionuclides in nature have been developed to simplify measurements and to apply the prediction to larger scales. When an isotope is rare and in trace form, the measurement can be quite difficult and/or expensive. But a prediction model offers the advantage of a large-scale interpretation of the behavior of the radionuclide, while using only a restricted set of parameters (for example the main contributors to the formation of the radionuclide). Thus, radionuclide prediction models have been developed as tools to trace hydrogeologic processes (Fabryka-Martin, 1988) and to access scenarios of radionuclide release in the environment (Cornett et al., 2010; Curtis et al., 1999; Fabryka-Martin et al., 1994; Fabryka-Martin and Curtis, 1993). Fabryka-Martin (1988) made an intensive

physical study of the formation of neutron induced radionuclides. Her study was concentrated on the mathematical calculation of the formation of isotopes by absorption of a neutron but also on the nature of neutrons and their behaviour with matter. Her study has inspired the approach taken in this thesis.

In the context of uranium deposits, prediction models have already been elaborated for radioactive isotopes such as ^{36}Cl, ^{237}Np, ^{239}Pu, ^{99}Tc and others that are formed by neutron absorption like in the case of ^{236}U (Fabryka-Martin, 1988; Fabryka-Martin et al., 1994; Fabryka-Martin and Curtis, 1993). With the use of the transport code Monte Carlo Neutron and Photon (MCNP) (Briesmeister, 1986) that uses statistical techniques to predict behavior of neutrons in a set matter, the concentration of the isotopes had been estimated by constructing mathematical three-dimensional models to simulate a specific physical situation. The resulting models were used to delimitate boundary conditions for the formation of the radioactive isotopes (Cornett et al., 2010; Curtis et al., 1999; Fabryka-Martin et al., 1994; Fabryka-Martin and Curtis, 1993).

In order to measure the trace amount of ^{236}U present in different types of samples, an accelerator mass spectrometer (AMS) needs to be used as the instrument has an enhanced isotopic abundance sensitivity up to $1*10^{-13}$ at the André E. Lalonde laboratory (AELL) at the University of Ottawa. Other previously used methods such as α-spectrometry and thermal ionization mass spectrometry (TIMS) are limited in their isotopic abundance sensitivity and cannot measure samples with $^{236}U/^{238}U$ ratio below $1*10^{-8}$ (Zhao et al., 1997).

^{236}U has been studied in the past but only looked at as a potential geochemical tool in the last few years. ^{236}U has become of interest because of its association to nuclear fuel and nuclear fallout. In a nuclear reactor, ^{236}U acts as a neutron poison and accumulates in the fuel, absorbing valuable neutrons that otherwise would create the ^{235}U nuclear fission. In case of nuclear fuel leaks, ^{236}U was used to trace anthropogenic U contamination in nature around nuclear power plants and due to nuclear testing (Hotchkis et al., 2000; Steier et al., 2008). ^{236}U was also used as a tracer in water movement (Sauvé, 2016). Figure 1.1 presents a compilation of the ^{236}U/^{238}U atom-to-atom ratios found in previous studies.

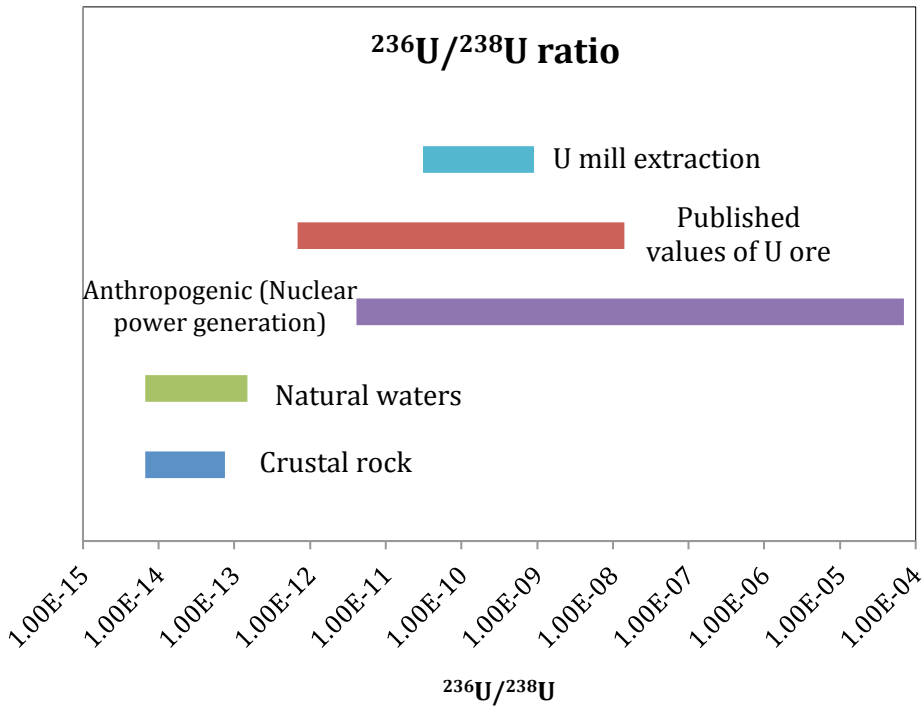

Figure 1.1 Representing the range of ^{236}U/^{238}U atom/atom ratio as found in previous studies. Note the logarithmic scale. A table of the data can be found in Annex A

Number wise, as a non-anthropogenic "background" ratio, in crustal rock it was calculated by (Steier et al., 2008) that the ^{236}U/^{238}U ratio should be $1*10^{-14}$ to $5*10^{-14}$

atoms/atoms while natural waters should have a ratio of $1*10^{-14}$ to $1*10^{-13}$ atoms/atoms. Anthropogenic ^{236}U measured around different nuclear plants has $^{236}U/^{238}U$ ratios in soil and water samples varying between $1.45*10^{-5}$ atoms/atoms to $7*10^{-12}$ atoms/atoms (Hotchkis et al., 2000; Steier et al., 2008; Zhao et al., 1997).

In previous studies, ^{236}U was measured in multiple samples taken to test and improve the use of the AMS. Tendencies have been observed, but never before a complete set of samples originating from the same deposit has been tested. Measurements show that U-ore has a $^{236}U/^{238}U$ isotopic ratio of $9.5*10^{-9}$ to $8.2*10^{-12}$ in samples of ore from 0.5% to 79% U concentration (Berkovits et al., 2000; Hotchkis et al., 2000; Steier et al., 2008; Wilcken et al., 2008; Zhao et al., 1994). Murphy et al. (2015) have looked at ^{236}U as a potential tracer in one U-deposit. Their study was done in parallel to this one, and is discussed later in this thesis. All the values discussed in this section are shown in Figure 1.1 and can be found in Table A-1 in Annex A with their respective reference.

This study will look at the Cigar Lake deposit, a well-studied geological site, to examine the distribution of ^{236}U around and in the deposit. This thesis approaches the subject by constructing a prediction calculation of the distribution of ^{236}U radionuclide using the elemental composition of samples collected at Cigar Lake. The samples were then measured for ^{236}U content using the AMS at AELL in Ottawa. The results of this study are presented in three different sections: the prediction model results, the AMS results and the discussion. The discussion section will compare the prediction model results to the measurements obtained with the AMS and try to answer multiple questions that will help us test the validity of (1) the model and (2) of the AMS results as well as to assess the behavior of the ^{236}U radionuclide at Cigar Lake.

Objectives:

The objectives of the present research are to: (1) Construct a prediction model that can be used to estimate the distribution of ^{236}U radionuclide around and in the Cigar Lake uranium ore deposit (2) Verify these results by means of measurements performed on the samples with an accelerator mass spectrometer (AMS), and (3). Determine the potential of ^{236}U to be used as a tracer in the exploration of high-grade uranium deposits such as the Cigar Lake deposit based on these results.

2 Concepts and Definitions

To understand the ideas behind this thesis, this chapter will focus on defining important terms and concepts used in the mathematical prediction model and in the analyses of the samples using the Accelerator Mass Spectrometer (AMS).

The following concepts are key to understanding the physics behind the prediction model in the next chapter.

2.1 Radioactive decay

Radioactive decay, also know as radioactivity, can be defined as the process in which the nucleus of an unstable atom releases energy and emits matter (particles) to get closer to a more stable state. These particles are emitted by radiation and can be of various types, the most common being alpha particles (α), beta particles (β) and gamma photons (γ).

A quick summary of these common particles:

An alpha particle (α) is a particle composted of two protons and two neutrons, similar to the helium nucleus. The alpha decay is favored in heavier nuclides. It reduces the neutron-proton ratio of the parent isotope to a more stable configuration.

A beta particle (β) is a high energy and high-speed electron or positron. The beta decay (β-) occurs when a neutron is transformed into a proton inside the nucleus and an electron is emitted. Vice versa, when a proton is transformed into a neutron in the nucleus, a positron is emitted (β+). These types of decay allow the atom to reach closer to

its optimal neutron to proton ratio.

A gamma photon (γ) is a high-energy photon emitted by the nucleus. Gamma decay allows the atom to go from a high-energy state to a lower energy state by emitting energy in the form of electromagnetic radiation without changing its other nuclear characteristics.

Fission is also a type of radioactive decay in which the nucleus of an atom splits or is broken into smaller nuclei with simultaneous conversion of part of the mass into energy. Fission can occur spontaneously (spontaneous fission SF) as a natural decay process or it can be induced by the absorption of a relatively low energy particle like a neutron (neutron-induced fission NF) or a photon. For every neutron induced fission events, in addition to the two fragments, several neutrons can be released. The fission process becomes important only in heavy nuclei from thorium and beyond, even though any nucleus can fission if provided with enough excitation energy. Figure 2.1 illustrates an example of the distribution of fission products in relation to the fission yield for neutron-induced fission (NF) of ^{235}U by thermal neutron and ^{238}U by fast neutron and for spontaneous fission (SF) of ^{238}U.

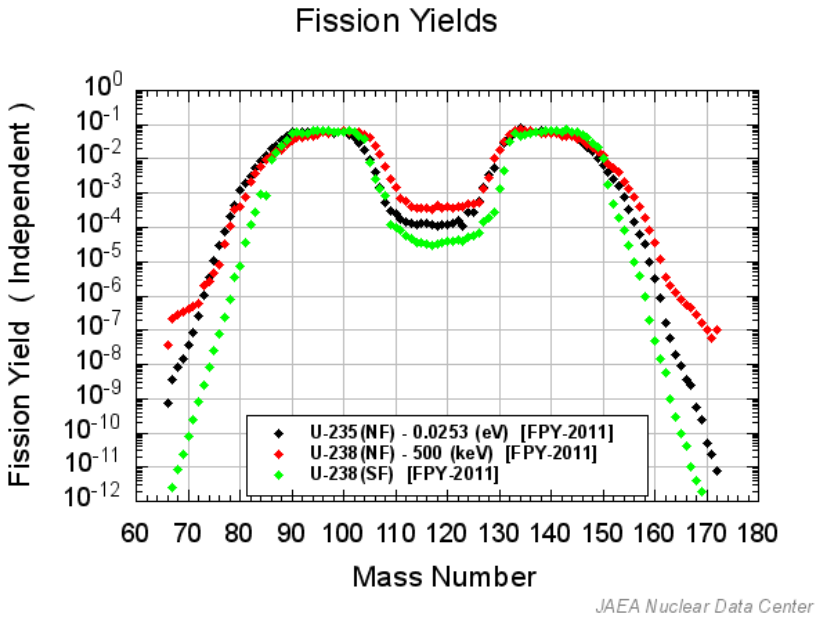

Figure 2.1: Distribution of induced fission fragments of ^{238}U (U-238 NF) and ^{235}U (U-235 NF) and spontaneous fission fragments of ^{238}U (U-238 SF) done using the JAEA Nuclear Data Center plotting tool.

2.2 Half-life and Decay constant

For radioactive decay, we express the rate of decay as half lives ($t_{1/2}$): the time it takes for half of the radioactive nuclei to undergo radioactive decay. Since radioactive decay occurs exponentially, another term, the decay constant (λ) is also used to express the rate of decrease per time unit. Half time and decay constant are related by the equation:

$$\frac{dN}{dt} = -\lambda N$$

where $\frac{dN}{dt}$ is the decrease per time unit, N total population of atoms at a given time. The decay constant can also be expressed as $= \frac{\ln(2)}{t_{1/2}} = \frac{0.693}{t_{1/2}}$.

2.3 Nuclide

The nuclides represent all particular types of atoms with a specific number of protons and neutrons.

2.4 Isotopes

An isotope is defined as a nuclide with the same number of protons but different numbers of neutrons. Isotopes can be naturally occurring or created during a nuclear reaction. Some isotopes are stable in nature while others are unstable and are called radioisotopes.

2.5 Nuclear reactions

A nuclear reaction is a change of the structure and properties of an atomic nucleus as a result of the interaction with an energetic particle. In general, a reaction or the collision of an atom with a particle can be written as:

$$X + a \rightarrow Y + b$$

or as the compact version:

$$X(a, b)Y$$

Where X and Y are the target and product nuclei and a and b the incident and emitted particles. Incident and emitted particles can be neutrons (n), Alpha particles (α), protons (p) and others. As an example, in the (α,n) reaction, the α particles are the incident particles and the neutrons are the emitted particles. For every incident particle, several different paths can occur, having each a different set of product nuclei and particles.

2.6 Reaction Cross-Section

The reaction cross-section, also called microscopic cross-section, (σ) is used to determine the relative probability of a given reaction $X(a,b)Y$ to occur. It is commonly expressed in barns where 1barn $(b) = 10^{-24} cm^2$ and can be visualized as the area on the target nucleus that is bombarded by the incident particle (Krane, 1988). The reaction cross-section of each nucleus is energy dependent upon the incident particle and can vary rapidly (Ensslin, 1991).

2.7 Macroscopic Cross-Section

The macroscopic cross-section is a concept used in characterizing bulk material for the probability of interaction with a particle. It takes into consideration the material, with its multiple elements and the cross-section associated to each element. It is defined as the sum of the number of atoms of each element per volume unit times the atom's associated reaction cross-section:

$$\Sigma_t = \sum_i N_i \sigma_i \quad (cm^{-1}) \qquad (2.1)$$

where Σ_t is the macroscopic cross-section expressed in cm^{-1}, N_i is the density of atoms of element i (atoms/cm^3), and σ_i the reaction cross-section of element i (cm^2). It is an analogous concept to the linear attenuation coefficient (Ensslin, 1991).

2.8 Particle flux

The particle flux can be described as the number of particles going through an area (unit cross-section) during a time unit. Usually it is expressed in particles/cm^2/s. It can

also be described as the production rate divided by the attenuation coefficient, as the particles are absorbed through the matter. The attenuation coefficient is the sum of the respective probabilities of absorption of the particle by matter, in our case the macroscopic cross-section.

2.9 Neutron capture and thermal neutrons.

Neutron capture is the process by which a neutron is absorbed in the nucleus of another particle. This process only occurs with neutrons with low energies, thermal neutrons (<0.025eV) being the most dominant. In nature, neutrons emitted during a reaction can have different energies. For example, fission releases fast neutrons (E ~1MeV): those neutrons can be "thermalized" meaning that their energy can be reduced to thermal neutron level by collision or attenuation due to other elements in their path. In sandstone, the probability that a neutron will be thermalized before capture was calculated by Fabryka-Martin (1988) as 0.96, meaning that in sandstone, almost all neutrons are thermalized before capture.

2.10 The decay chains

There are 3 naturally occurring decay chains: ^{238}U, ^{235}U and ^{232}Th. These are called chains because they decay naturally from the parent isotope into their daughters via α and β decays. As the α particles are released, they create in return (α,n) reactions with lighter elements that release neutrons. The three naturally occurring chains can be observed in Figure 2.2.

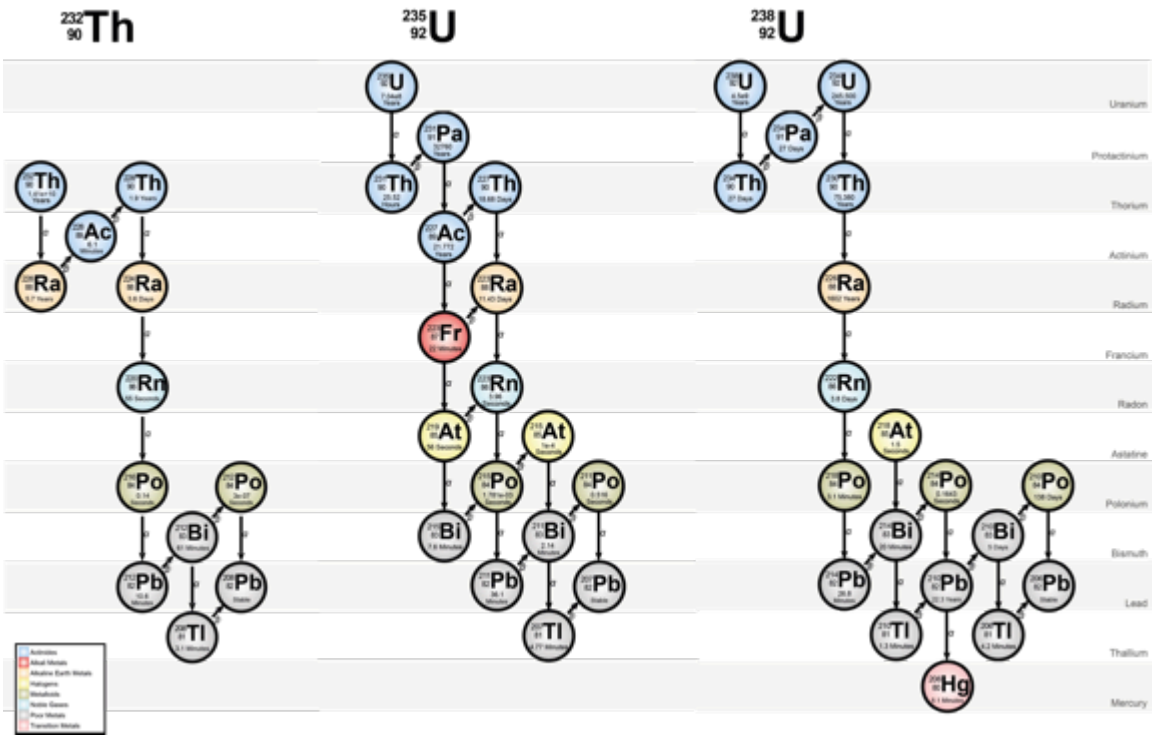

Figure 2.2: The three natural occurring decay chains ^{232}Th, ^{235}U and ^{238}U

2.11 Coulomb explosion

The concept of Coulomb explosion is important in understanding how the AMS works. When a molecule having a very high velocity is striking a mass, the binding electrons of the atoms that compose the molecule are stripped from the atoms; as a result, the atoms are left positively charged and the mutual electrostatic repulsive force will release them as free atoms by breaking the molecule.

3. A model of ^{236}U production and distribution

In a uranium deposit such as Cigar Lake, conditions must be identified and processes taken into account to be able to build a model of ^{236}U production and distribution. ^{236}U is formed when ^{235}U absorbs a neutron meaning the nucleus of the ^{235}U atom incorporates the neutron and so becomes ^{236}U. 82% of the time, ^{236}U will fission. However in the other 18% of the time, ^{236}U does not fission and ^{236}U nucleus persists with a half-life of 23.48 Ma. This neutron activation process makes neutrons the principal driver of the system.

To have a simplified calculation prediction model that can explain the distribution and production of ^{236}U, certain assumptions can be made. The first assumption to simplify our model is that **all neutrons are thermal.** Although all neutrons do not have thermal energies when they are emitted, in sandstone, i.e. the composition of the Athabasca basin, it was calculated that the probability that a neutron reaches thermal energy levels before being absorbed was of 0.96 (Fabryka-Martin, 1988). This means that almost all neutrons will have thermal energies before being absorbed in matter and in this way our assumption can simplify our calculation. A second assumption is that the **system is homogeneous over the scale of a few meters**. A uranium deposit is highly heterogeneous even at the scale of cm and the mineralization can be very isolated. This assumption is false but by creating bulk compositions, we can have an easier first estimate calculation. A third assumption is also made, that the **system is at equilibrium between production and radioactive decay and there are no losses of ^{236}U due to**

other processes. This means that the system is closed to other processes and has not been disturbed. This assumption can be made as the mineralization at Cigar Lake is partially isolated from groundwater flow (Cornett et al., 1996) and allows us to make the model non-time dependent.

To build a quantitative model of the factors that influence the concentration of ^{236}U, we need to identify the source where the neutrons originate, quantify them, and see where these neutrons go to finally see the resulting reactions and the concentration of ^{236}U.

3.1 The sources of neutrons in the system

The main Cigar Lake ore deposit is situated about 400-500m deep. In the subsurface, below 30m, cosmic rays do not have influence on neutron production and only fission and (α, n) reactions on light nuclei are the main contributors to the production of neutrons as illustrated in Figure 3.1 (Fabryka-Martin, 1988; Fabryka-Martin et al., 1994). Both fission and (α,n) reactions release fast neutrons. Neutrons produced by (α,n) reaction have initial energy of 0.5 to 3MeV and can range up to 10MeV (Kaplan, 1955). Neutrons produced from spontaneous fission have energies from 2MeV up to 17MeV (Kaplan, 1955). As mentioned above, in sandstone, the probability that neutrons will reach thermal energies before capture has been calculated to be 0.96 (Fabryka-Martin, 1988). Because the probability of thermalization is so high, our assumption that all neutrons are thermal seems reasonable.

In rock, thermal neutrons have a free mean path of about 0.5m to less than 10 cm in high-grade uranium ore (Curtis et al., 1999). The term "free mean path" represents the average distance that the neutron can travel between two interactions. As this distance is small and used for bulk composition, the production rate can be considered as "punctual", meaning that the production rate of the bulk is used in our calculation.

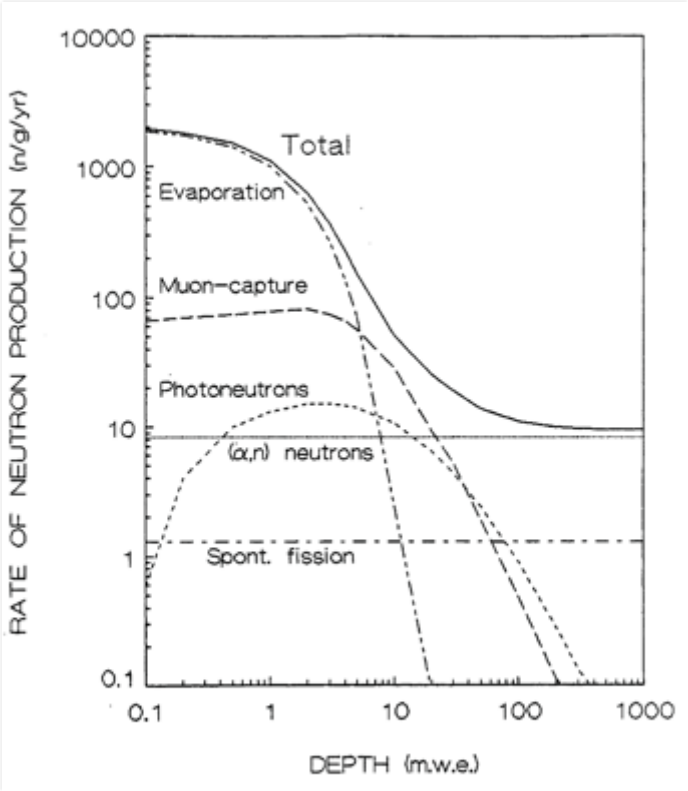

Figure 3.1: Neutron production profile in High Ca-granite taken from Fabryka-Martin, 1988. It shows the processes by which neutrons are produced in meters of water equivalent (mwe). Depth in mwe is a normalized way of expressing depth independent of rock density and is conveyed as $d_{mwe} = h(\rho_r/\rho_w)$ where h is the absolute depth in meters, ρ_r is the average bulk density of the overlying rock (g cm-3) at depth and $\rho_w$is the density of water (1g cm-3). At Cigar Lake, the average bulk density is between 2.5g cm-3 for minerals not containing U ore and 7.5 g cm-3 for ore (Fabryka-Martin et al., 1994), hence, below 30m, only fission and (α,n) reactions produce neutrons.

3.1.1 Alpha - neutron reaction (α,n)

As ^{238}U and ^{235}U undergo their chain decays, they release alpha particles (α). Light elements, with atomic number lower than chlorine (Ensslin, 1991), capture the α-particle and release neutrons. α-particles have a mean free path of a few microns. Hence the calculation of the neutron production rate is dependent on the micro-distribution of α-emitting radionuclides relative to the elements with significant (α,n) reaction cross-section. Theses properties are not easy to characterize and make the task of calculating the neutron production very complex.

3.1.2 Fission

^{238}U and ^{235}U have very low probabilities of undergoing spontaneous fission (Krane, 1988) because it competes with alpha decay.

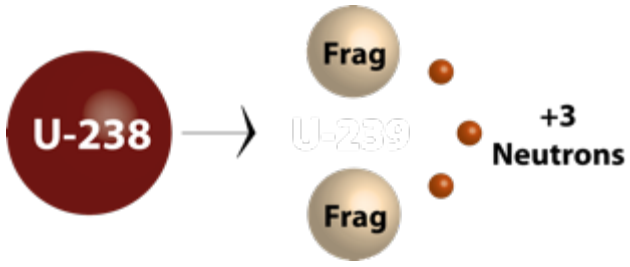

Figure 3.2 ^{238}U generalized spontaneous fission

On the other hand, fission-induced by a neutrons occurs in both isotopes and can be observed in Figure 3.3.

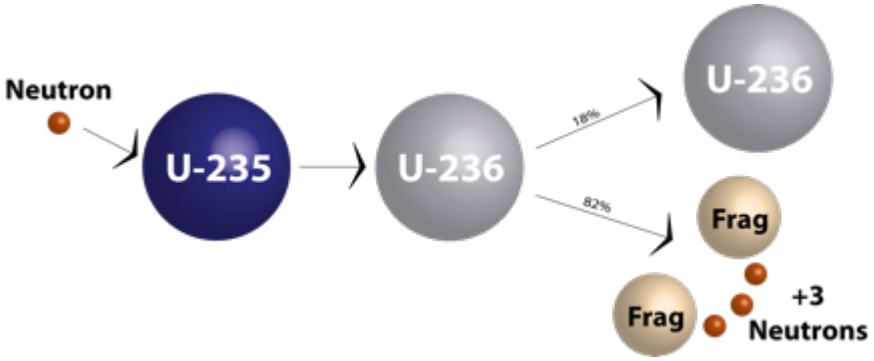

Figure 3.3: the ^{235}U neutron-induced fission

The average number of neutrons produced for each type of fission is summarized in Table 3.1. Please note that ^{238}U does undergo induced fission, but it is induced by fast neutrons (E~1MeV) while ^{235}U undergoes fission induced by thermal neutrons (E > 0.025eV). Figure 3.4 illustrates the fission cross-sections for both ^{235}U and ^{238}U depending on the energy of the incident neutron.

Table 3-1: Summary of the neutron production due to spontaneous and induced fission (* Shulits and Faw, 2008; ** from IAEA-CRP-STD).

Isotope	Type of fission	Fission half-life (y)	Fission constant (/y)	Neutrons/ Fission
^{235}U **	induced thermal neutron			2.43
^{238}U **	induced fast neutron			2.82
^{235}U *	spontaneous	3.50E+17	1.98E-18	1.86
^{238}U *	spontaneous	8.40E+15	8.25E-17	2.07

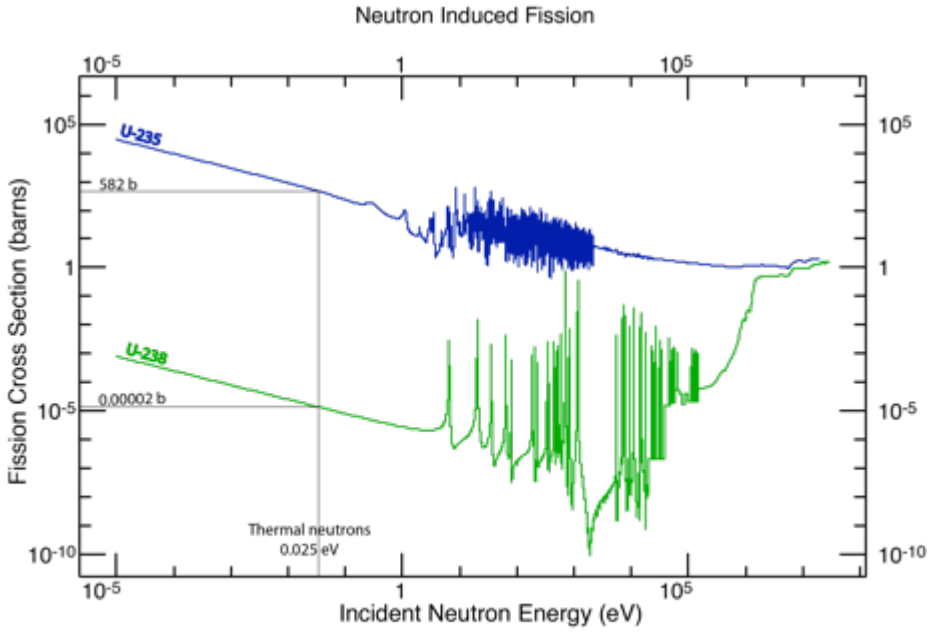

ENDF/B-VII.1: U-235(N,F) & U-238(N,F)

Figure 3.4 Fission Cross-Sections for neutron induced fission created using https://www-nds.iaea.org/exfor/endf.htm using the ENDF/B-VII.1 database and modified.

Mathematical methods allow the calculation of the production rate of neutrons due to both spontaneous and induced fission. However, no such method is used in this project as measurements done at Cigar Lake were available.

3.2 Neutron production rate

As mentioned above, the neutron production rate was not calculated for this project. We used the neutron production rate measured by a neutron coincidence counter at Los Almos National Laboratory by Fabryka-Martin et al., (1994) during their study at Cigar Lake. The neutron production rate was measured from ten "ore" samples (CS235L and nine samples from hole 220). A linear regression between neutron production rate P_n (n

$gr^{-1}yr^{-1}$) and U content in percentage, the relationship with a correlation coefficient of 0.991 was found:

$$\boldsymbol{P_n = (2.13 * 10^4) + (9.42 * 10^3) * (U\%)} \ \ \textbf{(n g}^{-1}\textbf{yr}^{-1}\textbf{)} \qquad \textbf{(3.1)}$$

Information about the methodology of measurement is not available. In this dissertation, the neutron production rate given is assumed to result from the sum of fission and (α,n) reactions.

3.3 The main neutron absorbers

Neutron absorbers are elements with high neutron cross-sections present in the system. At Cigar Lake, using the bulk composition of core (core CS235L described in (Fabryka-Martin et al., 1994)) , we identified the elements that interact the most with the neutrons and that consequently absorb the available neutrons. These elements have higher cross-sections and/or their concentration is high enough, making them the major neutron absorbers present. Four elements stand out as high absorbers: boron (B), samarium (Sm), gadolinium (Gd) and uranium (U), with their specific neutron-absorbing isotopes ^{10}B, ^{147}Sm, ^{149}Sm, ^{155}Gd, ^{235}U and ^{238}U, their cross-section being illustrated in Figure 3.5. In this figure it can be observed that some of these neutron-absorbing isotopes have somewhat lower cross-sections. It is the presence of high concentration of these elements, such as B in the bulk composition that makes them important neutron absorbers. Please note that ^{236}U is also plotted in Figure 3.5 to demonstrate that it has a thermal neutron absorption cross-section of 5.09b and, paired with expected low concentrations, will have a negligible effect on the total neutrons absorbed.

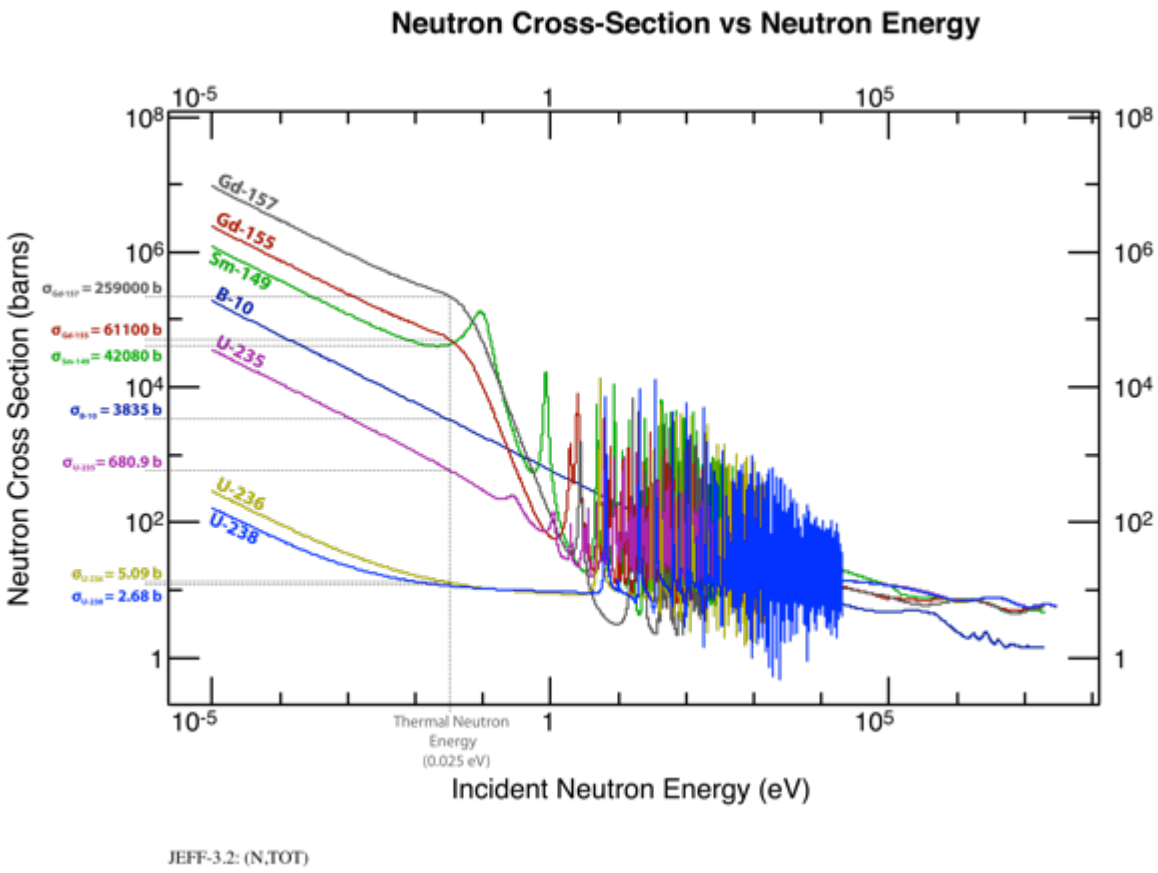

Figure 3.5: Neutron Cross-Sections of the major neutron absorbing elements. Created using https://www-nds.iaea.org/exfor/endf.htm using the JEFF-3.2 database and modified.

3.4 Calculating the neutron flux

As described in the concept and definitions section, Chapter 2, the neutron flux is the number of neutrons going through an area (cross-section) during a time unit and is measured in neutrons $cm^{-2}s^{-1}$. It identifies the available neutrons in the system for any given neutron related reaction. For this dissertation, we assume that all neutrons are thermal when absorbed; hence the neutron flux will be of thermal neutrons. The neutron activation rate is calculated using the number of neutrons that are produced, which we assume will be thermal, divided by the macroscopic neutron cross-section of the bulk composition. As explained in the concepts and definitions chapter, the macroscopic

cross-section acts like an attenuation factor for the neutrons. As we are assuming that the samples are homogeneous, this implies that the targets are equally distributed in the bulk composition and hence that the neutrons are absorbed at the same rate equally in the sample. This assumption allows the calculated neutron flux to be an estimate of the available neutrons available after interaction with matter.

$$\boldsymbol{\phi_n = \frac{P_n}{\sum N_i * \sigma_i}\ (\text{n cm}^{-2}\text{yr}^{-1})} \qquad \textbf{(3.2)}$$

Where ϕ_n is the neutron flux, P_n is the neutron production calculated via equation (3.1). The macroscopic cross-section presented in equation 2.1, $\Sigma_t = \sum N_i \sigma_i$ where N_i and σ_i are the number of atoms and their associated neutron cross-section for each element of the bulk composition. In our case, only the prominent neutron absorbers, ^{10}B, ^{147}Sm, ^{149}Sm, ^{155}Gd, ^{235}U and ^{238}U were taken into account for the calculation of the macroscopic cross-section.

3.5 The prediction model and production of ^{236}U

The resulting prediction model is a calculation for each sample to determine the amount of ^{236}U present in the ore and rock; the calculation takes into account the bulk composition of each sample (assumed homogeneous) for uranium and the main neutron absorbers (B, Sm, Gd). Please note that each sample will have its own neutron flux, calculated from equation 3.2, and its own resulting concentrations of ^{236}U based on the samples composition.

The process of absorbing a neutron is called neutron activation. Since the model assumes

that the system is not time-dependent and that only 18% of the ^{236}U nuclei do not fission, the concentration of ^{236}U in the bulk system can be calculated as:

$$N_{236_U} = \frac{N_{235_U} * \sigma_{235_U} * \phi_n}{\lambda_{236_U}} * 18\%$$

$$\boldsymbol{N_{236_U} = \frac{N_{235_U} * \sigma_{235_U} * \frac{P_n}{\sum n_i * \sigma_i}}{\lambda_{236_U}} * 18\%} \quad \textbf{(3.3)}$$

where N_{235_U} and N_{236_U} are the number of nuclei of each isotope, ϕ_n is the thermal neutron flux calculated and σ_{235_U} is the neutron cross-section of ^{235}U. λ_{236_U} is the decay constant of the ^{236}U isotope calculated with its half-life ($t_{\frac{1}{2}}(^{236}U) = 2.342 * 10^7 y$).

$$\lambda_{236_U} = \frac{\ln(2)}{t_{1/2}(^{236}U)} = 2.96 * 10^{-8}\ year^{-1}$$

The ^{236}U/^{238}U atom-to-atom ratio is calculated by dividing the result of equation 3.3 with the concentration of ^{238}U in atoms par gram from the measurements done at SRC.

An illustrated set-up of the excel sheet can be seen in Figure 3.6 as it was applied to all samples. Each sample went through the calculations mentioned above and a table was made up with the result tabulated in Table B-2 annex B. These results are discussed and analyzed in a later chapter.

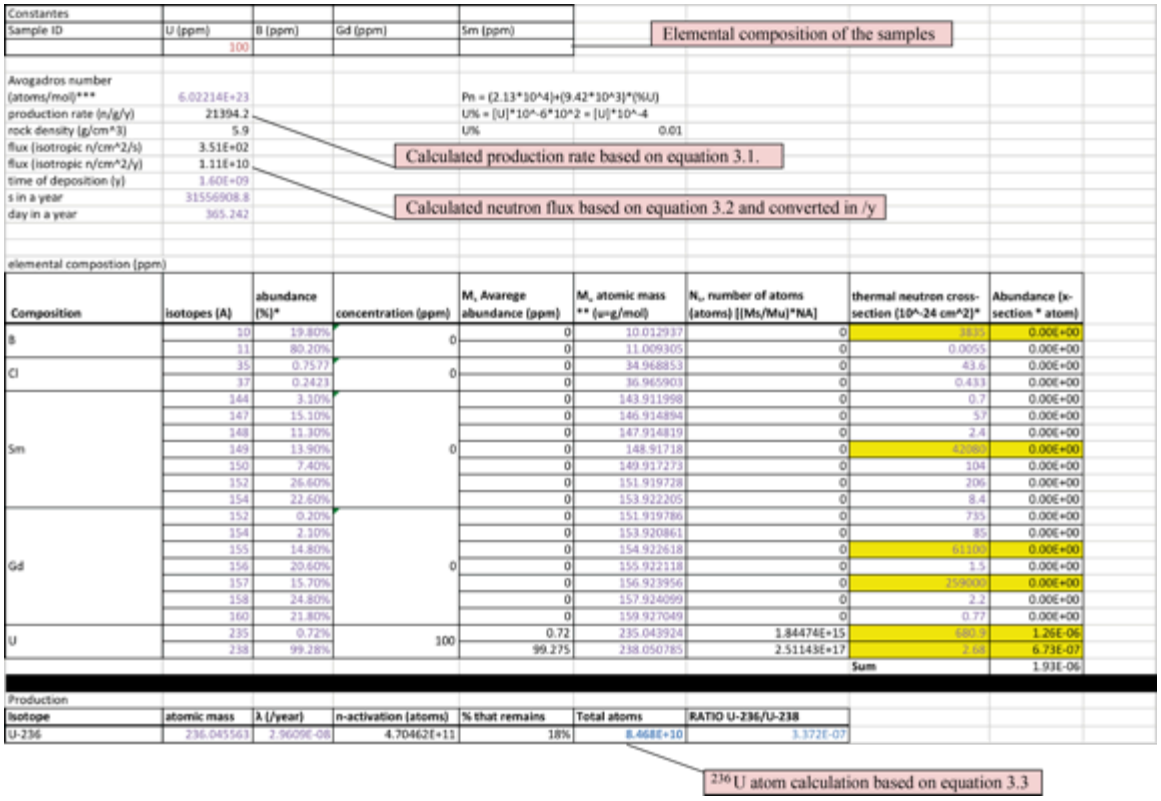

Constantes

Sample ID	U (ppm)	B (ppm)	Gd (ppm)	Sm (ppm)
	100			

Elemental composition of the samples

Avogadros number (atoms/mol)***	6.02214E+23
production rate (n/g/y)	21394.2
rock density (g/cm^3)	5.9
flux (isotropic n/cm^2/s)	3.51E+02
flux (isotropic n/cm^2/y)	1.11E+10
time of deposition (y)	1.60E+09
s in a year	31556908.8
day in a year	365.242

Pn = (2.13*10^4)+(9.42*10^3)*(%U)
U% = [U]*10^-6*10^2 = [U]*10^-4
U% 0.01

Calculated production rate based on equation 3.1.

Calculated neutron flux based on equation 3.2 and converted in /y

elemental composition (ppm)

Composition	isotopes (A)	abundance (%)*	concentration (ppm)	M_i Avarege abundance (ppm)	M_i atomic mass ** (u=g/mol)	N_i, number of atoms (atoms) [(Ms/Mu)*NA]	thermal neutron cross-section (10^-24 cm^2)*	Abundance (x-section * atom)
B	10	19.80%	0	0	10.012937	0	3835	0.00E+00
	11	80.20%		0	11.009305	0	0.0055	0.00E+00
Cl	35	0.7577	0	0	34.968853	0	43.6	0.00E+00
	37	0.2423		0	36.965903	0	0.433	0.00E+00
Sm	144	3.10%	0	0	143.911998	0	0.7	0.00E+00
	147	15.10%		0	146.914894	0	57	0.00E+00
	148	11.30%		0	147.914819	0	2.4	0.00E+00
	149	13.90%		0	148.91718	0	42080	0.00E+00
	150	7.40%		0	149.917273	0	104	0.00E+00
	152	26.60%		0	151.919728	0	206	0.00E+00
	154	22.60%		0	153.922205	0	8.4	0.00E+00
Gd	152	0.20%	0	0	151.919786	0	735	0.00E+00
	154	2.10%		0	153.920861	0	85	0.00E+00
	155	14.80%		0	154.922618	0	61100	0.00E+00
	156	20.60%		0	155.922118	0	1.5	0.00E+00
	157	15.70%		0	156.923956	0	259000	0.00E+00
	158	24.80%		0	157.924099	0	2.2	0.00E+00
	160	21.80%		0	159.927049	0	0.77	0.00E+00
U	235	0.72%	100	0.72	235.043924	1.84474E+15	680.9	1.26E-06
	238	99.28%		99.275	238.050785	2.51143E+17	2.68	6.73E-07
							Sum	1.93E-06

Production

isotope	atomic mass	λ (/year)	n-activation (atoms)	% that remains	Total atoms	RATIO U-236/U-238
U-236	236.045563	2.9609E-08	4.70462E+11	18%	8.468E+10	3.372E-07

^{236}U atom calculation based on equation 3.3

Figure 3.6: Template of the model made in excel.

4 Accelerator mass spectrometer (AMS)

To test the accuracy of the model described in Chapter 3 and to measure the amount of ^{236}U in the samples, a very sensitive mass spectrometric method is necessary. The levels of ^{236}U in uranium ore are known to be very low from previous studies, with $^{236}U/^{238}U$ ratio varying between $9.5*10^{-9}$ to $8.2*10^{-12}$ (Rokop, Metta, and Stevens 1972; Berkovits et al. 2000; Rucklidge, Wilson, and Kilius 1990; Wilcken et al. 2007; X. -L. Zhao et al. 1994; Murphy et al. 2015; Srncik et al. 2011; Steier et al. 2008; Wilcken et al. 2008; X-L. Zhao et al. 1994).

The Accelerator Mass Spectrometer (AMS) is an analytical instrument designed to measure very low (femto gram level) concentrations of rare radioisotopes by the addition of a tandem accelerator to an otherwise traditional mass spectrometer. For the measurements of the $^{236}U/^{238}U$ ratio, other analytical techniques such as α-spectrometry or thermal ionization mass spectrometry (TIMS) have limited sensitivity and cannot measure isotope ratios below 10^{-8} (Zhao et al., 1997). AMS has been shown to have an abundance ratio sensitivity (ARS) of $^{236}U/^{238}U$ up to 10^{-12} in previous studies (Wilcken et al. 2008) and will allow us to analyze samples of both high grade and low-grade uranium ore.

This chapter describes how the samples were prepared for AMS analysis, explains the basic functionality of the AMS as well as of the tandem accelerator, discusses the

problems encountered during the experiments and the corrections that have been used to calculate the concentrations of ^{236}U that are presented in the results.

4.1 Sample preparation

This section presents an overview of the procedure used in the preparation of the samples. It describes how the samples were first separated by grade and the order in which they were prepared. A description of how the uranium was extracted from the samples is included as well as how the extracted uranium was prepared to be pressed into targets for AMS analysis.

4.1.1 Sample assessments and separation

1. The uranium ore samples were first separated depending on grade and activity, using a handheld detector and stored accordingly to CNSC regulations. The samples were prepared in batches using the following procedure, in the grade order. The lower grade samples were prepared first as to avoid cross-contamination. They had an activity level of background of ~0.11μSv/hr to 0.2μSv/hr. The second batch, mid grade, was then prepared. The activity of these samples varied between 0.2μSv/hr and 2μSv/hr. Finally, with care, the high grade samples were prepared. These last samples had activity of >2μSv/hr. The separation in batches of the same grade ensured minimal cross-contamination due to high grade vs low grade samples and allowed minimal exposure and additional safety measures to handle the high grade ore samples.

4.1.2 Uranium extraction

2. The rock samples were crushed into fine sand. The low grade and medium grade samples were crushed using a disk mill while the high grade samples where crushed using a diamond drill bit in a protected room in a fumehood. A subsample of 10 to 100 grams was transferred to a Teflon beaker and a ~500fg of ^{233}U tracer was added gravimetrically from the stock, containing only ^{233}U with an activity of 9.28E-04 Bq/g.
3. The uranium was extracted from samples using 100 mL of aqua regia (4:1 ratio of HCl and HNO_3) at a temperature of 115°C for 24 hours in Teflon digestion tube in a fume hood. Due to the high calcite concentrations, the amount of aqua regia was adapted per sample until the solution would remain acidic. 100mL of aqua regia was added if the solution had a pH greater than 2 after a digestion of 24 hours and was left to digest again at 115°C for another 24 hours in a digestion fumehood.
4. The acid containing the extracted U was kept, centrifuged to eliminate particulates and filtered to remove the silicate minerals.
5. The uranium in the acid solution was separated from the solution by co-precipitating the U with iron (Fe) after adjusting the pH to values of 9 to 10 using NaOH.

4.1.3 Column separation

6. The precipitate was then dissolved in 4M HNO_3 acid to obtain a solution with pH of ~1 and run through a primed and activated UTEVA column. Each column is

composed of 2mL dry pack cartridge. The active sites in the UTEVA columns are diamyl amyl phosphate (DAAP), where the U is sorbed as U-nitrato complexes. The uptake of U in these columns depends on the concentration of nitric acid (HNO_3) in the sample (Horwitz et al., 1992). Figure 4.1 shows this dependency. Theoretically, the resin can uptake U up to approximately 37mg/mL of resin bed but it is recommended to use 20% of this capacity, hence less than 7.5mg U/mL of resin bed (Eichrom Industries Inc., 2016). The Fe concentrations in the samples also prompted a review of an older study where a quantitative recovery (~100%) of U with up to 50 mg Fe per sample was reported (Carter et al., 1999). Samples with expected higher concentration of Fe and U were loaded in multiple stacked columns according to the uptake and elusion possibility of the resin. The resin also permits the elution of different sorbed actinides by using the appropriate acid concentrations, shown in Figure 4.1 (Horwitz et al., 1992).

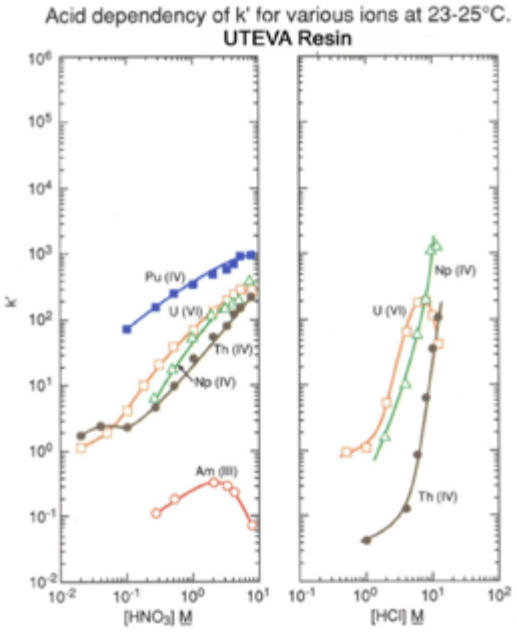

Figure 4.1: Diagram from Horowitz et al., 1992. The left diagram shows the high absorption of U(VI) by NHO_3 at 4M and above. The second diagram depicts the relationship of HCl with the column and the elements. A 4-6M HCl solution allows the selective elution of Thorium (Th) from the resin once the sample has been loaded. A low molarity of HCl allows the elution of U.

7. Each sample was loaded onto its own column(s), depending on the expected concentration of the sample. Each column was rinsed with 10ml 4M HNO_3/column to remove any Fe, then 5ml 6M HCl/column was added to remove thorium (Th).
8. The U was eluted using 10 ml 0.025M HCl/column and collected in a vial and dried to remove the HCl.

4.1.4 AMS Targets

9. The dried material was re-dissolved in 0.5M HNO_3 and 4 mg of Fe are added in the form of a $FeCl_3$ solution.

10. This solution was co-precipitated using pure NH_4OH to change the pH of the solution to 9 to 10 and the solution was then centrifuged. The precipitate was then collected and dried in an oven at ~100°C.
11. Once dried, the precipitate was weighted and calcinated in quartz cups at a temperature of 800°C to form uranium oxides (UO_2).
12. Once cooled, the samples were ground and mixed with a 1:1 or 1:4 pure aluminum (Al) powder; the first series of samples that were run with the AMS had a 1:1 mixture of samples to pure Al. Later in the third and forth series, it was found that stronger currents can be obtained using 1:4 mixture of samples to pure Al. In the last series, due to low counts with high grade samples, the mixture was brought back to mixture 1:1 of samples to pure Al. Once mixed, the samples were then loaded and pressed in copper targets.

4.1.5 Standards and blanks

We used bulk ^{233}U and ^{236}U to create our standards. This material was added to 10ml 0.5M HNO_3 and 4 mg of Fe are added in the form of $FeCl_3$ solution. This solution was co-precipitated using NH_4OH and centrifuged to remove the supernatant. The precipitate was collected and dried, then weighed and calcinated in quartz cups at a temperature of 800°C to form uranium oxides. Once cooled, the samples were then ground and mixed with a 1:1 or 1:4 pure aluminum powder, depending on the dilution needed and then loaded in copper targets. The results from these standards are also discussed at the end of this chapter.

Procedure blanks (also called column blanks) were created adding only the ^{233}U tracer. These blanks were used to test that no contamination was introduced during the sample preparation. 200fg of ^{233}U bulk were added to 10ml 4M HNO_3, and were run through the activated column. Steps 6 to 11 described previously in the sample preparation section above were then followed.

Machine blanks were also added to the AMS measurements by pressing an empty target. This ensures the level of contamination from sample to sample is monitored during the run.

4.2 The AMS set-up and how it works

The AMS is an analytical instrument that uses a tandem accelerator paired with a mass spectrometer to detect low concentrations of isotopes. A mass spectrometer by itself cannot distinguish between isobars, that is, isotopes of the same weight. By adding a tandem accelerator to the mass spectrometer, it allows the injected ions to be accelerated by changing their charge and allows molecules to be disintegrated due to Coulombic explosions; thus the remaining monoatomic ions gained energy and can be separated by energy-to-charge ratio levels and by mass. This method increases the sensitivity of the measurement by lowering the background noise, allowing the measurement of very low concentrations of isotopes. The following section describes the set-up of the instrument and what happens at each stage in the apparatus.

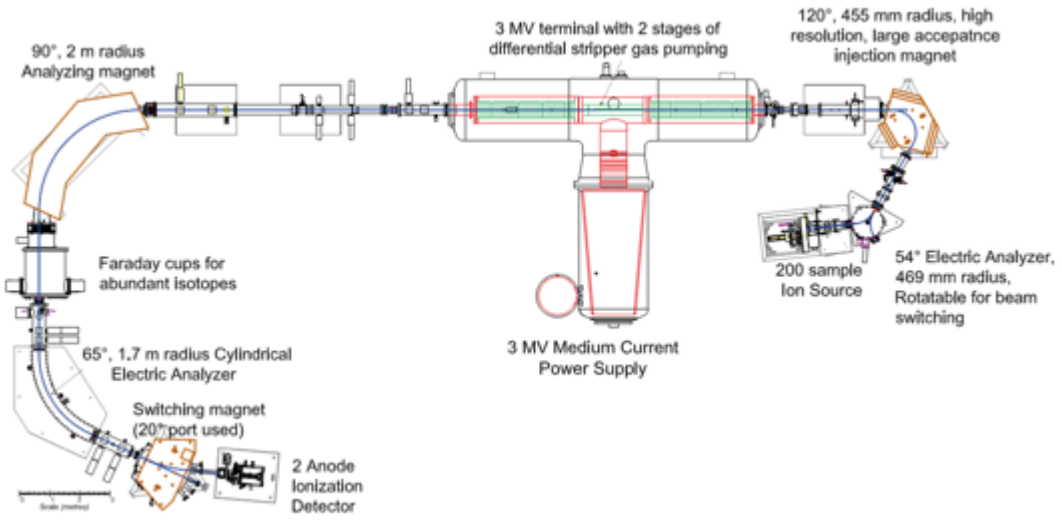

Figure 4.2: Overview of the AEL-AMS (modified from Kieser et al. 2015)

The AMS situated at the University of Ottawa in the A.E. Lalonde Laboratory (AELL) is equipped with a 200-sample carousel where our uranium oxides (UO_2) samples are inserted and kept in vacuum. A beam of ions (atoms with an electrical charge) is produced by a ^{133}Cs ion source and focused on the sample. In other words, the Cs gives up an electron to the U atoms in the sample thus making the UO^-, negatively charged ions. These negatively charged ions then go through a first stage of acceleration due to a voltage increase when they enter the spherical electrostatic analyzer. A first set of mass spectrometry takes place as the beam goes through a 120 degrees high resolution, large acceptance, injection magnet where it is bent to insure that only the ions with the wanted mass are selected, in our case the mass of $^{233}UO^-$, $^{234}UO^-$, $^{236}UO^-$ and $^{238}UO^-$. Throughout the AMS system, a low vacuum is maintained to ensure that the U ions travel through the beam line freely without any collisions.

The acceleration continues when the beam is then injected to the tandem accelerator where it is accelerated in 2 stages and goes through a stripper gas. In the tandem

accelerator, the central part is called a terminal, and it is charged to a high positive voltage. The negative ions are accelerated towards the positive terminal, being attracted to it. At the terminal, they pass through the stripper gas that strips them of one or more electrons and this process changes the charge on the ions to positive. The positive ions are then accelerated towards the end of the accelerator which is at the ground negative potential. By selecting a positive ion with a charge of +3 or higher (e.g. U^{+3}) in the accelerator, all molecules are disintegrated by Coulomb explosions in the stripper gas and only monoatomic ions are left in the beam.

Exiting the accelerator, the U^{3+} beam of ions passes through multiple focusing lenses while vacuum pumps maintain the vacuum at less than 10^{-7} Torr to ensure the free path for the ions. As the beam enters the second mass spectrometer part of the instrument, the ion beam is bent by an analyzing magnet, where the positively charged ions are separated based on their mass to charge ratio. The abundant isotopes (e.g.^{238}U and ^{235}U) are measured in Faraday cups situated right after the bending magnet. For the measurement of low number of ions of ^{236}U, the beam of ions passes through an electrostatic analyzer that selects particles based on their energy-to-charge ratio, to ensure that we are measuring only the right isotope. The beam line passes through a switching magnet and is counted in a gaseous ionization detector (Kieser et al. 2016). This detector counts individual ions as they come down the beam line.

4.3 Sample analyses and machine parameters setup

Samples were analyzed using the AMS. Multiple blanks, column blanks and standards where prepared and distributed in between the samples in the sample carousel. After the samples are loaded in the carousel and put under vacuum, the machine is tuned based on previous runs or on optics calculations. Table 4-1 below is a summary of the important parameters used in tuning. A more elaborate table can be found in Annex C.

Table 4-1: Setup parameters used to tune the AMS before and during the analyses of the samples

Parameters	Setup
Pilot tuning beam and record	$^{238}U^{16}O^{-} \rightarrow {}^{238}U^{+3}$
Tuning bouncer DC voltage (V)	349V
Cs (°C) and V_{tgt}/V_{ext}	IC=18A, 110°C and 7V/28V
Terminal voltage (kV)	2532.58 kV
Stripper pressure (mBar)	0.015 mBar
Positive ion detected	$^{236}U^{3+}$; $^{238}U^{3+}$; $^{233}U^{3+}$

Table 4-1 describes the ion that is selected, UO^{-} and the resulting isotopes that were analyzed $^{236}U^{3+}$; $^{238}U^{3+}$; $^{233}U^{3+}$; $^{234}U^{3+}$. The Cs source reservoir is kept at 110°C with a current of 18A. The terminal is set to 2.5MV and the stripper gas pressure inside the AMS is set to 0.015 mBar. The full tuning parameter table can be found in Annex C.

^{233}U, ^{236}U, ^{234}U and ^{238}U were measured in test samples and in the samples from Cigar Lake. These isotopes were analyzed sequentially by bouncing the AMS machine. "Bouncing" is the concept used to minimize the change to the set-up of the AMS machine in order to sequentially analyze different isotopes by keeping the same path through the whole apparatus for all isotopes that need to be analysed. The term refers to the sequential injection of the isotopes into the accelerator and it is the low energy, 120 degrees high resolution, large acceptance injection magnet that is bounced. The magnet is

illustrated in Figures 4.2 and 4.3. The vacuum chamber of the magnet is electrically isolated. Changing the voltage inside the chamber changes the energy of the ions that are passing through the magnetic field and allows the selection of the desired ion with different mass (Klein, Mous, and Gottdang 2004; Kieser et al. 2015; Southon, Nelson, and Vogel 1990). The mass selection is made by varying the voltage (V_B) applied to the chamber and can be explained by the following equation.

$$r = \frac{1}{B}\sqrt{\frac{2MV_B}{q}}$$

where r is the radius of the vacuum chamber that is a constant , B the magnetic field that we keep constant, q the charge of the ion that is also constant - all ions being UO^- with varying masses M ($^{233}UO^-$, $^{234}UO^-$, $^{236}UO^-$,$^{238}UO^-$) and the equivalent voltage V_B is varied to keep the equation constant. The cycling between voltages in called "bouncing". The initial tuning bouncer DC voltage for $^{238}UO^-$ is set at 349V.

In our case, we used slow sequential injection (SSI), a method that varies the voltage not only at the injection magnet, but also of the electrostatic analysers (where V_{EA1} = constant and V_{EA2} can be varied) and at the terminal (V_T), emplacement showed in Figure 4.3. The settings of all 3 parameters, (V_B, V_T , V_{EA2}) follow the rules as expressed in euqations (1), (2) and (3):

$$\boxed{M(V_{is} + V_B) = constant} \quad (4.1)$$

It is the "bouncing" voltage (V_B) that varies to accommodate the analyte isotope where M is the mass of the UO^- ion, and V_{is} is the voltage at the source that is constant.

As the negative ions UO^- are broken down into monoatomic, positively charged ions m^{+3} in the accelerator, the relation is energy based

$$\underset{(V_{is})}{M^-} \xrightarrow{V_T} \underset{(E_m)}{m^{+q}}$$

and the energy can be written as

$$E_m = \frac{m}{M}(V_{is} + V_T) + qV_T$$

where q, m and E_m are the charge (here $^{+3}$), the mass and energy of the emerging ion respectively. We have the next two relations that dictate the setting of the terminal voltage and the voltage at the electrostatic analyser EA2:

$$\boxed{mE_m = constant} \tag{4.2}$$

$$\boxed{V_{EA2} \propto \frac{E_m}{q}} \tag{4.3}$$

These 3 relations allow only the variation of the 3 voltages (V_B, V_T , V_{EA2}) to keep that same path for the different isotopes analyzed. When the voltage is the only variable that is changed, this strategy allows for minimal downtime between cycles.

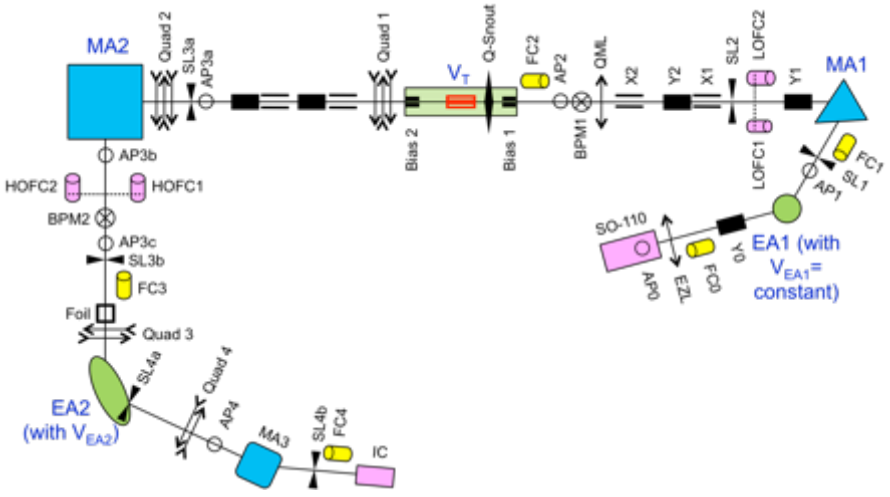

Figure 4.3: Diagram showing the different elements of the EAL-AMS.

4.3.1 Issues and problems

In our experiments, few instrumental issues have arisen when ^{236}U measurement in uranium ore was investigated. Before running the samples, multiple tests were done using standards in the AMS to eliminate as many of the technical and theoretical issues as possible. The samples were analyzed in series as the experiment progressed and the method was modified to accommodate the issues that appeared. This section touches upon all the issues that have emerged during our experiments and what was done to eliminate or diminish them.

One of the first issues we addressed was the possible false detection of uranium hydride ^{235}UH as ^{236}U by the electrostatic analyzer EA2. The mass of $^{235}UH^{+3}$ is very close to $^{236}U^{+3}$ (both about ~236 amu), as seen in Figure 4.4, and the ions can easily be confused for one another. To test if $^{235}UH^{+3}$ had disguising itself as $^{236}U^{+3}$, we measured the amount of $^{238}UH^{+3}$. As ^{238}U and ^{235}U are both natural occurring isotopes with 99.28% and 0.72% abundances respectively, measuring the amount of ^{238}U directly reflects the amount of ^{235}U and hence, the amount of detected $^{238}UH^{+3}$ reflects the amount of $^{235}UH^{+3}$. The amount of $^{238}UH^{+3}$ detected was not significant. This indicated that the amount of $^{235}UH^{+3}$ was also not significant when looking for the $^{236}U^{+3}$ isotope. Hence, it can be considered that the detection of $^{235}UH^{+3}$ as ^{236}U is negligible.

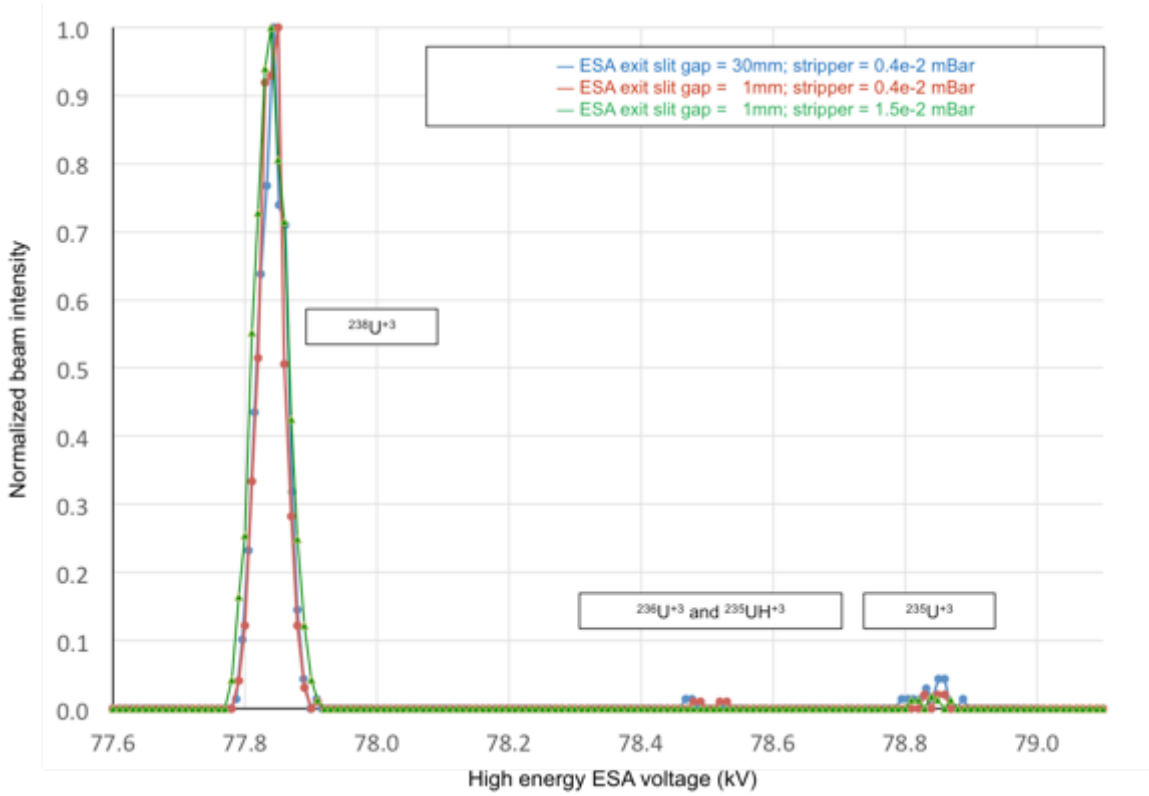

Figure 4.4: Summary of the high energy ESA performances for $^{236}UO^{-} \rightarrow {}^{236}U^{+3}$

Another potential issue taken into consideration was the presence of ^{235}U tailing that disguised itself as ^{236}U. To evaluate this potential error, a series of tests were done using the AMS, by monitoring masses 235.3, 235.6 and 235.9. The result showed that the counts at these masses were negligible, the tailing was not significant and so, did not disguise itself as ^{236}U. Hence, we can consider that the presence of ^{235}U tailing is negligible.

To increase the abundance sensitivity that we detected at about $1*10^{-13}$, narrowing the slits along the path of the beam and raising the stripper gas pressure was used. By raising the stripper gas pressure, it increases the number of collisions between the UO^{-}

beam and the gas, breaking more UO^- molecules and allowing the change of charge of more ions to U^{3+}. On the other hand, narrowing the slits eliminated unwanted masses that disguise themselves as UO^- or U^{3+} by allowing only the center of the beam to pass through and eliminating the dispersing ions.

Issues encountered during our AMS experiments included low current and irregular counting rates. Figure 4.5 (a,b,c) shows the typical current of ^{238}U for different samples. For low concentration samples, ^{238}U, ^{234}U, ^{233}U and ^{236}U were measured using the analytical detector but ^{238}U and ^{234}U over-loaded the detector and their measurement could not be used. This issue was solved for later samples by using the Faraday cups.

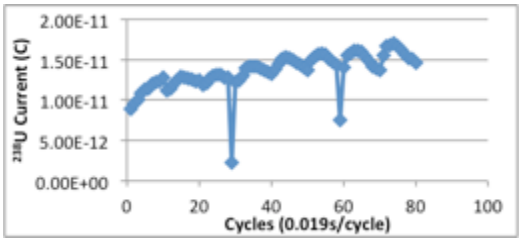

Figure 4.5 a: ^{238}U current for samples CL-M-01b, high grade, alteration halo of perched mineralization.

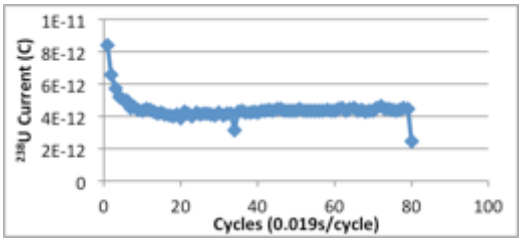

Figure 4.5 b: ^{238}U current for samples CL-M-48, high grade, ore sample. Current is low.

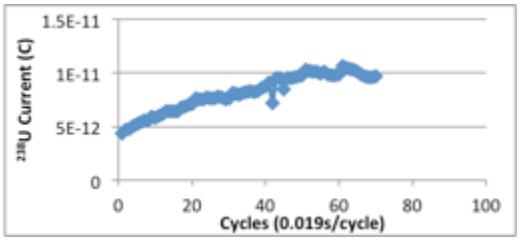

Figure 4.5 c: ^{238}U current for samples CL-M-50, mid grade sample, alteration halo of perched mineralization.

Figure 4.5 Typical current of ^{238}U for different samples

The mixing agent that was used to increase the conductivity of the samples could be one of the issues related to low currents. We used extra pure aluminum powder (Al) as the mixing agent. The Al powder itself seems to lead to low currents and possible contamination of the Al powder could lead to even lower currents. Changing the mixing agent could solve this issue. A preliminary study illustrated in Figures 4.6 and 4.7 show the current obtained with different mixing agents. From this study, Silicone (Si) seems to be a better mixing agent and will be further tested to see if it could be used in future experiments.

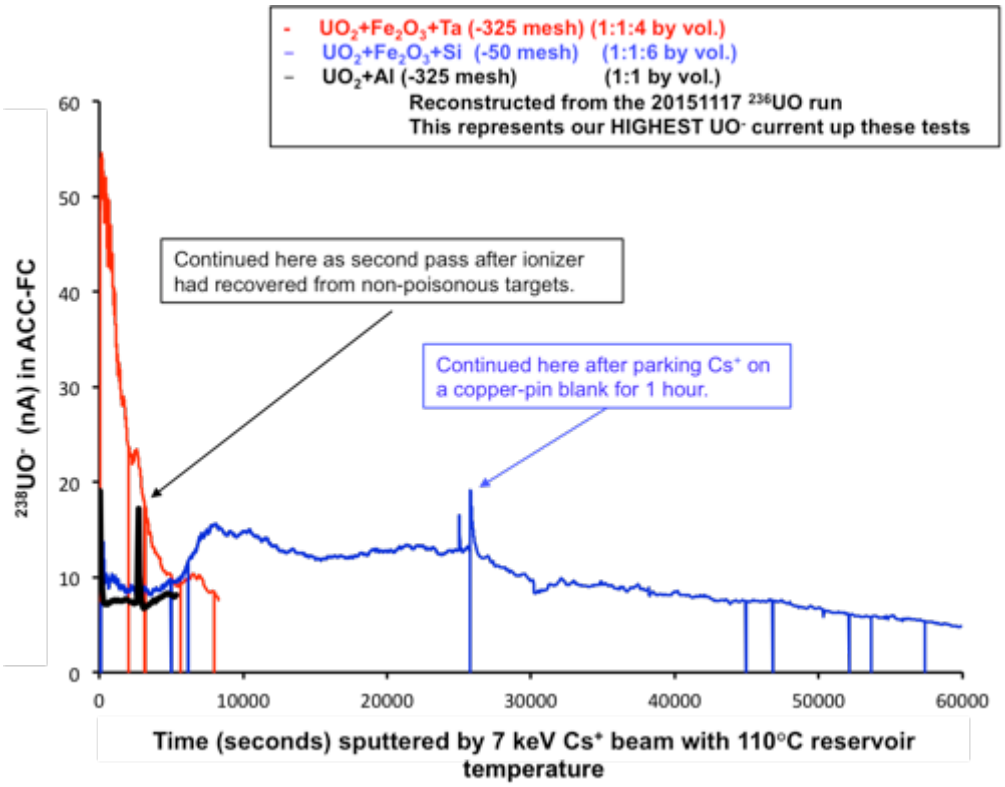

Figure 4.6: Comparison of Ta and Si for boosting UO^- current (Zhao, 2016)

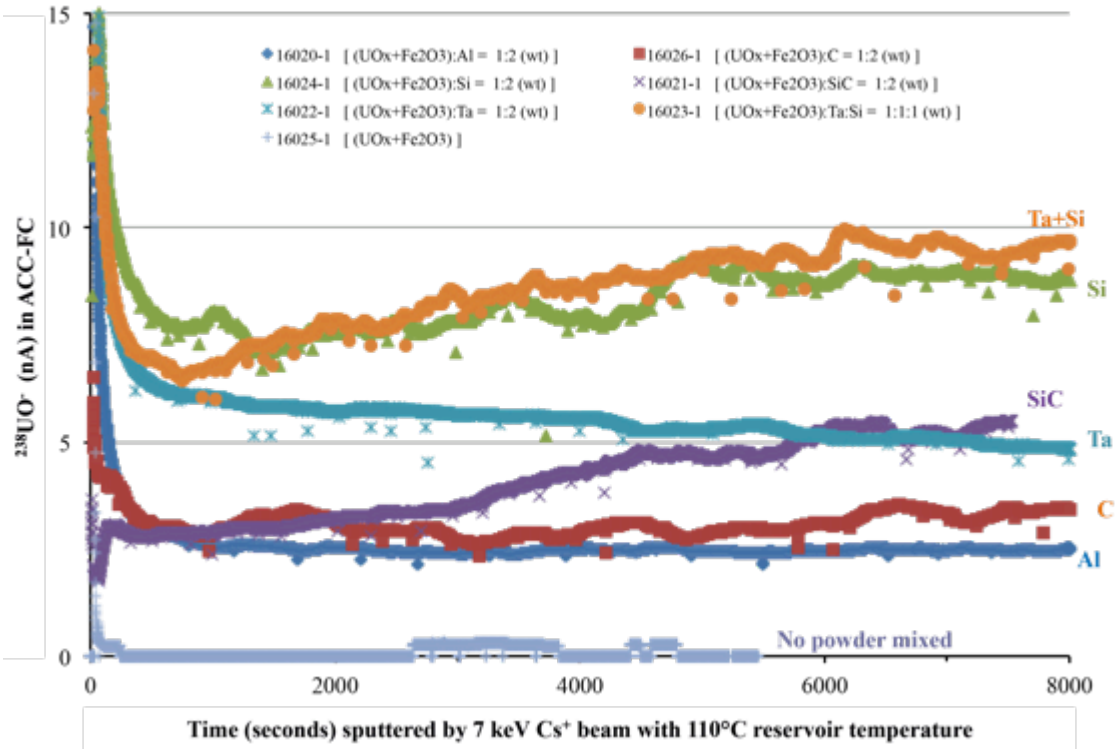

Figure 4.7: Comparisons of different powders for boosting UO^- current (Zhao, 2016)

Another potential source of the low current could be some sort of poisoning of the source during the analysis of higher-grade samples. Although not entirely understood, by cleaning the source and the line, this issue is somewhat reduced but remains present.

Another issue that arouse was a spiky background that appeared in the ^{236}U and ^{233}U counts. At this moment, this issue is also not understood and no solution can be brought forward.

4.4 Calibration and data processing

The first step in the calibration of the AMS measurements was to find the transmission loss of the $^{236}U/^{238}U$ ratio. Since ^{238}U is measured in a Faraday cup and ^{233}U

and ^{236}U in the gas ionization detector, there is more ^{236}U loss then ^{238}U. This is due to the fact that there is a different path length between the two detectors and that ^{236}U has to travel farther than the ^{238}U to reach the detector. We used a prepared standard with known quantities of ^{236}U and ^{238}U, analyzed it through the AMS and determined the difference in the ratio. This correction was then applied to the measurement made for each sample. The efficiency correction between ^{236}U and ^{238}U was found to be 1.75.

The second step in calibration was to measure the background of the machine and mixing agents. For this step we used three types of blanks: (1) A pressed empty copper target; (2) Ultra pure aluminum powder pressed in a copper target; (3) Iron Oxide pressed in a copper target. The summary of our results can be seen in table 4-2.

Table 4-2: Summary of the blanks used for calibration during the ^{236}U experiments using the AMS

Blank name	^{233}U Counts	^{236}U counts
15200-1 (Cu & Cu pin)	0	0
15200-2 (Cu & Cu pin)	0	0
15200-3 (Cu & Cu pin)	0	0
15200-4 (Cu & Cu pin)	0	0
15193-4 (Al blank)	0	0
15193-3 (Al blank)	0	0
15194-2 (FeO blank)	66	9
15194-4 (FeO blank)	89	2

It can be noticed the iron oxide gave some counts. Consequently, all samples were corrected for the blanks included in their run to eliminate any background from the sample processing and measurement procedures.

The third step of the calibration was to measure the background ^{236}U count from the preparation and measurement procedures. For this test, we used the procedure blanks

that were prepared in an identical procedure to the samples as explained earlier in this chapter. These blanks were analyzed by the AMS and some blanks gave counts. A mean of the counts was made and subtracted from the number of counts from each sample in that same run. Most procedure blanks gave no ^{236}U counts but in the first experiments and measurements, a little contamination was measured in the process blank samples. Table 4-3 summarizes the counts found for each procedural blank.

Table 4-3: Procedural Blanks used for calibration during the experiment

Name of Blank	^{233}U added (fg)	Counts of ^{233}U	Counts of ^{236}U
STD 2a	520	10015	92
STD 2b	520	18318	130
Bk1-2	520	8	0
BK2-1	520	342	0
BK2-2	520	247	0

STD2a and STD2b were run with low-grade samples, while BK1 and BK2 were part of the higher-grade sample run. In these tests:

(1) The ^{233}U count rate was much higher with low-grade samples because of the poisoning of the ion source by high concentrations of uranium;

(2) only in the low-grade sample run did we see any counts of ^{236}U.

The data obtained from the AMS runs was processed to calculate the amount of ^{236}U in the unknown samples by correcting for the ^{236}U background and the ^{236}U:^{238}U efficiency described above. The counts follow Poisson statistics. Samples with lower than 100 counts were eliminated because of the high statistical uncertainty.

4.5 Determining the concentration of ^{236}U (atoms/g), (pg/kg) and the $^{236}U/^{238}U$ ratio from the counts given by the AMS

To calculate the amount of ^{236}U in each sample, two slightly different methods were tested.

4.5.1 Method 1: using ^{233}U and ^{236}U counts

The first method utilized a calibration based on the known amount of ^{233}U that was added to the samples. Using the counts of ^{233}U and the counts of ^{236}U obtained from the AMS measurement, and knowing exactly how much ^{233}U was added, the amount of ^{236}U pg/kg of dried sample was established. Equation 4.4 illustrates this calculation.

$$[^{236}U]_{pg/kg} = \frac{\left(\frac{Counts(^{236}U)-BK(^{236}U)}{Counts(^{233}U)-BK(^{233}U)}\right)\cdot t\cdot tr(^{233}U)\cdot\left(\frac{Conv1}{Conv2}\right)}{amount\ of\ samples\ digested} \quad (4.4)$$

where, Counts(^{236}U) and Counts(^{233}U) represent the counts of ^{236}U and ^{233}U measured in the sample and BK(^{236}U) and BK(^{233}U) in the procedural blank that was part of the same run (as explained above in the calibration section). These counts represent the number of atoms observed in the time given. If the live time, the time of observation for both isotopes is not the same, a time conversion parameter is added (t).

$$t = \frac{livetime(^{236}U)}{livetime(^{233}U)}$$

tr(^{233}U) represents the amount of tracer added to the sample prior to digestion in atoms per sample. Conv1 represents the amount of fg/Bq of ^{236}U and Conv2 represents the amount of atoms per Bq of ^{236}U. These 2 conversion parameters allow us to calculate the amount of fg/sample of ^{236}U. This amount is then divided by the amount of sample digested in kg to obtain the result of how many pg/kg of sample we obtain.

To have this same result in terms of atoms/g of ^{236}U present, the following conversions was used:

$$[^{236}U]_{atoms/g} = \left(\frac{[^{236}U]_{pg/kg} \cdot 10^{-15}}{M_{U(^{236}U)}}\right) \cdot N_A \quad (4.5)$$

Where $[^{236}U]_{pg/kg}$ is the concentration of ^{236}U in pg/kg, $M_{U(^{236}U)}$ is the atomic mass of the ^{236}U isotope (236.045563 amu from Krane,1988) and N_A is Avogadro's number. Please note that the ^{236}U/^{238}U ratio was calculated based on the ^{236}U atoms/g and the concentration from SRC of ^{238}U in atoms/g converted from ppm using equation 4.10 below.

The error on the measurement of ^{236}U was calculated using counting statistics. In counting statistics, if an average number of events μ in a time interval Δt, the rate r can be written as $r = \mu/\Delta t$, and then we can express the mean as $\mu = r * \Delta t$.
In our case, the event is the detection of an atom, r is the count rate, the Δt IS the counting time, and μ the number of counts. Counting statistics follow Poisson distribution. In Poisson distribution, the mean μ equals the variance of the counts. The standard deviation on the counts, the error ($Er_{^{236}U(counts)}$), equals the square root of the variance of the counts (Var(μ)):

$$Er_{^{236}U(counts)} = \sqrt{Var(\mu)} = \sqrt{\mu} \quad (4.6)$$

Error on the counts of ^{236}U and ^{233}U was found and propagated through the different equations. This implies that samples with low counts will have high errors, on inversely that the higher counts a sample has, the lower the error on that measurement is. From the

laws of error propagation, the error on the concentration of ^{236}U (pg/kg) calculated with equation 4.4, $\mathrm{Er}_{^{236}U(pg/kg)}$ becomes:

$$\mathrm{Er}_{^{236}U}\left(\frac{pg}{kg}\right) = [^{236}U]_{pg/kg} * \sqrt{\left(\frac{\sqrt{\left(\mathrm{Er}_{^{236}U(counts)}\right)^2+\left(\mathrm{Er}_{^{236}U(BK)}\right)^2}}{Counts(^{236}U)-BK(^{236}U)}\right)^2+\left(\frac{\sqrt{\left(\mathrm{Er}_{^{233}U(counts)}\right)^2+\left(\mathrm{Er}_{^{233}U(BK)}\right)^2}}{Counts(^{233}U)-BK(^{233}U)}\right)^2} \quad (4.7)$$

And the error on the concentration of ^{236}U (atoms/g) calculated with equation 4.5 becomes:

$$\mathrm{Er}_{^{236}U(atoms/g)} = \left(\frac{\mathrm{Er}_{^{236}U(pg/kg)}\cdot 10^{-15}}{M_{U(^{236}U)}}\right)\cdot N_A \quad (4.8)$$

And for the ^{236}U/^{238}U ratio error, the error is calculated using the error of ^{236}U (atoms/g) calculated with equation 4.8 and the error ^{238}U from the SRC measurement. The error on the ratio $\left(\mathrm{Er}_{\frac{^{236}U}{^{238}U}}\right)$ becomes:

$$\mathrm{Er}_{\frac{^{236}U}{^{238}U}} = \sqrt{\left(\frac{\mathrm{Er}_{^{236}U(atoms/g)}}{[^{236}U]_{atoms/g}}\right)^2+\left(\frac{\mathrm{Er}_{^{238}U(atoms/g)}}{[^{238}U]_{atoms/g}}\right)^2} \quad (4.9)$$

4.5.2 Method 2: using ^{236}U/ ^{238}U ratio measured with the AMS

The second method was used when the ^{233}U count rate was very low due to sample dilution or if a poor current was produced from the target. In this method we used the concentration of ^{238}U of the samples measured at the SRC. Because the ^{236}U:^{238}U ratio could be calculated from the counts acquired via AMS, the number of atoms of ^{236}U was determined using the concentration of ^{238}U of the samples measured at SRC.

The first step was to convert the concentration obtained from SRC from ppm to number of ^{238}U atoms/g.

$$[\,^{238}U]_{atoms/g} = \left(\frac{[^{238}U]_{ppm}\cdot 10^{-6}}{M_{U(^{238}U)}}\right)\cdot N_A \tag{4.10}$$

where $[^{238}U]_{ppm}$ is the concentration of ^{238}U in ppm obtained from SRC, $M_{U(^{238}U)}$ is the atomic mass of the ^{238}U isotope (238.050785 amu from Krane,1988) and N_A is Avogadro's number.

To obtains the number of atoms/g of ^{236}U;

$$[\,^{236}U]_{atoms/g} = Ratio_{AMS}\cdot[\,^{238}U]_{atoms/g} \tag{4.11}$$

where the $Ratio_{AMS}$ is calculated for the counts made via AMS. To get this concentration in terms of pg/kg:

$$[\,^{236}U]_{pg/kg} = \left(\frac{[^{236}U]_{atoms}\cdot M_{U(^{236}U)}}{N_A}\right)\cdot 10^{15} \tag{4.12}$$

In this case, the error propagation is simpler. The error on the concentration of ^{238}U atoms/g is calculated as :

$$\mathrm{Er}_{^{238}U(atoms/g)} = \left(\frac{\mathrm{Er}_{^{238}U(ppm)}\cdot 10^{-6}}{M_{U(^{238}U)}}\right)\cdot N_A \tag{4.13}$$

The error on the concentration of ^{236}U (atoms/g) is calculated as:

$$\mathrm{Er}_{^{236}U(atoms/g)} = [\,^{236}U]_{atoms/g} * \sqrt{\left(\frac{Er_{Ratio_{AMS}}}{Ratio_{AMS}}\right)^2 + \left(\frac{\mathrm{Er}_{^{238}U(atoms/g)}}{[\,^{238}U]_{atoms/g}}\right)^2} \tag{4.14}$$

where the error on the ratio is estimated as the error on the ^{236}U counts.

The error on the concentration of ^{236}U (pg/kg) is calculated as:

$$\mathrm{Er}_{^{236}U(pg/kg)} = \left(\frac{\mathrm{Er}_{^{236}U(atoms/g)}\cdot M_{U(^{236}U)}}{N_A}\right)\cdot 10^{15} \tag{4.15}$$

The results of these calculations can all be found in Table D-1 in the Annex D.

4.5.3 Prepared Standards

To ensure the quality of the results, standards with known amounts of ^{236}U and ^{233}U were made. The results from these standards are summarized in Figure 4.8 and a detailed table can be found in Table C-2 in Annex C.

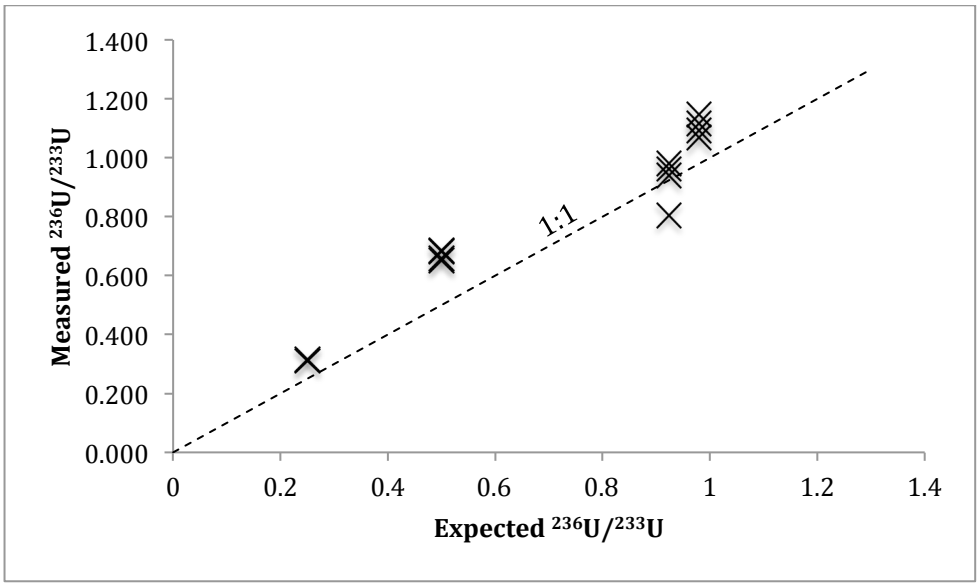

Figure 4.8: $^{236}U/^{233}U$ atom-to-atom ratio measured versus expected

It can be observed that when measured with the AMS, thes standards fall around the one to one line, but not exactly. Most standards show a slightly higher measurement than expected. Looking at individual samples, they deviate by 1.5% to 36% from the expected value, with and average deviation of 16.8%. This suggests a slight bias, meaning that the AMS measures more ^{236}U counts than ^{233}U counts compared the known amounts of ^{236}U and ^{233}U of the standard.

5 The Geology

The Athabasca basin is host to some of the highest-grade uranium deposits in the world. These deposits are all unconformity related deposits, implying that the main mineralization is at the unconformity between the basement rock and the sandstone overlying the granitic basement rocks (Ramaekers et al., 2007). These giant unconformity-related deposits are concentrated in pods situated at the unconformity and / or hosted right below it in the basement. A lot of the unconformity related uranium deposits in the Athabasca basin have the same characteristic traits: including general structural setting, age of mineralogy, host rock association mineralogy and geochemistry. The uranium deposits differ in size, intensity of alteration and associated clay minerals and mostly by the concentration of high grade uranium (U) mineralization (Bishop et al., 2016).

As Cigar Lake is one of the most explored deposits in the Athabasca Basin, this study has utilized it as a test subject to investigate the distribution of the isotope ^{236}U in a uranium deposit.

This chapter is an overview of the regional and local geology, with the description of the Cigar Lake deposit and of the alteration zone surrounding it.. The on-site location of each collected sample is specified with a quick description.

5.1 Regional Geology

The Athabasca basin is situated in Canada (figure 5.1), in northern Saskatchewan and northeastern part of Alberta. This section is an overview of the regional geology of the Athabasca basin, with an overview of its formation that has been well documented by numerous sources such as Card et al. (2007), Yeo et Delaney (2007) and Tran (2001) and others.

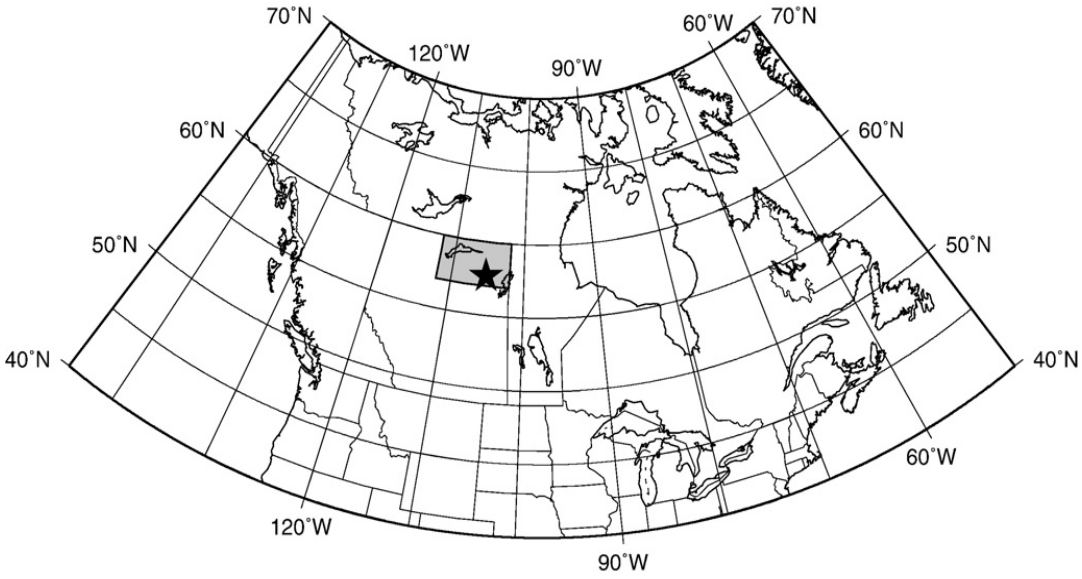

Figure 5.1 Map of Canada with the location of the Athabasca Basin and Cigar Lake. Taken from Farquharson and Craven, (2009). The dark square is the Athabasca Basin and the star is the location of the Cigar Lake ore deposit.

5.1.1 The Basement

On a geotectonic continental-scale, the Athabasca basin is situated on a remnant of the eroded Thelon-Taltson ca. 1.9 Ga orogenic belt and the Trans-Hudson ca. 1.8 Ga orogenic belt on the western Churchill structural Province (Card et al., 2007; Jefferson et al., 2007; Richard et al., 2011). It is composed of 3 major lithotectonic zones; the Archean Rae & Hearne provinces and the Taltson magmatic zone (figure 5.2). The Rae

and Hearne provinces underlie the basin in Saskatchewan while the Taltson magmatic zone underlies it only in Alberta (Card et al., 2007; Ramaekers et al., 2007).

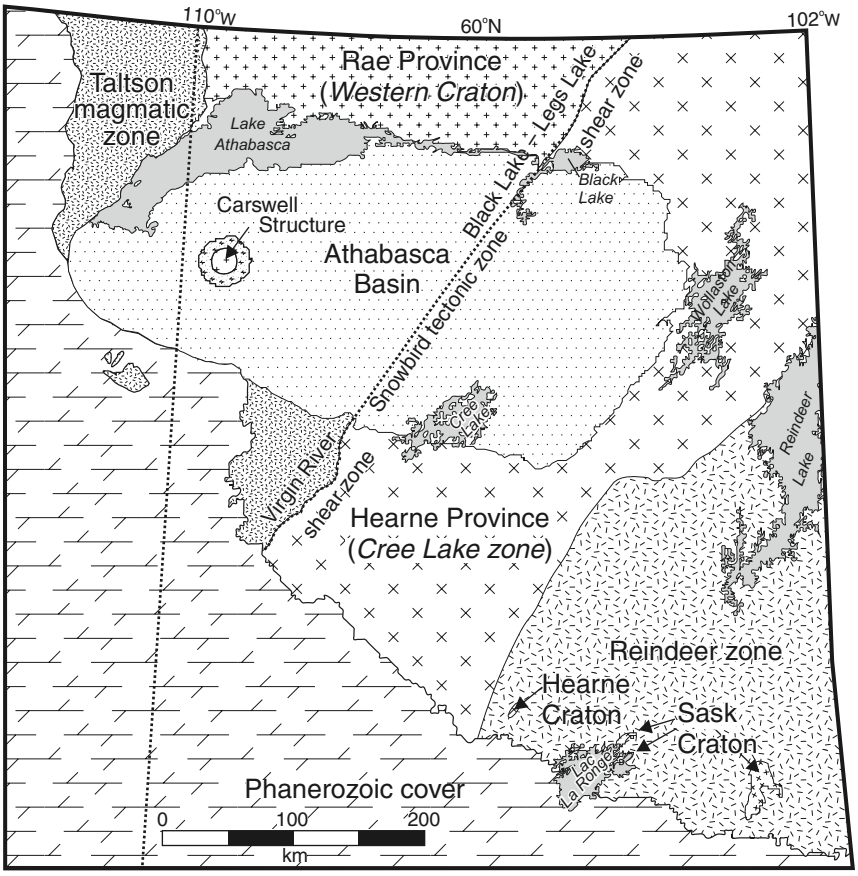

Figure 5.2: Major subdivisions of the exposed Precambrian shield in northern Saskatchewan and Alberta. (Card et al., 2007)

The Herne Province, also named Cree Lake Zone, on the eastern margin of the basin was further subdivided into the Mudjatik Domain, Virgin River Domain and Wollaston Domain (Card et al., 2007).

The evolution of the basement was described intensively by Card et al., (2007) and many others. In overview, the evolution was recorded to start at circa 3.05 Ga with the Neoarchean deformation and metamorphism of 3.0 Ga Granitoid rocks and Archean

supracrustal belts of the Rae and Hearne provinces. As early as ca. 2.45 Ga, metasedimentary basins such as the Hurwitz in the northern Hearne province, started forming on the craton (Card et al., 2007) and there is evidence that at ca. 2.3 Ga the Rae province was affected by granitic plutonism and metamorphism (Berman et al., 2000). The deposition of the Wollaston Supergroup at ca. 2.075 Ga on the eastern margin of the Rae-Hearne Craton marks the rifting and opening of the Manikewan Ocean (Yeo and Delaney, 2007). Between 2.02-1.90 Ga the Talston and Thelon magmatic zones were emplaced on the western margin of the Rae-Hearne Craton due to the collision of the Slave Craton with the Buffalo head terrane (Card et al., 2007). The Trans-Hudson orogeny ca. 1.92-1.77 marks the closure of the Manikewan ocean during which both provinces were subjected to thermo-tectonism (Card et al., 2007; Tran, 2001; Yeo and Delaney, 2007). The Mackenzie dykes emplaced at ca. 1.27Ga record the end of sporadic deformation of the region (Card et al., 2007).

During the ductile deformation that the regions underwent to accommodate both orogenies, several major shear zones developed. The Snowbird tectonic zone is one of the major structures (Card et al., 2007). This Paleoproterozoinc tectonic zone was first interpreted as the suture of the convergence between the Slave and Superior provinces (Hoffman, 1988), but reinterpreted as a shear zone by Hanmer (1997). The Grease River, Beatty River and Cable Bay shear zones and the Black Bay and Tabbernor faults are also major basin-transecting structures (Figure 5.3). These structures were reactivated periodically (Card et al., 2007).

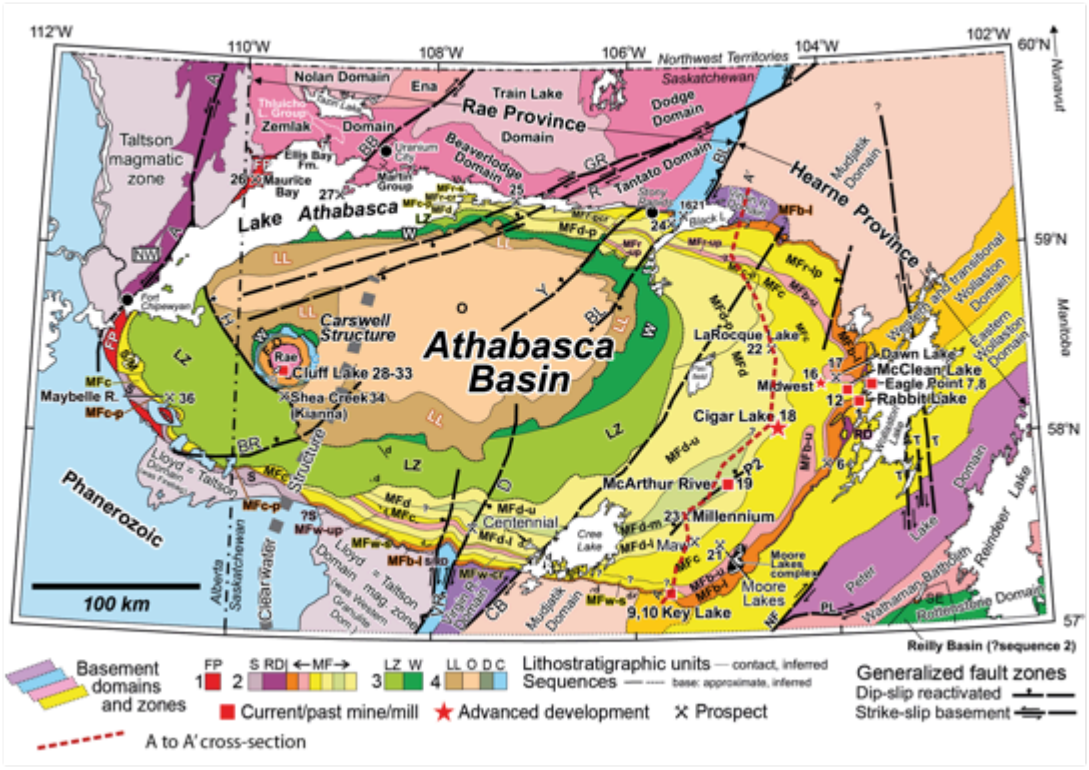

Figure 5.3: Geology and structures of the Athabasca Basin (modified from Jefferson et al.,2007), include the A-A' cross-section of figure 4.4 Legend C=Carswell, D=Douglas, FP=Fair Point, LL=Locker Lake, LZ=Lazenby Lake, MF=Manitou Falls (members: b=Bird (l=lower, u=upper) c=Collins, d=Dunlop, r=Raibl (up=upper pebbly), w=Warnes (up=upper pebbly)), O=Otherside, RD=Read, S=Smart, W=Wolverine Point, d=diabase. Members of LZ, LL, and O are indicated by lines and labels but only one shade is used per formation. "Wollaston-Mudjatik transition zone". CIS=Carswell Structure. Generalized fault zones include multiple ductile movements before deposition of Athabasca Group and brittle transcurrent and dip-slip movements during and after deposition; they are named as: A=Allan, BB=Black Bay, BL=Black Lake, BR=Beatty River, BU=Bustard, CB=Cable Bay, CH=Charlot, CHB=Charbonneau, CL=Charles Lake, CT=Clut, D=Dufferin, ER=East Rim, F=Fidler, FN=Fowler–Net Lake, GR=Grease River, H=Harrison, HT=Hudsonian thrusts (general trajectory), LL=Leland Lakes, MAY=Maybelle, NF=Needle Falls, PL=Parker Lake, P2=P2 fault at McArthur River, R=Richardson, RI=Riou, RL=Reilly Lake, RO=Robillard, RON=Robillard north, ROS=Robillard south, SL=St. Louis, T=Tabbernor, VR=Virgin River array (Dufferin is one named fault of many in VR), Y=Yaworski, YH=Yatsore-Hill Island. Arrays of faults with similar orientation and offset are indicated by colour groups.

5.1.2 Basin Geology

The basin is composed of the Athabasca group consisting of quartzose and fluvial sequences bound by unconformities. Four depositional sequences have been identified (Figure 5.4), that took place between ca. 1760 Ma and ca. 1500 Ma. Shallow marine strata are minor or cap the redbed sequences. The maximum basin thickness recorded of 1500 m is situated the center of the basin (Ramaekers et al., 2007) but was originally thought to be of about 5 km based on pressure–temperature estimates from fluid inclusions (Boiron et al., 2010; Derome et al., 2003). Figure 5.4 shows the basin stratigraphy. Summary of the different lithologies can be found in table 3 from Jefferson et al. (2007). For a more detailed information concerning the regional geology of the Athabasca basin see the references mentioned in this summary

5.2 Local geology

As mentioned above, The Cigar Lake uranium deposit is located at the unconformity between the middle Paleoproterozoic Wallaston Group and the late Paleoproterozoic to Mesoproterozoic Athabasca Group. The unconformity is defined by red hematitic paleoregolith resulting from paleoweathering. It has a vertical profile from a few cm to 220 m thick that has been overprinted by diagenetic bleaching and hematite alterations (Card et al., 2007).

The local geology was extensively documented by Bruneton (1993) and Fouques et al. (1986). At the location of the Cigar lake deposit, the Athabasca group is composed of the Manitou Falls Formation, subdivided in 3 units: D, C and B (Figure 5.4). The deposit itself is located in the MFB member, between 410 and 450 meters below surface.

The Manitou Falls Formation is approximately 400 m thick and covered by up to 55m of glacial till. This formation consists of a monotonous sequence of medium to coarse-grained sandstone units that is fining progressively upwards to the surface interpreted as braided stream fluvial deposit. For more information on the stratigraphy of the Manitou Falls formation see associated references.

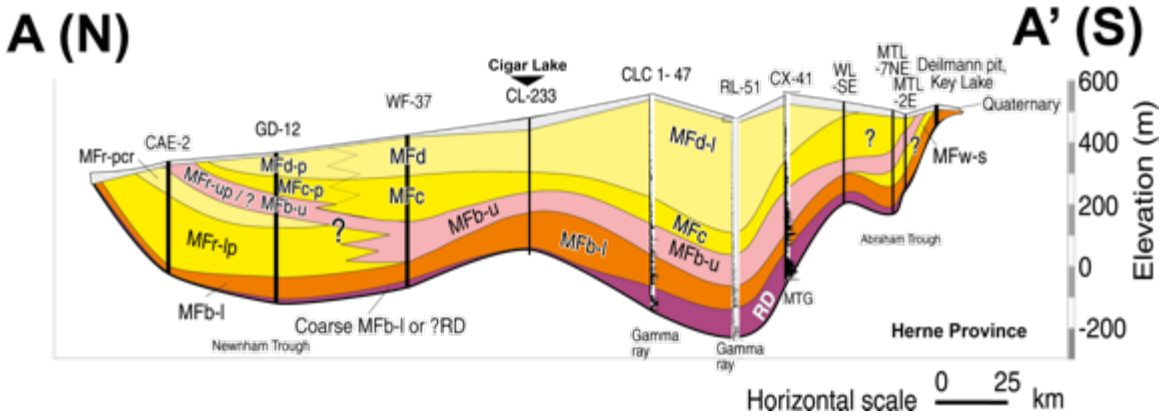

Figure 5.4: Cross-section of the Athabasca Basin taken and modified from (Ramaekers et al., 2007). The emplacement of the cross-section can be seen on Figure 5.3.

The basement is part of the Wallaston group and subdivided in 2 units: the first unit composed of graphite-bearing pelitic gneisses with biotites and corderite and the second unit composed of calc-magnesian gneisses with amphibole and pyroxene. The units are cross-cut by pegmatoids thought to be of local origin, probably from anatectic melting of the pelites. At Cigar Lake, graphitic gneisses are predominant and have been subdivided into two other units: augen-textured pelites unit ("augen gneisses") and a fine-grained pelite unit. The "augen-gneisses" form an east-west trending belt of about 100m meter wide that is bordered by the fine-grained pelite units. The fine-grained pelite units can also be found in thin horizons in the "augen-gneiss". The mineralized body lays on top of

the “augen-gneiss” belt. These units are thought to have attained upper amphibolite grade during regional metamorphism but have been intensely altered.

5.3 Alterations

For our study, the alterations are the most important part as the mineralization is linked to them. The basement has three types of alteration, two pre-Athabasca alterations and one post Athabasca formation. The sandstone basin has multiple hydrothermal alterations. All these alterations are intensively illustrated in Figure 5.5 and described by Fouques et al, 1986 and Bruneton, 1987,1993. The following section will summarize that information.

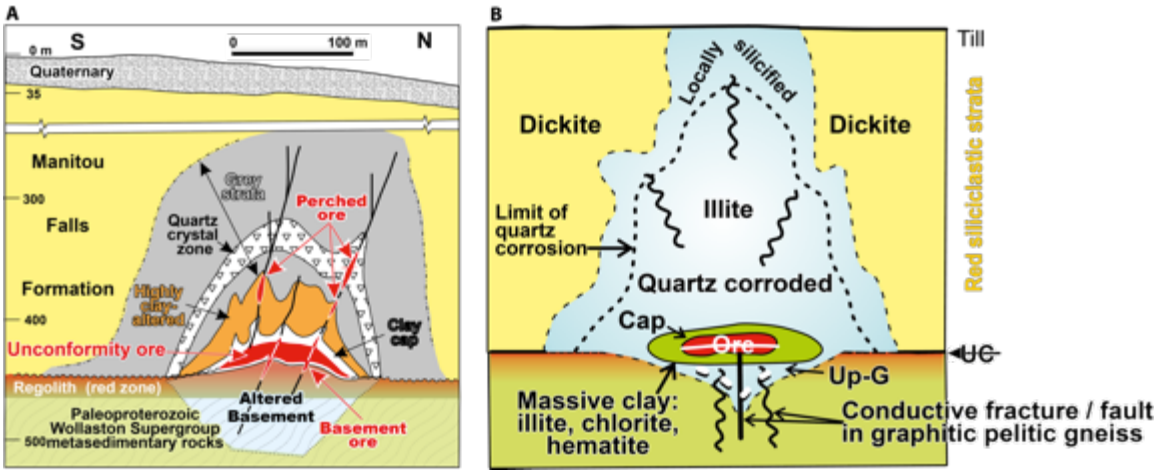

Figure 5.5: A - Alteration zones and B - associated alteration minerals, taken and modified from (Jefferson et al., 2007)

5.3.1 The basement

The first alteration that is visible in the basement, although not major, is the retrograde metamorphism. This retrograde metamorphism is characterized below the regolith by 3 mineral alterations: (1) the sericitization of cordierite and feldspar; (2) the

chloritization of cordierite; (3) slight chloritization of biotite, garnet and amphibole.

The second alteration is the pre-Athabasca paleoweathering. This paleoweathering is divided into 3 zones delimited by color: (1) *An orange to yellow zone* that is a thin (0.5 to 2m) to absent layer composed mainly of quartz grains floating in a kaolinite matrix present right below the unconformity.(2) *A red oxidized zone* that is a layer extending up to 25m below the sub-Athabasca unconformity composed of hematite (iron-oxides) and anatase (titanium-oxide), it is marked by a lack of graphite and sulfides and the metamorphic minerals have been replaced by clay minerals (kaolinite, illite and rarely chlorite). (3) The *green zone* is a layer that transitions between the red zone and fresh unweathered rock. It is a combination of retrograde and paleoweathering with the original textures and minerals still recognizable. Graphite and sulfides are present and the alteration minerals consist mainly of Mg-rich illite and Fe-chlorite.

The third type of alteration to the basement of the Athabasca basin is hydrothermal. It occurs around the orebody at up to 100m below the unconformity and obliterates previous alterations. Two different zones have been described, a *totally argillized* and *altered basement*. The *totally argillized basement* (also named massive grey-greenish clay zone) is located right below the richest part of the orebody. It is 1 to 3m thick, weakly mineralized and no original textures can be observed. It is composed of Mg-chlorite and Mg-illite and calcite is locally abundant. Graphite and pyrite are also not present in this zone. The *altered basement* differentiates itself with the fact that original textures are visible and that graphite and pyrite are present. In this zone, minerals such as biotite, amphibole, garnet and feldspars are strongly altered to Mg-rich and Fe-rich illite and Mg-Fe-rich chlorite and secondary minerals like Dravite and various phosphates are

widespread. The basement clays are dominated by sudoite and Mg-rich illite.

5.3.2 The basin

A hydrothermal alteration halo surrounds the ore deposit up to 300m upwards in the sandstone. Figure 5.5 illustrates the different alterations that the sandstone overlaying the ore body has gone through. These alterations are concentric.

From outermost to innermost zones, the zone that reaches the surface of the sandstone is called the *bleaching zone*, characterized by late limonitic alterations superimposed upon the bleaching.

The first *grey alteration zone* gets its name from the micro-disseminated iron sulfides that gives it the color. Hydrocarbons are also present in certain places.

The *quartz zone* is a zone of silicification where even fractures are filled with euhedral quartz crystals.

The second *grey alteration zone* differs from the first one as it is highly fractured and clays such as illite start appearing in the fractures and the sandstone matrix.

A highly *alterted clay zone* follows and is identified by its increase in clay content as it approaches the ore body. This zone contains up to 30% clay by volume, with the dominant clay mineral present being illite. This alteration is also distinguished by having local zones of quartz dissolution resulting in unconsolidated sand.

Surrounding the ore zone is the alteration named the *massive clay zone*. It caps the ore and is characterized by massive clay such as illite, siderite chlorite and kaolinite, as its name indicates it, with very little remnant sand left. The zone has areas of oxidation and can be weakly mineralized or have locally several percent U content.

The ore zone, also described by Bruneton (1987,1993) as the final alteration zone under the name *the massive ore zone*, consists of brecciated pitchblende associated with sulphides and sulpharsenites with a high U content that can exceed 50 percent over several meters. The zone has sharp contacts with the *argilized basement* and *the massive clay zone*.

5.4 The deposit

The Cigar Lake Uranium deposit is situated at approximately 40 kilometers west of the eastern margin of the Athabasca Basin in Saskatchewan, Canada, Cigar Lake (Figure 5.3). It is considered as one of the largest supergrade uranium deposit hosted in the Paleoproterozoic Athabasca basin ("IAEA UDEPO," 2016). It is an unconformity-related deposit implying that the main mineralization is at the unconformity between the basement rock, the middle Peleoproterozoic Wallaston Group and the overlaying sandstone basin, late Peleoproterozoic to Mesoproterozoic Athabasca Group (Bruneton, 1987).

The deposit contains massive mineralization formed as flattened elongated pods to continuous bodies of 2,150m long, 25 to 100m width and a maximum thickness of 20m. The main mineralization has been dated to 1.3Ga (Cumming and Krstic, 1992) and is developed along the basement-sandstone unconformity with intensive host-rock alterations (Bruneton, 1987; Jefferson et al., 2007). The Cigar Lake deposit is located at a depth of 410 to 450m depth. Secondary vein like mineralization occur as "perched", higher in the sandstone or lower in the basement (Bruneton, 1987; Fouques et al., 1986).

The known mineralization at Cigar Lake has been divided in two parts: the eastern part also named phase 1 and the western part named phase 2. Resources and reserves were estimated in 2016 by Cameco as described in table 5-1 and 5-2.

Table 5-1: Cigar Lake mineral resources as indicated by Cameco in the IN 43-101 report 2016, last updated December 31, 2016 (Bishop et al., 2016)

Category	Area	Total tonnes (x 1,000)	Grade % U_3O_8	Total M lbs U_3O_8	Cameco's share M lbs U_3O_8
Measured and indicated					
Measured	Phase 1	2.7	6.06	0.4	0.2
Indicated	Phase 1	17.5	7.59	2.9	1.5
Total measured and indicated		**20.3**	**7.38**	**3.3**	**1.6**
Inferred					
Inferred	Phase 1	42.4	11.17	10.4	5.2
Inferred	Phase 2	242.4	17.35	92.7	46.4
Total inferred		**284.7**	**16.43**	**103.1**	**51.6**

Table 5-2: Cigar Lake mineral reserves as indicated by Cameco in the IN 43-101 report 2016, last updated December 31, 2016 (Bishop et al., 2016)

Category	Area	Total tonnes (x 1,000)	Grade % U_3O_8	Total M lbs U_3O_8	Cameco's share M lbs U_3O_8
Proven	Broken	2.4	24.56	1.3	0.6
	Phase 1	223.7	21.91	108.1	54.1
Total proven		**226.1**	**21.93**	**109.3**	**54.7**
Probable	Phase 1	375.7	13.55	112.3	56.2
Total probable		**375.7**	**13.55**	**112.3**	**56.2**
Total reserves		**601.8**	**16.70**	**221.6**	**110.9**

The ore is composed mainly of uranium oxide in the form of uraninite and pitchblende (U_3O_8) that occurs as disseminated grains in aggregates and as lenses that can be a few meters thick with grades ranging up to 85% in a 0.5 meter interval (Bishop et al., 2016).

By consensus, it is believed that the mineralization took place when oxidizing brines, of marine origin, rich in U mixed with a reducing agent at the unconformity where deformation in the basement were present. It lead to a series of alterations and to the mineralization of U in a structural trap (Alexandre et al., 2009; Derome et al., 2003; Fayek and Kyser, 1997; Hoeve and Quirt, 1984; Kotzer and Kyser, 1995; Mercadier et al., 2012, 2010, Richard et al., 2016, 2011, 2010; Sibbald, 1985; Thomas et al., 2000). The origin of the U is still debated, as some believe that the U was leached from the U-bearing minerals in the basin such as apatite, zircon and monazite (Fayek and Kyser, 1997; Kotzer and Kyser, 1995) while others argue that the origin of the U is the basement (Derome et al., 2003; Hecht and Cuney, 2000; Mercadier et al., 2012; Richard et al., 2011). It is believed that the "perched" mineralization is due to reactivation of the faults and remobilization of the ore (Bishop et al., 2016).

Mineralization was recorded in three stages, from which the first two are considered hydrothermal in nature (Bruneton, 1993). The last stage of mineralization is much younger with estimated in age between 320 and 393Ma and is characterized by a low-temperature assemblage (Philippe et al., 1993). It is important to note that the clay matrix surrounding the ore has low-permeability but intersects with fractures (Cramer, 1986). The central part of the ore zone, however, is at least partially isolated from regional groundwater flow (Cornett et al., 1996).

5.5 Main Minerals and origin of Boron, Samarium and Gadolinium

As mentioned above, at Cigar Lake, the dominant clay mineral is illite. Kaolinite, sudoite (Al-chlorite), Mg-rich illite, Fe-chlorite, Mg-chlorite and an illite-chlorite mixed layer mineral are also present (Bruneton, 1987; Percival et al., 1993). Calcite may be locally abundant in the basement (Bruneton, 1987; Fouques et al., 1986).

As discussed, the ore is composed mainly of massive pitchblende; a sooty, cryptocrystalline, botryoidal form of uraninite (Jefferson et al., 2007).

Boron is mostly associated with the tourmaline (dravite) present in the deposit (Mercadier et al., 2012). In the deposit, dravite is in clay size and appears as disseminated in altered zones but concentrated along fractures (Jefferson et al., 2007). The dravite is associated with hydrothermal processes (Bruneton, 1993), the boron is thought to have been brought to the ore system by basinal brines of marine origin (Mercadier et al., 2012).

Sm and Gd are REE and are incorporated in alumino-phosphate-sulphate (APS) minerals that are rich in REE (Gaboreau et al., 2007; Jefferson et al., 2007; Mercadier et al., 2011). APS minerals have been documented around the deposits in the Athabasca Basin (Hoeve and Quirt, 1984). It is believed that APS minerals are part of the hydrothermal alterations and that they formed and are rich in REE that were released from the dissolution of phosphate minerals (principally monazite) in the basement rocks and in the basin during the syn-ore alteration processes (Gaboreau et al., 2007; Hecht and Cuney, 2000).

5.6 Location of samples collected

Samples were collected from 9 bore holes on site, to represent 3 different zones; (1) to be far away from mineralization; as background samples, (2) close to the mineralization; as core that was on top of the mineralization, as alteration samples and perched mineralization; and (3) core that stretched throughout the main mineralization, that encompassed alteration and ore samples. The location of these samples can be seen in Figure 5.6 illustrating the mineralization at Cigar Lake and the emplacement of the core that was used. You can find a description of the samples in Table B-1 of annex B.

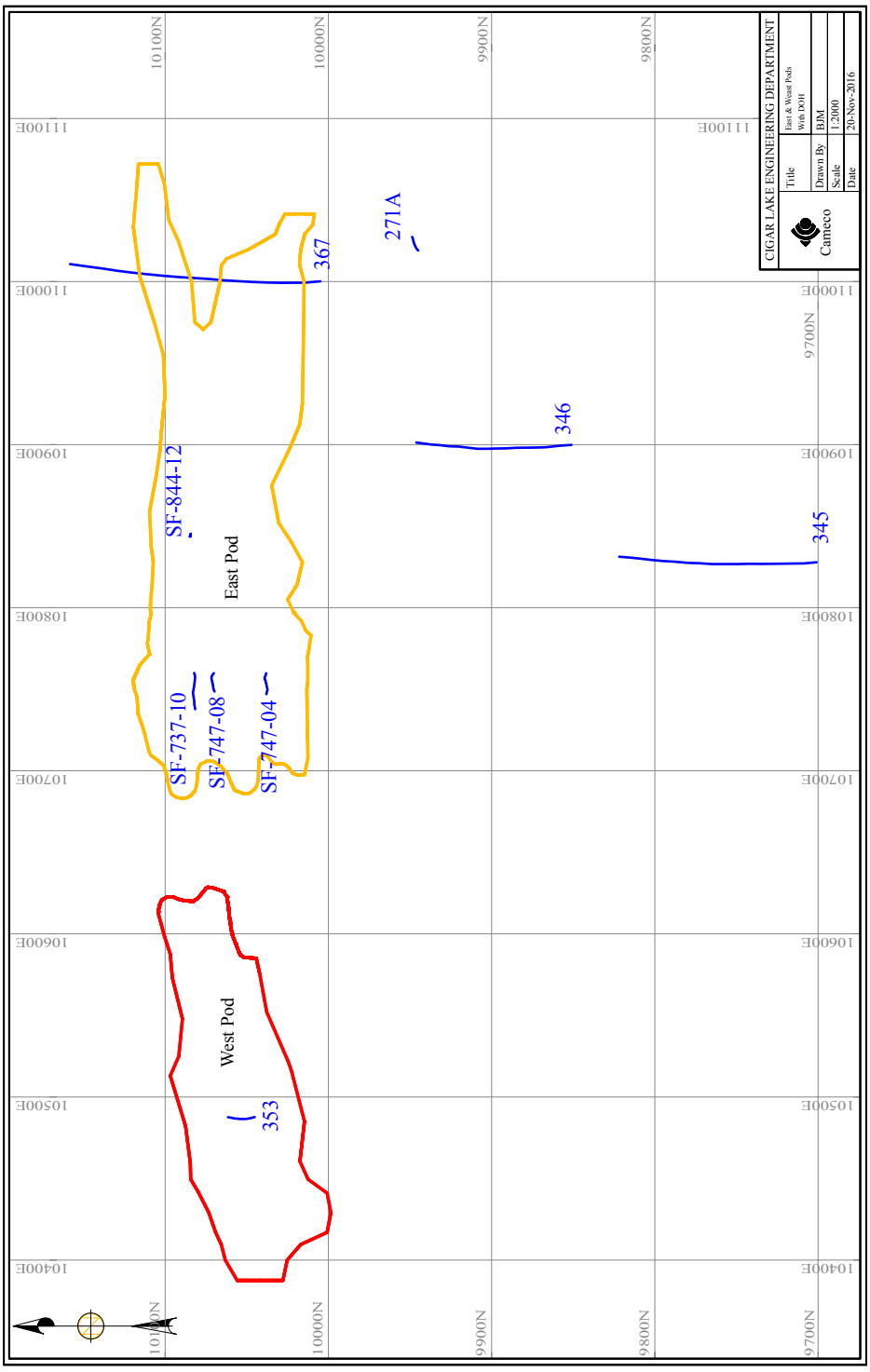

Figure 5.6: Plan view of the emplacement of the cores used in this study. Note that the samples collected are described in Table B-1 in Annex B above Legend: yellow phase 1 (eastern pod), red phase 2 (western pod). Figure sent from Cameco by Stephen Zubowski.

6 Elemental composition and testing the Prediction Model

This chapter will cover the methodology followed to run and test the predictive model built and described in Chapter 3. First, it will discuss the elemental results of the samples collected at Cigar Lake and described in Chapter 5, section 5.6, analyzed at the Saskatchewan Research Center (SRC) and the correlation between the uranium mineralization and the presence of the main neutron absorbers such as boron (B), samarium (Sm) and gadolinium (Gd). Then, it will address the ^{236}U concentration results obtained through the model and its relation to the neutron absorbers (U, B, Sm, Gd) to see how these absorbers influence the production of the ^{236}U isotope. The last part of this chapter will look at the sensitivity and error propagation in the model calculation to see how robust the prediction model is. Please note, ppm and ppb are used to describe all concentrations, where ppm is mg/kg and ppb is µg/kg.

6.1 Elemental composition and statistical distribution

To implement the model, all 60 samples collected at Cigar Lake were analyzed for elemental composition. Quantities of 10g of each crushed samples were sent and analyzed at SRC for major elements, light elements and B concentration. The elemental composition of the samples, limited to the main neutron absorbers U, B, Sm and Gd can be found in Table B-1 in annex B. Figure 5.6 in the previous chapter shows the emplacement of each core and Table B-1 in the Annex B describes the core, the depth and the geology of each sample.

In our set of samples, from the measurement done at SRC, the concentration of U varies from 0.64ppm to 662000ppm, the concentration of B varies from 8ppm to 1440ppm, the concentration of Sm varies from 0.55ppm to 1.33ppm and the concentration Gd varies from 0.73ppm to 161ppm. Figure 6.1 below shows the range of distribution of our samples on a histogram. Note that each element has a log-normal distribution for the samples. This means that the concentration of each element has a normal distribution throughout the samples but on the logarithmic scale, or in other words the logarithmic values of the concentration are normally distributed throughout the samples.

This is due to the fact that these are trace concentrations spawning across large variations. This said, ^{236}U concentration and $^{236}U/^{238}U$ atom-to-atom ratio will also have a log-normal distribution through the samples.

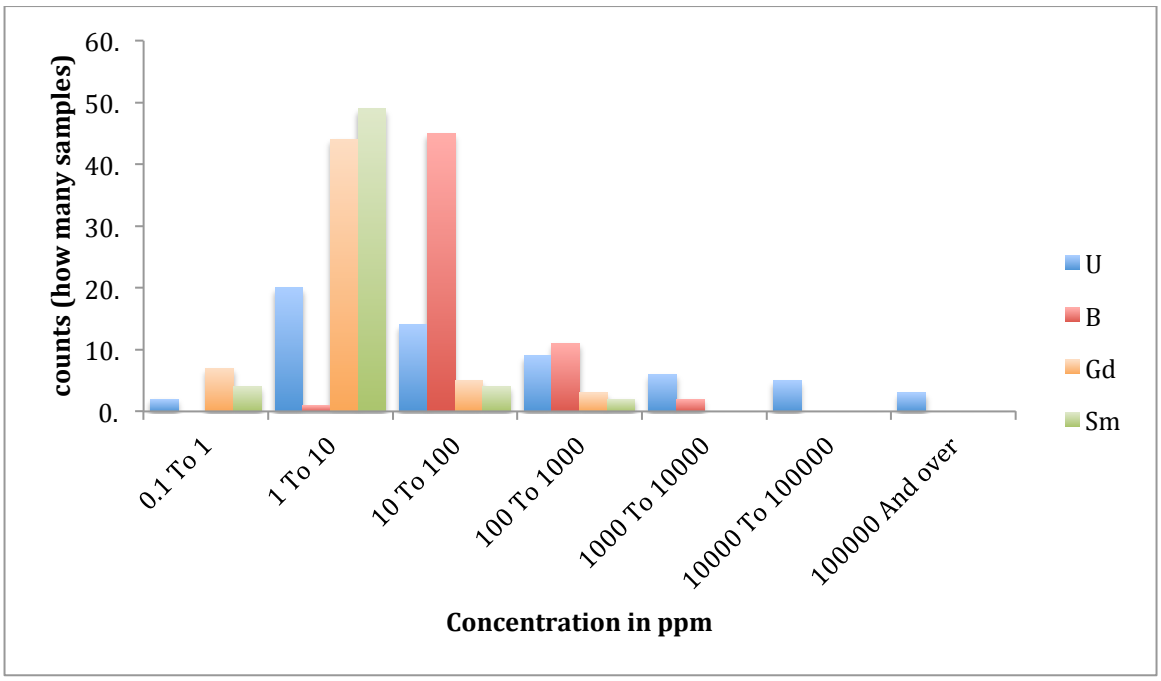

Figure 6.1: Log-normal distribution of the concentration of neutron absorbers in the samples

This information is important, as statistical analyses and regressions will be performed on the data. When two variables are compared and have log-normal distribution, statistical tests are done on the logarithmic value. This is done to eliminate the skewing in the data.

In a regression done on two variables with log-normal distribution, as said above, the regressions done on the logarithmic values and hence will be linear. The interpretation of this regression is the percent change in one variable to the percent change of the other. This can be written as: $\%\Delta Y = m * \%\Delta X$, where $\%\Delta Y$ and $\%\Delta X$ are our two variables and m is the slope of the linear regression done on the logarithmic values of X and Y.

6.2 Elemental correlation

First, we looked at the main absorbers, B, Sm and Gd vs the U concentration, to see if there was any correlation between them to appreciate if the distributions of these elements correlate to the concentrations of U. Not all the isotopes of these elements are high neutron absorbers, but the main absorbers have a natural abundance that varies around 15%, aka. ^{10}B (19.8%), ^{149}Sm (13.9%), ^{155}Gd and ^{157}Gd (14.8% and 15.7% respectively). Multiple statistical tests were performed on the data. All the statistical tests performed in this section can be found in Annex D.

6.2.1 Individual regression between B and U, Sm and U and Gd and U

Figures 6.2, 6.3 and 6.4 show the individual correlation of neutron absorbers B, Sm and Gd vs U. For each pair, a regression (visible in Figure 6.2 6.3 and 6.4) and a

statistical test were done. Individually, each element has a significant correlation with U, with a p-value of 0.003 for B, $1.047*10^{-7}$ for Gd and $5.2*10^{-7}$ for Sm at a confidence level of 95%. When only the main neutron absorbers are taken into account, the same p-values were observed; a p-value of 0.003 for ^{10}B, $1.047*10^{-7}$ for ^{155}Gd, $1.047*10^{-7}$ for ^{157}Gd and $5.2*10^{-7}$ for ^{149}Sm at a confidence level of 95%.

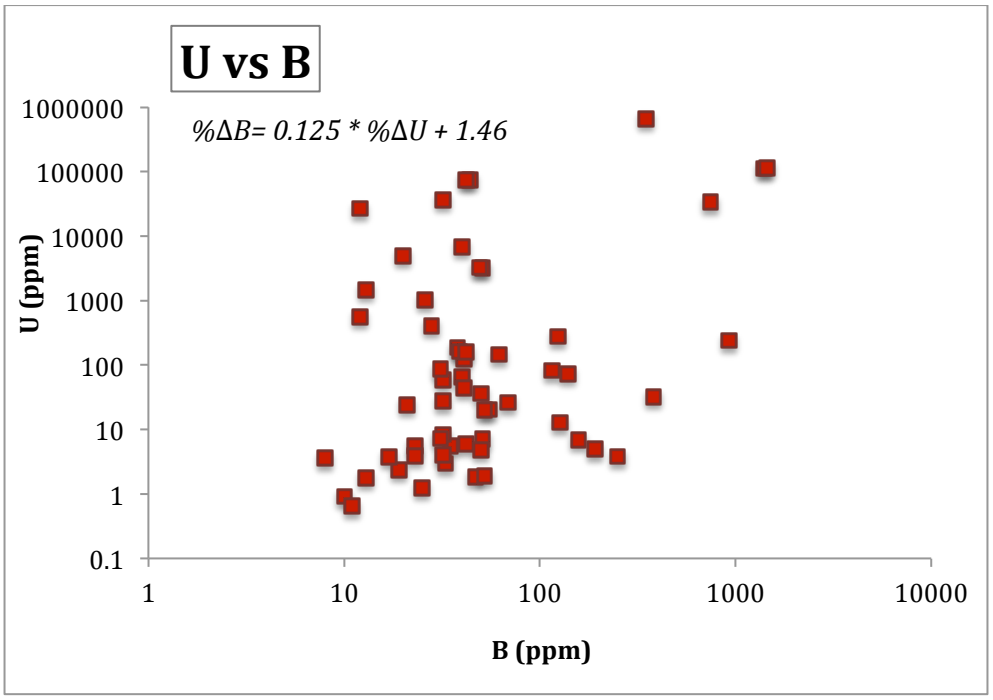

Figure 6.2: Correlation between the concentration of uranium and boron.

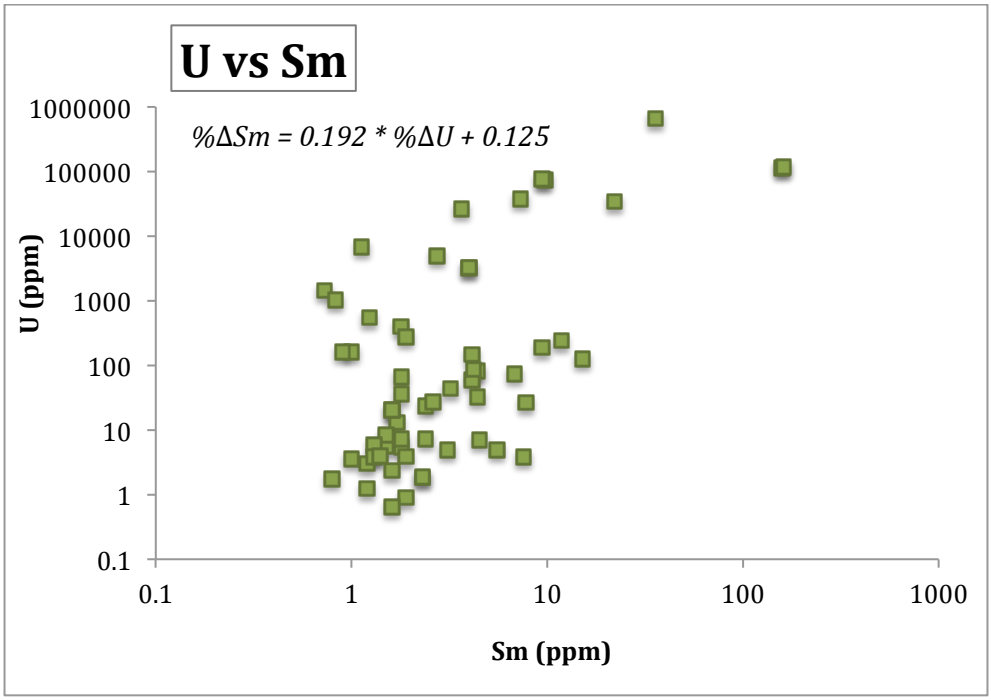

Figure 6.3: Correlation between the concentration of uranium and samarium.

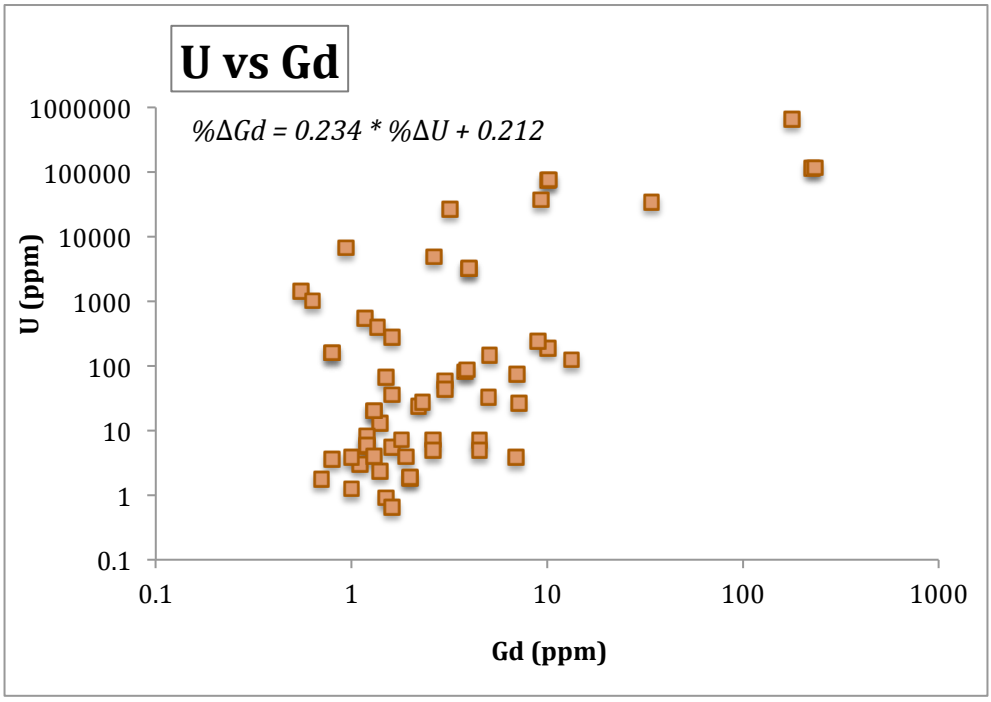

Figure 6.4: Correlation between the concentration of uranium and gadolinium.

6.2.2 Simultaneous regression of B, Sm and Gd on U

When statistically testing the correlation between U and all three absorbers B, Gd and Sm simultaneously using a multiple linear regression, the results show that only Gd had a significant correlation with U, with p-values of 0.266 for ^{10}B, 0.036 for Gd (^{155}Gd and ^{157}Gd) and 0.348 for ^{149}Sm at a confidence level of 95%.

6.2.3 Paired regression on U

Again, when tested in pairs against U (B and Gd, with a p-value of 0.187 for B and $4.79*10^{-6}$ for Gd; B and Sm, with a p-value of 0.272 for B and $3.00*10^{-5}$ for Sm; and Sm and Gd, with a p-value of 0.242 for Sm and 0.0357 for Gd), Gd is the dominant element that has a significant correlation with U with a 95% confidence. When paired just on the level of the neutron-absorbing isotopes against U,

6.2.4 Fission products

We also looked at the isotopes of Sm and Gd as decay products by fission from the U chain series, to see how much contribution U had to the presence of each of these isotopes. This was done based on the fission half-lives of each element and the age of mineralization. From the U concentration, it showed that the maximum contribution from the U fission was of 0.01% for the Sm isotopes ^{147}Sm and ^{149}Sm when the U concentration was greater than 40%. For all other isotopes, the contribution was less than 0.01% indicating that the origin of the isotopes is not the nuclear fission.

6.3 Results of the model

The concentrations of the major neutron absorbers discussed in Chapter 3 (B, Sm, Gd and U) were input for each sample in the template and the concentration of ^{236}U can be determined by the model. The calculations done in the prediction model are described in Chapter 3.

6.3.1 ^{236}U results

The model predicts that the concentration of ^{236}U varies between the lowest value of 0.188 ppq (10^{-15}) and the highest value of 0.2 ppb (10^{-9}) and in terms of atoms/g of ^{236}U varying between $4.8*10^{5}$ and $5.1*10^{11}$ atoms/g.

To compare ^{236}U to the U concentration, we use the ^{238}U isotope, as it is the most abundant of the natural occurring isotopes with an abundance of 99.28%. As explained above, ^{236}U and ^{238}U have also log-normal distribution through the samples. Looking at the concentration in atoms/g of ^{236}U versus ^{238}U as illustrated in Figure 6.6, there is a close correlation between them on the logarithmic scale. The linear regression $\%\Delta^{236}U = 0.954 * \%\Delta^{238}U - 8.81$ shows a tight correlation between ^{236}U and ^{238}U, where if ^{238}U changes by 1%, ^{236}U changes by 0.95%. Notice that the slope of the linear regression shows that ^{236}U increases at a slower rate than U. This indicates that other factors than the concentration of U have an influence on how much ^{236}U is produced.

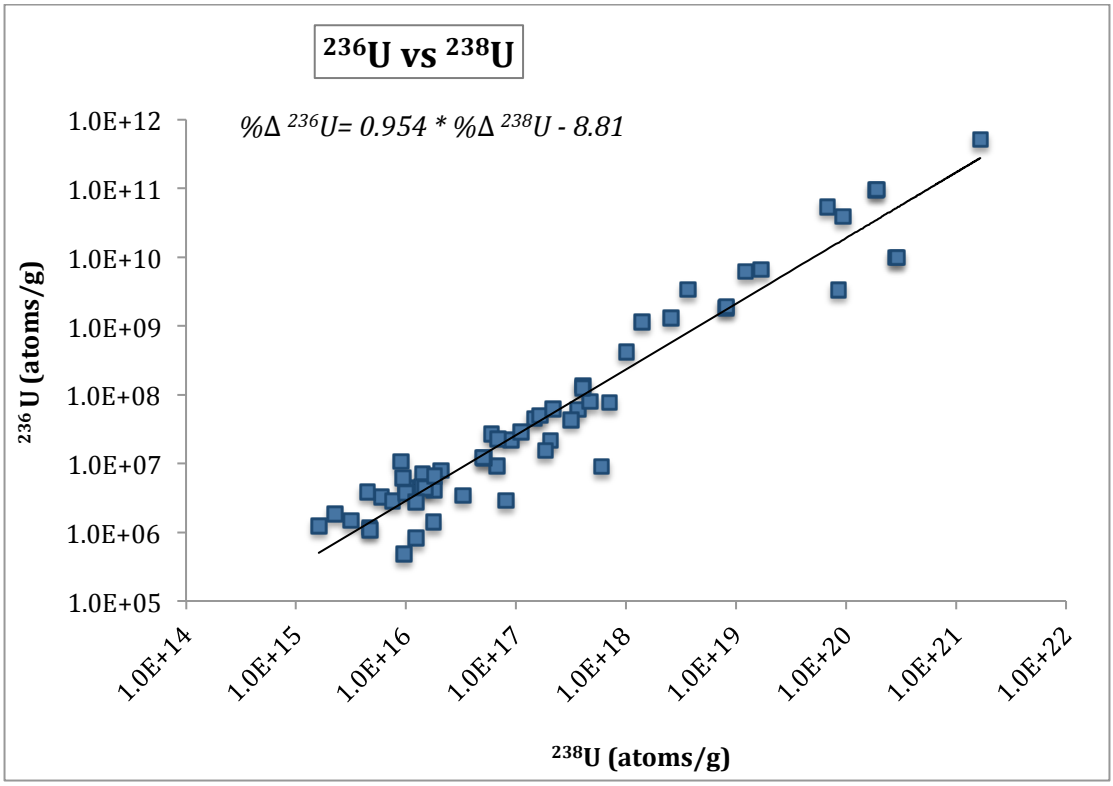

Figure 6.5: Model calculated ^{236}U vs ^{238}U, log-normally distrbuted, this figure shows the percent change in ^{236}U with the percent change of ^{238}U. The correlation shows that ^{236}U increases at a slower rate then ^{238}U.

6.3.2 The $^{236}U/^{238}U$ ratio results

The range of the $^{236}U/^{238}U$ atom/atom ratio results from the prediction model is illustrated in Figure 6.6 with lowest value at $1.4*10^{-11}$ to highest value of $1.2 * 10^{-9}$. Note the normal distribution is on the log scale.

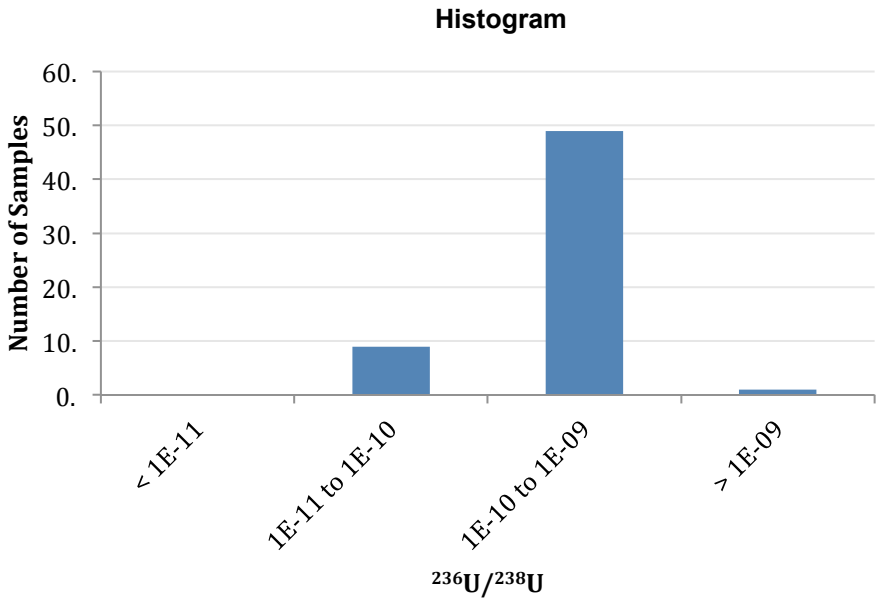

Figure 6.6: Histogram depicting the range of the $^{236}U/^{238}U$ ratio results from the prediction model. Note the logarithmic scale.

6.3.3 Correlation between $^{236}U/^{238}U$ atom/atom ratio and the absorbers B, Sm, Gd

To be able to see which one of the neutron absorbers had a big influence on the $^{236}U/^{238}U$ ratio linear regression was performed.

Figure 6.7, 6.8 and 6.9 show the individual linear regression done on the logarithmic values of the concentration of B, Sm and Gd versus the logarithmic value of $^{236}U/^{238}U$ ratio.

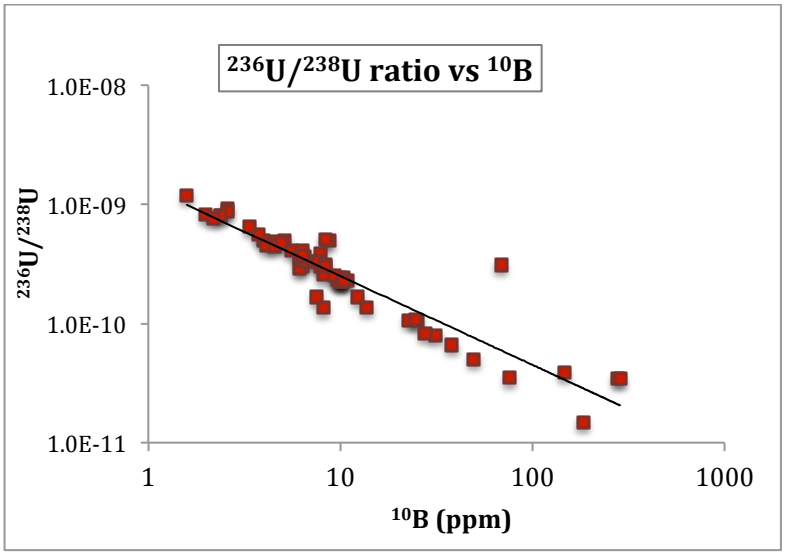

Figure 6.7: Correlation between $^{236}U/^{238}U$ atom/atom ratio from the model vs the concentration of B. Note the logarithmic scale and relation.

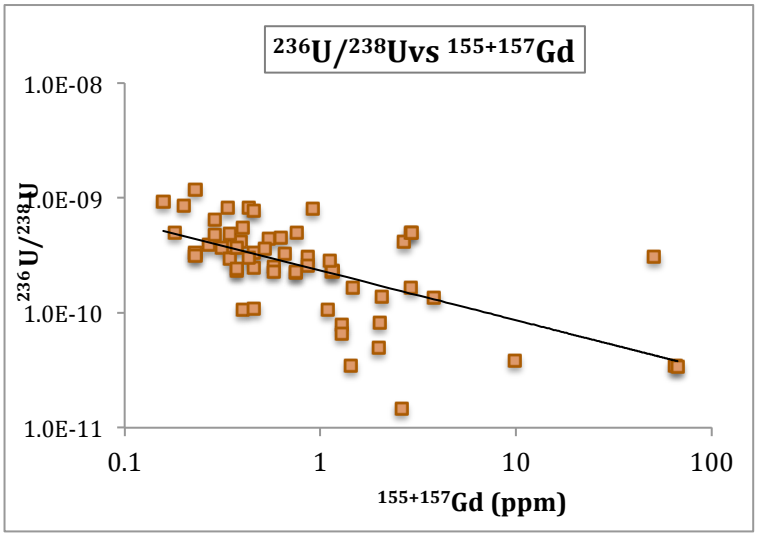

Figure 6.8: Correlation between $^{236}U/^{238}U$ atom/atom ratio from the model vs the concentration of Gd. Note the logarithmic scale and relation.

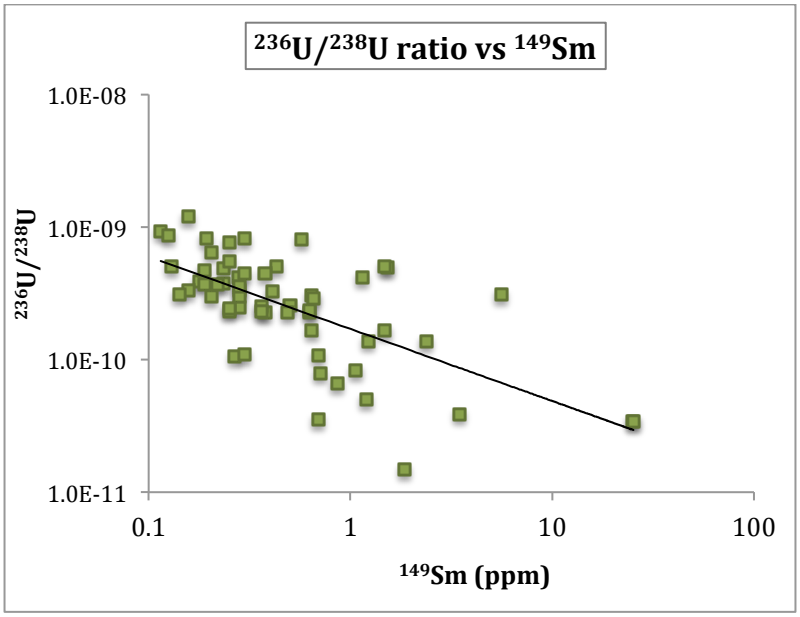

Figure 6.9: Correlation between $^{236}U/^{238}U$ atom/atom ratio from the model vs the concentration of Sm. Note the logarithmic scale and relation.

From the regression and as expected, all three elements have a correlation to the $^{236}U/^{238}U$ atom/atom ratio when tested at a confidence level of 95%, with p-values of 0 for ^{10}B, $3.4*10^{-7}$ for $^{155+157}Gd$ and $1.86*10^{-8}$ for ^{149}Sm. From the test, the sample correlation coefficient r, that represents the strength and the direction of a linear relationship between the two variables, is r = -0.93 for the correlation with ^{10}B, r = -0.65 for the correlation with ^{149}Sm and r = -0.61 for the correlation with $^{155+157}Gd$. Based on the sample correlation, B, Sm and Gd have strong negative correlations with the $^{236}U/^{238}U$ atom/atom ratio meaning that as the concentration of B, Sm and Gd increases, the $^{236}U/^{238}U$ atom/atom ratio decreases.

When statistically testing the correlation between the $^{236}U/^{238}U$ atom/atom ratio and all three absorbers ^{10}B, $^{155+157}Gd$ and ^{149}Sm simultaneously using a multiple linear

regression, the results of this regression also show that all three absorbers had a significant correlation with the $^{236}U/^{238}U$ atom/atom ratio at a confidence level of 95% with p-values of 0 for ^{10}B, $3.25*10^{-8}$ for $^{155+157}Gd$ and $4.77*10^{-7}$ for ^{149}Sm .

6.4 Error sensitivity

To be able to see how robust the model is, we tested it by introducing a 5% parametric error in the elemental composition measurements. We looked at the difference that adding or subtracting 5% of the concentration for each element, B, Gd, Sm and U would bring to the response of the model and the impact it would make on the final concentration of ^{236}U. Because this error is applied at the initial input set of values, it also tests how the error propagates through the system.

6.4.1 5% error in the B concentration

To test the impact of a 5% error in B concentration on the resulting ^{236}U concentration, the model is run three times, as illustrated in Figure 6.10. First with the concentration value of B analyzed at the SRC, second by adding a 5% error to the value from SRC and third by subtracting a 5% error to the value from SRC.

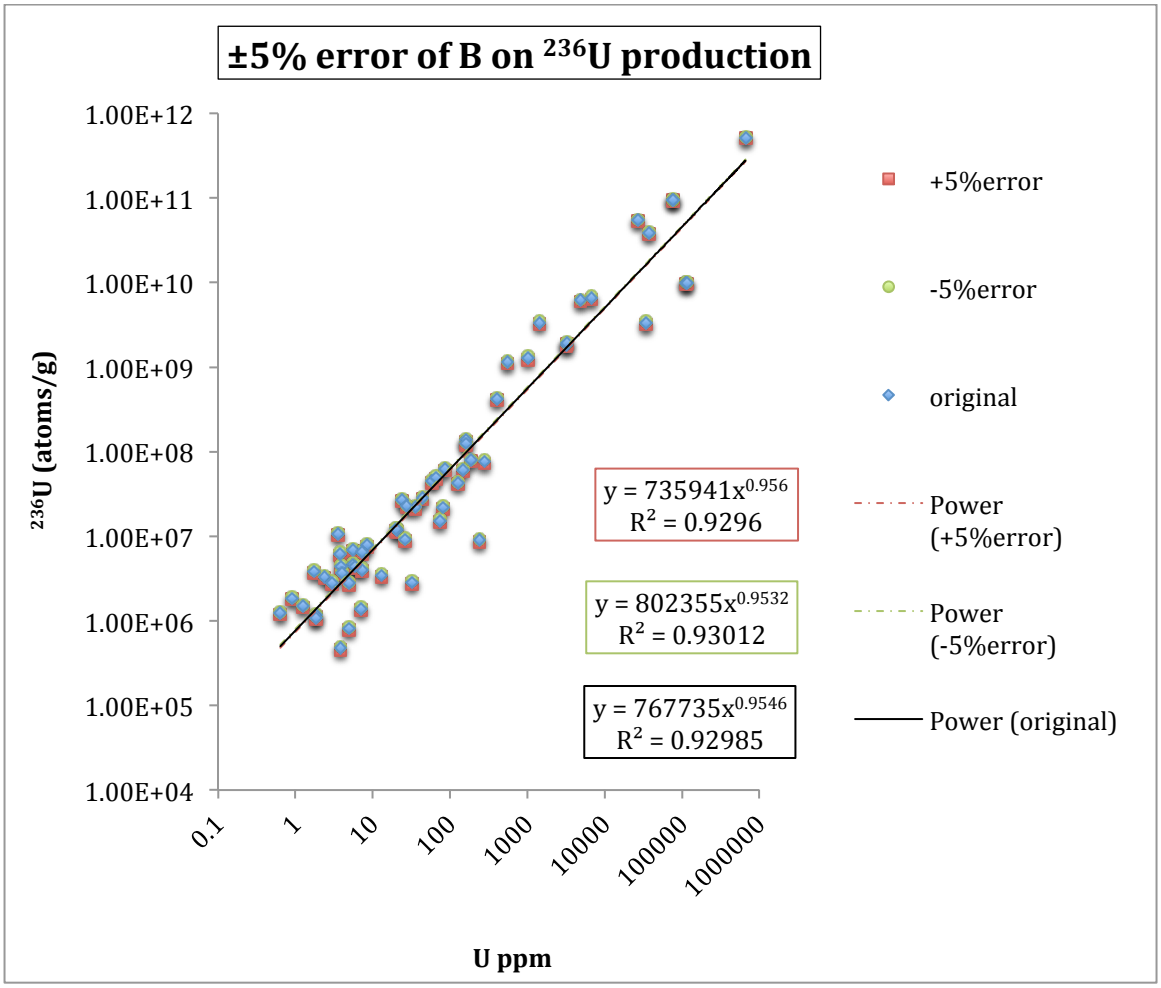

Figure 6.10: ±5% error in B concentration introduced to the calculation of ^{236}U production

When calculating the relative change (%) between the concentration of ^{236}U simulated with the error versus actual measurement, it can be observed that the absolute relative change varies with only maximum 5%, as illustrated in Figure 6.11 and 6.12, with averages of -3.6% to 3.8% relative change.

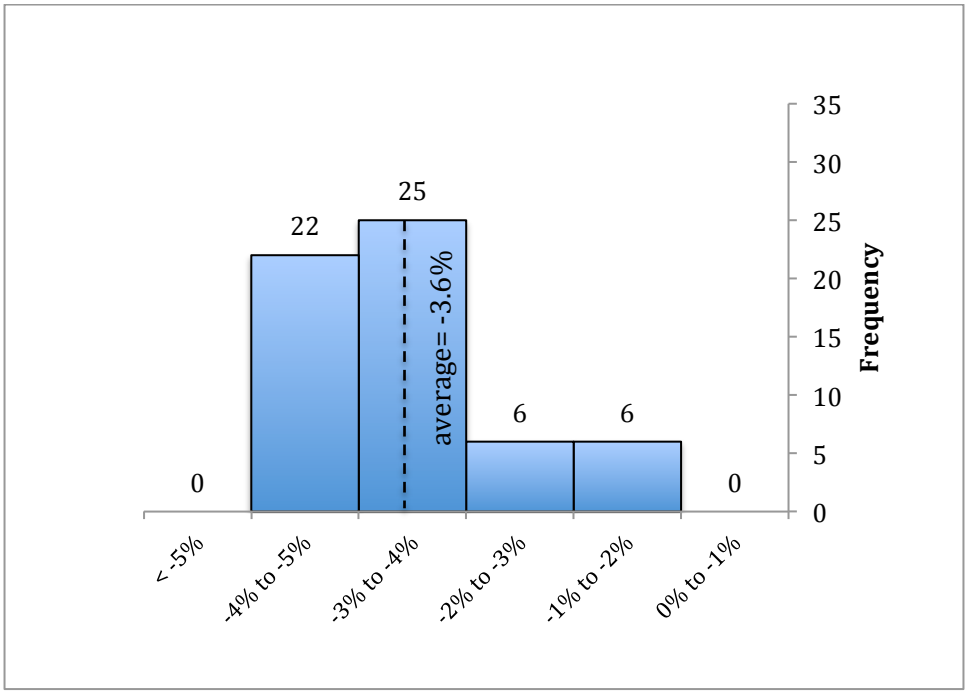

Figure 6.11: Resulting propagated error (relative change) of a +5% B concentration in the initial elemental composition.

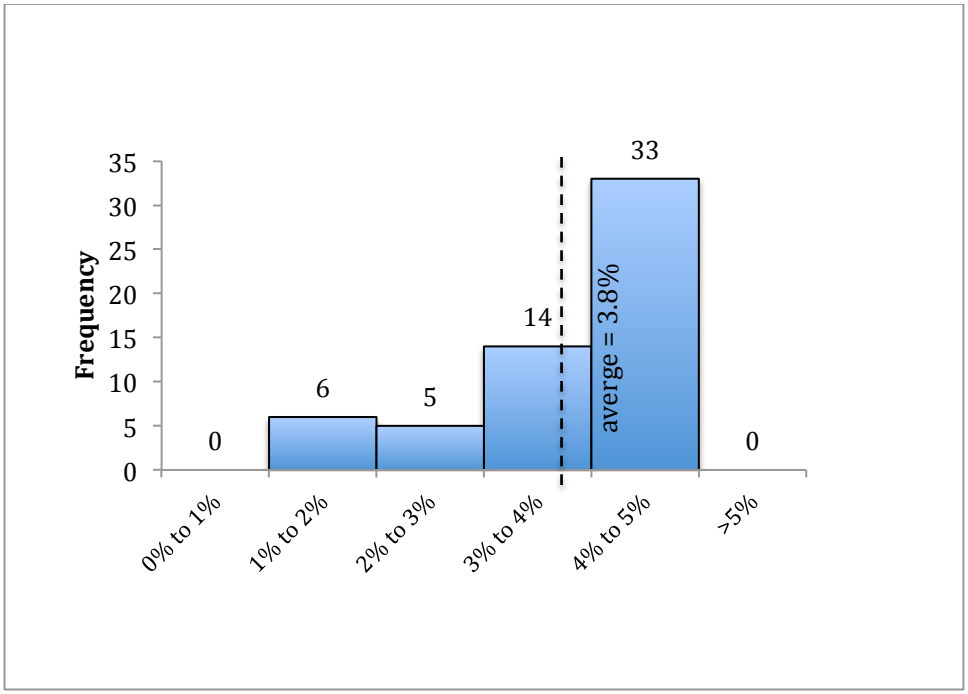

Figure 6.12: Resulting propagated error (relative change) of a -5% B concentration in the initial elemental composition.

By introducing this 5% error in the B concentration, we observe in Figure 6.10 that there is a moderate deviation with respect to the initial values; the resulting offset values changing by less than ±5% as seen in Figures 6.11 and 6.12 with an average error of ~3.7%.

6.4.2 5% error in the Sm concentration

To test the impact of a 5% error in Sm concentration on the resulting ^{236}U concentration, the model was again run three times illustrated in Figure 6.13. First with the concentration of Sm analyzed at the SRC, second by adding a 5% error to the value from SRC and third by subtracting a 5% error the value from SRC.

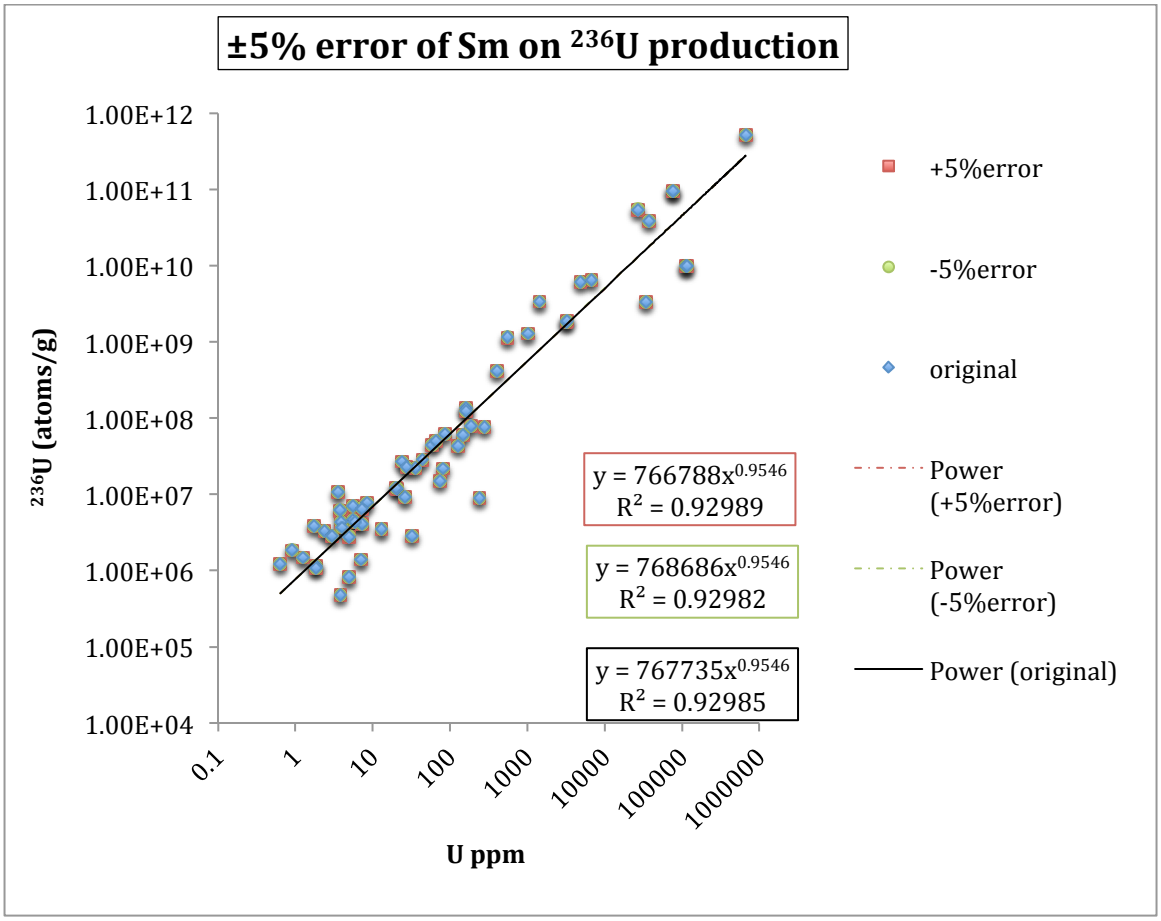

Figure 6.13: ±5% error in Sm concentration introduced to the calculation of ^{236}U production.

When calculating the relative change (%) between the concentration of ^{236}U simulated with the error versus actual measurement, it can be observed that the absolute relative change (%) varies with only maximum 0.4%, as illustrated in Figure 6.14 and 6.15, with averages of -0.13% to 0.13% relative change.

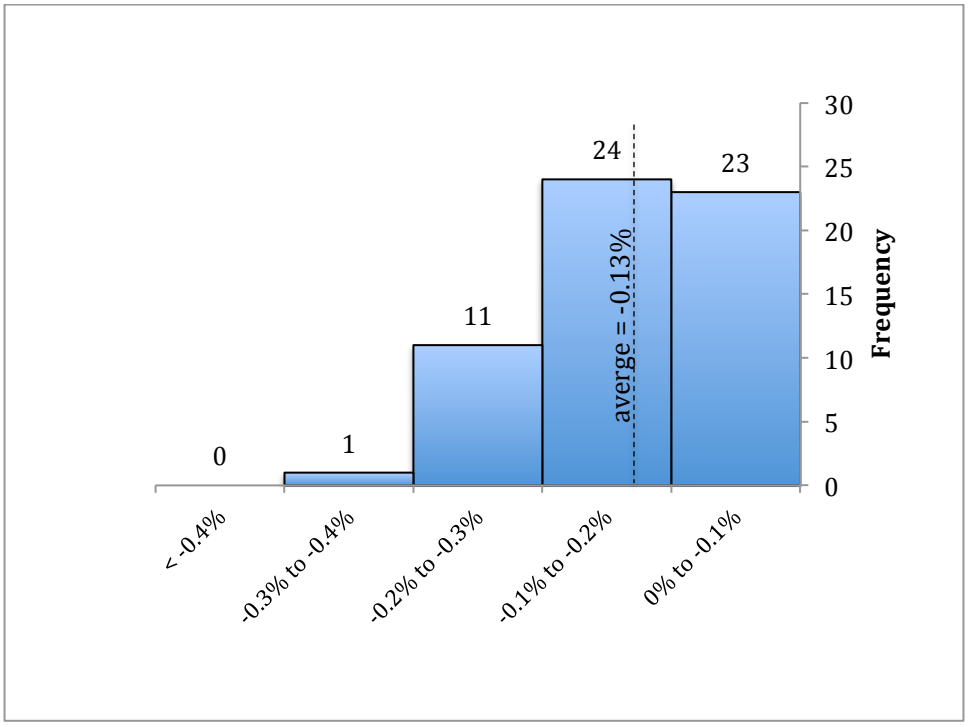

Figure 6.14: Resulting propagated error (relative change) of a +5% Sm concentration in the initial elemental composition.

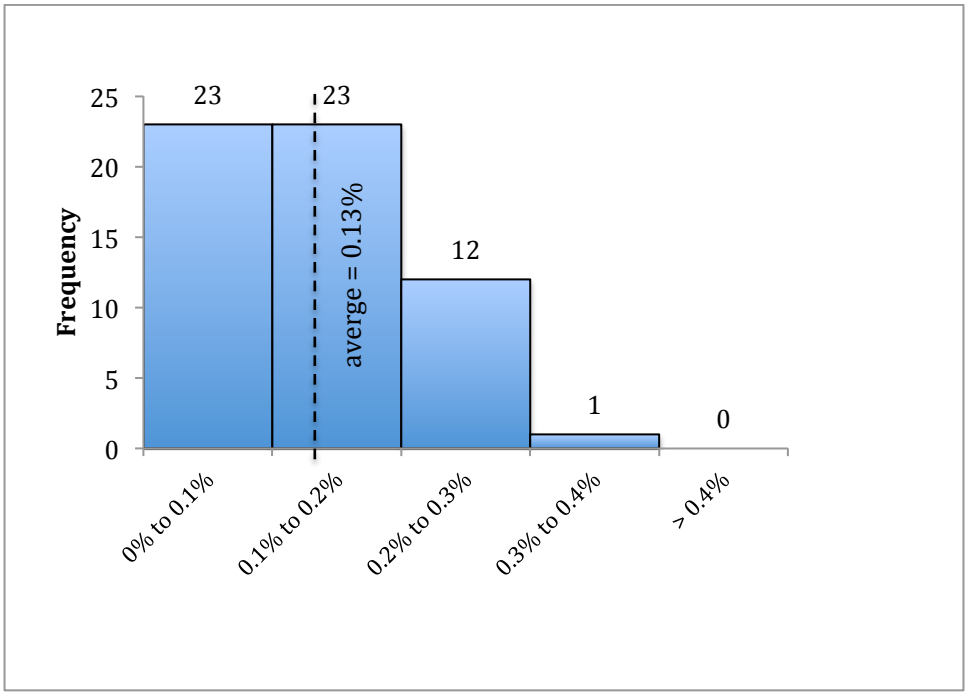

Figure 6.15: Resulting propagated error (relative change) of a -5% Sm concentration in the initial elemental composition.

By introducing this 5% error in the Sm concentration, we observe in Figure 6.13 that there is a moderate deviation with respect to the initial values, the resulting offset values changing by less than ±0.4% as seen in Figures 6.14 and 6.15 with an average of ~0.13%.

6.4.3 5% error in the Gd concentration

To test the impact of a 5% error in Gd concentration on the resulting ^{236}U concentration, the model is run three times as illustrated in Figure 6.16. First with the concentration of Gd analyzed at the SRC, second by adding a 5% error to the value from SRC and third by subtracting a 5% error to the value from SRC.

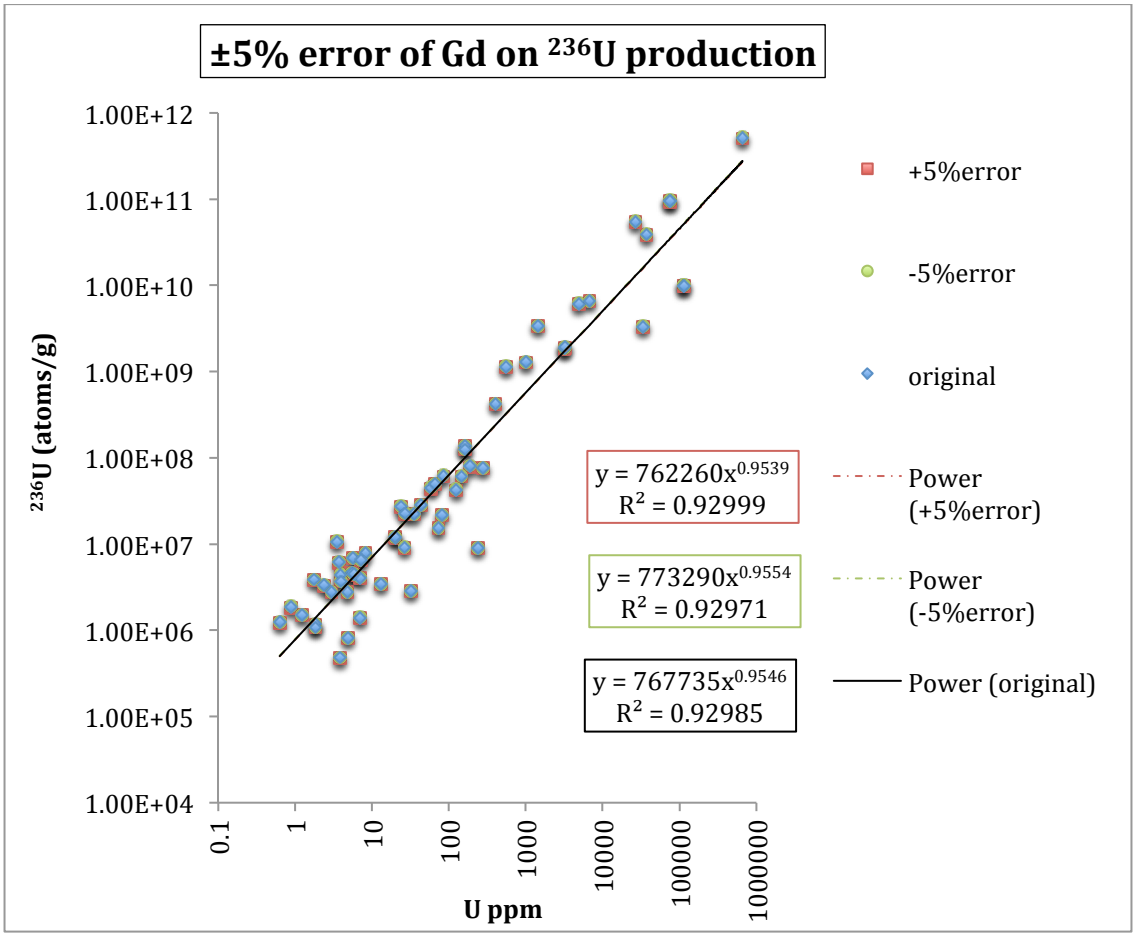

Figure 6.16: ±5% error in Gd concentration introduced to the calculation of ^{236}U production

When calculating the relative change (%) between the concentration of ^{236}U simulated with the error versus actual measurement, it can be observed that the absolute relative change (%) varies with only maximum 3%, as illustrated in Figures 6.17 and 6.18, with averages of -1.0% to 1.1% relative change.

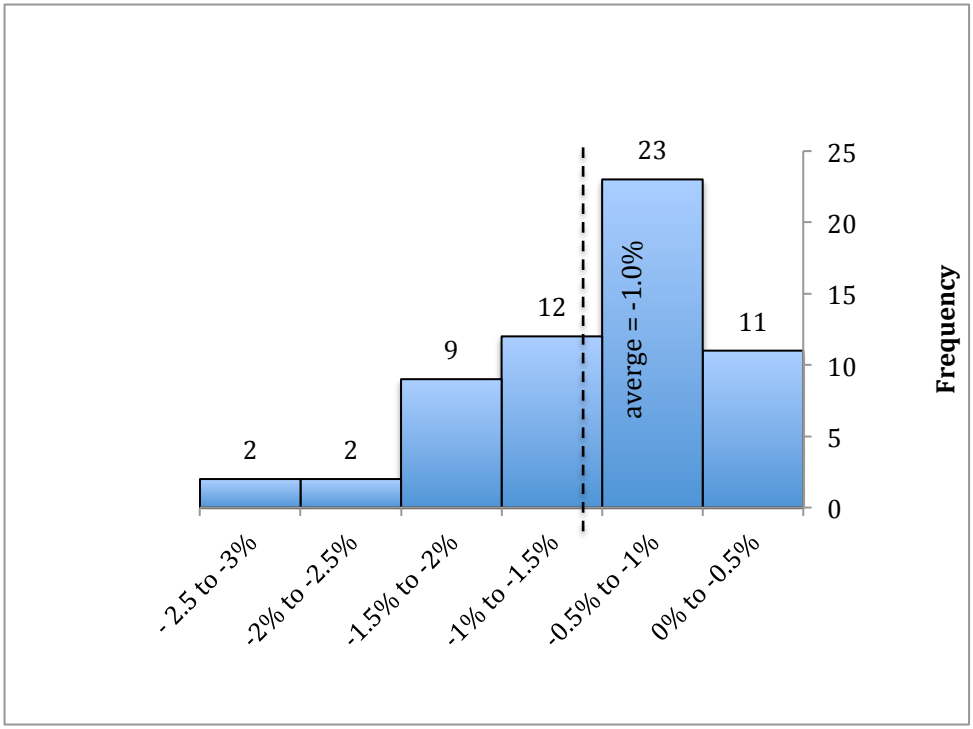

Figure 6.17: Resulting propagated error (relative change) of a +5% Gd concentration in the initial elemental composition.

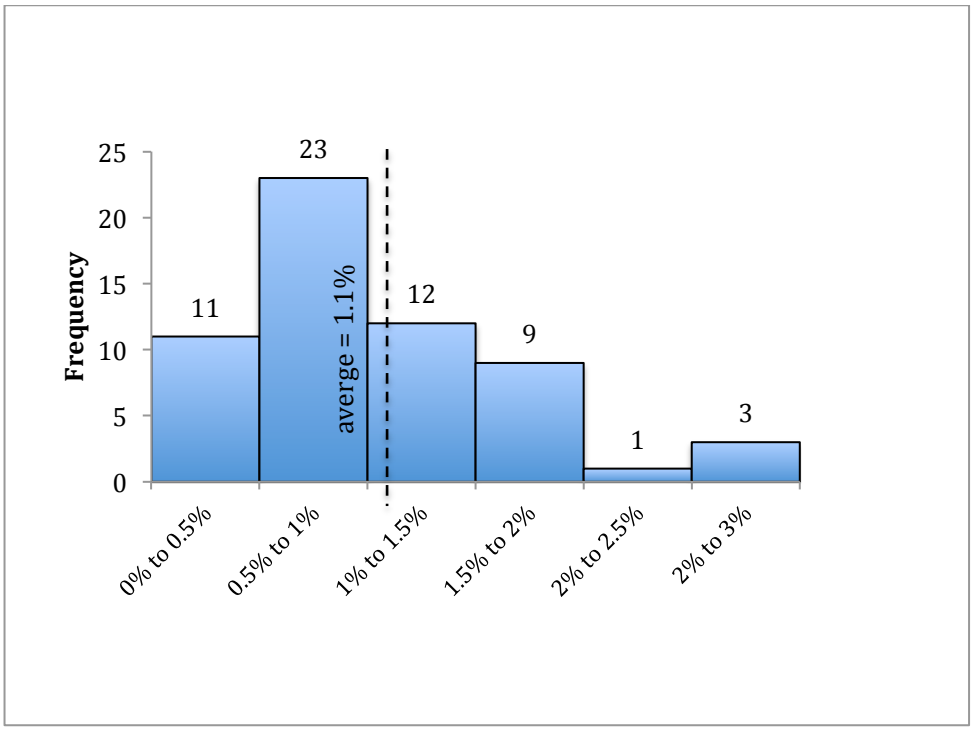

Figure 6.18: : Resulting propagated error (relative change) of a -5% Gd concentration in the initial elemental composition.

By introducing this 5% error in the Gd concentration, we observe in Figure 6.16 that there is a moderate deviation with respect to the initial values, the resulting offset values changing by less than ±3% as seen in Figures 6.17 and 6.18 with an average error of ~1.1%.

6.4.4 5% error in the U concentration

To test the impact of a 5% error in U concentration on the resulting ^{236}U concentration, the model is run three times as illustrated in Figure 6.19. First with the concentration of U analysed at the SRC, second by adding a 5% error the value from SRC and third by subtracting a 5% error the value from SRC.

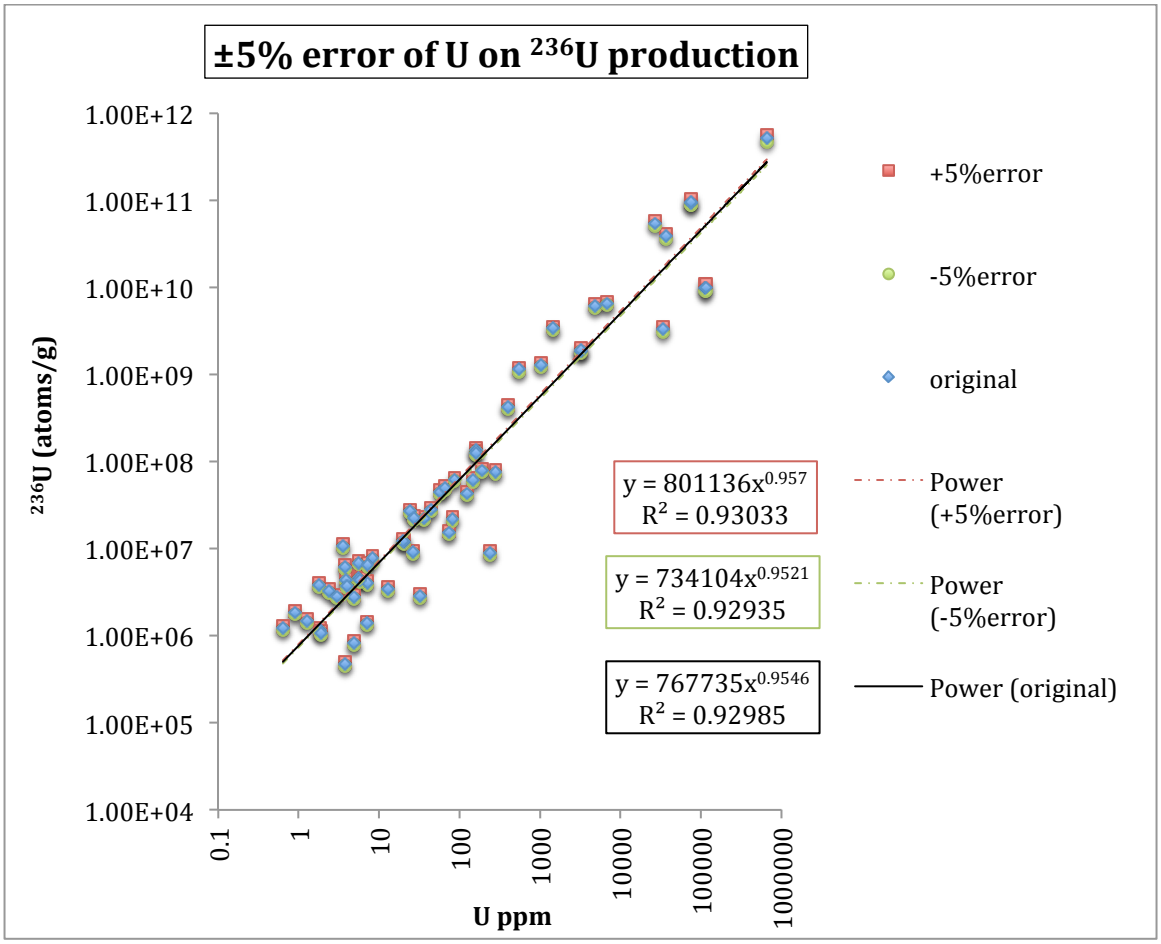

Figure 6.19: ±5% error in U concentration introduced to the calculation of ^{236}U production

When comparing the relative change (%) between the concentration of ^{236}U obtained with the error and actual measurement, it can be observed that the absolute relative change (%) varies of up to a maximum 9.29%, as illustrated in Figure 6.20 and 6.21, with averages of 5.43% to -5.47% relative change. Note that contrary to the relative change due to errors in B, Sm and Gd, U has a positive relative change when the 5% error is added and a negative relative change when the 5% error is subtracted.

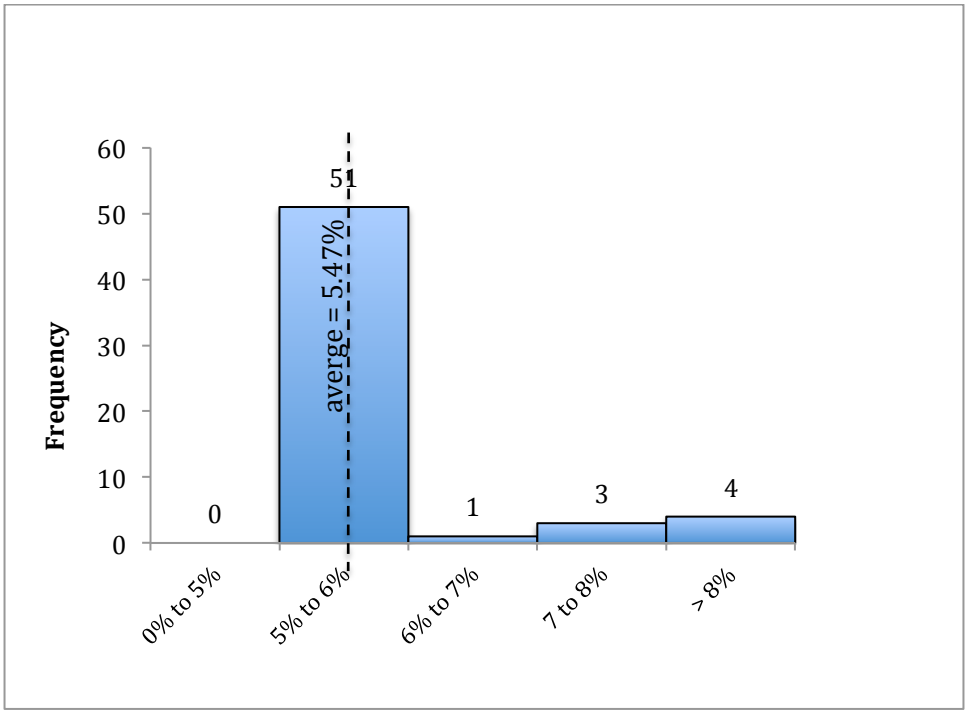

Figure 6.20: Resulting propagated error (relative change) of a +5% U concentration in the initial elemental composition.

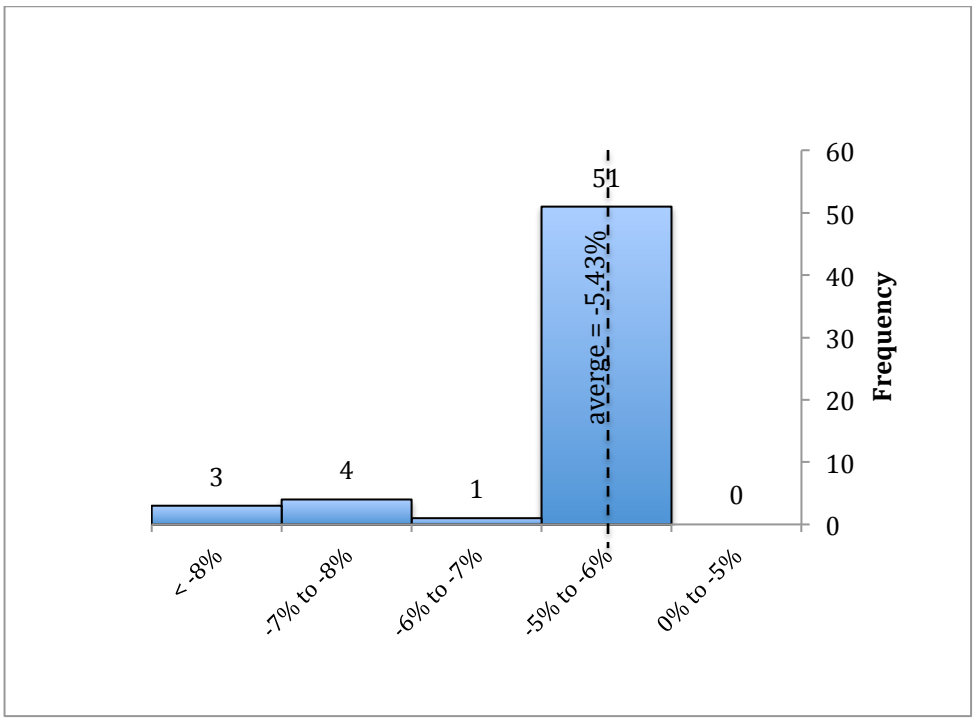

Figure 6.21 : Resulting propagated error (relative change) of a -5% U concentration in the initial elemental composition.

By introducing this 5% error in the U concentration, we observe in Figure 6.16 that there is a moderate deviation with respect to the initial values; the resulting offset values changing by less than ±10% as seen in Figures 6.17 and 6.18 with an average error of ~5.45%.

In conclusion, even if a 5% error is introduced to one of the key input elemental concentrations, the model responds by introducing very little error with a moderate propagating error only for the U and B while Sm and Gd do not propagate the error. Most important, the error is not amplified by the model.

6.5 Conclusions regarding the model

Based on the elemental analyses of the Cigar Lake samples and the correlation between U and the main neutron absorbers B, Sm, Gd as well as the error sensitivity simulated on the prediction model, we can conclude that:

1. The concentrations of U, B, Sm and Gd have a log-normal distribution in the samples of Cigar Lake.
2. Boron is present in higher concentrations than Sm and Gd around and in the ore deposit.
3. The neutron absorbing isotopes have natural abundances of 19.8% ^{10}B, 13.9% ^{149}Sm, 14.8% ^{155}Gd and 15.7% ^{157}Gd.
4. Statistically speaking, with a multiple linear regression of B, Sm and Gd simultaneously on U, Gd is the only element that is significantly correlated to U at a 95% confidence level. The same result is obtained

with the neutron absorbing isotopes and when doing multiple linear regressions on paired neutron absorbers (B, Sm), (B, Gd) and (Sm, Gd) with U.

5. The concentration of ^{236}U increases at a slightly slower rate than the increase in U concentration.

6. When comparing the $^{236}U/^{238}U$ atom/atom ratio to the neutron absorbing isotopes ^{10}B, ^{149}Sm, $^{155}Gd + ^{157}Gd$; ^{10}B has the strongest relative correlation with the ratio, but statistically speaking, all three absorbers have a significant correlation at 95% confidence level.

7. When a 5% concentration error is simulated in the system, the model responds by propagating a moderate error only from the U and B elemental concentrations while the changes in the concentrations of Sm and Gd do not propagate the error. The maximum error propagation is limited, that is, the error is not amplified.

8. The error test shows that the ^{236}U concentration decreases if the concentration of B, Sm and Gd is increased. This is expected since B, Sm and Gd are important neutron absorbers and the model reflects this fact. On the other hand, the concentration ^{236}U increases if the concentration of U increases. This is expected since more U produces more neutrons but also since ^{235}U is a neutron absorber and the model reflects that point.

7 Results of AMS Measurements

The results from the AMS measurements explained in Chapter 4 have been summarized in this section. Due to low counts on some of the samples, only 26 samples out of the 60 original samples were usable. These 26 samples had greater than 100 counts of ^{236}U. Thus this approach eliminated the samples that would induce very high uncertainties. For each sample, the atoms/g of ^{236}U and atoms/g of ^{238}U, pg/kg of ^{236}U and $^{236}U/^{238}U$ atom ratio have been tabulated. The complete table of the results presented in this section can be found in the Table B-3 in annex B. It is important to note that the denomination "ore" represents samples taken from the main mineralization and that the samples are organized based on the U (ppm) content measured at the Saskatchewan Research Center (SRC): "Ore" samples have more then 200 ppm U content, "alteration" samples have between 10 to 200ppm of U and "background" samples have a concentration of less then 10ppm U.

The $^{236}U/^{238}U$ atom-to-atom ratio is directly measured via AMS but in the samples where ^{238}U couldn't be measured via AMS, the $^{236}U/^{238}U$ atom-to-atom ratio was calculated using the number of ^{236}U atoms/g measured via AMS and the concentration of U measured at SRC. This second technique is used because in the first measurements done on the AMS, we tried to measure all trace isotopes (^{236}U, ^{234}U and ^{233}U) with the ionization detector and ^{234}U was used as an analogue of ^{238}U, as it has a natural abundance of 0.0054%. Unfortunately the beam was too intense, saturated the detector and no measurement of ^{234}U could be recorded. ^{236}U was calculated related to the amount

of ^{233}U tracer added to each sample. In this case, when we talk about the ^{238}U atoms/g, this is the measurement done at SRC.

This section will show the range of the ^{236}U results and compare it to other measurements that were found in literature and then look at the results based on an atom/g to atom/g ratio of ^{236}U and ^{238}U.

7.1 Range of the results

Figure 7.1 presented below illustrates the distribution range of $^{236}U/^{238}U$ atom ratio values in the samples. Out of the 26 samples that were analyzed, the lowest ratio measured was of 5.8 x 10^{-12} and the highest ratio of 6.7 x 10^{-08}. Most of the samples had a ratio between 10^{-10} to 10^{-11}. Note that the ratio has a log-normal distribution, just as U, B, Sm and Gd discussed in the previous chapter.

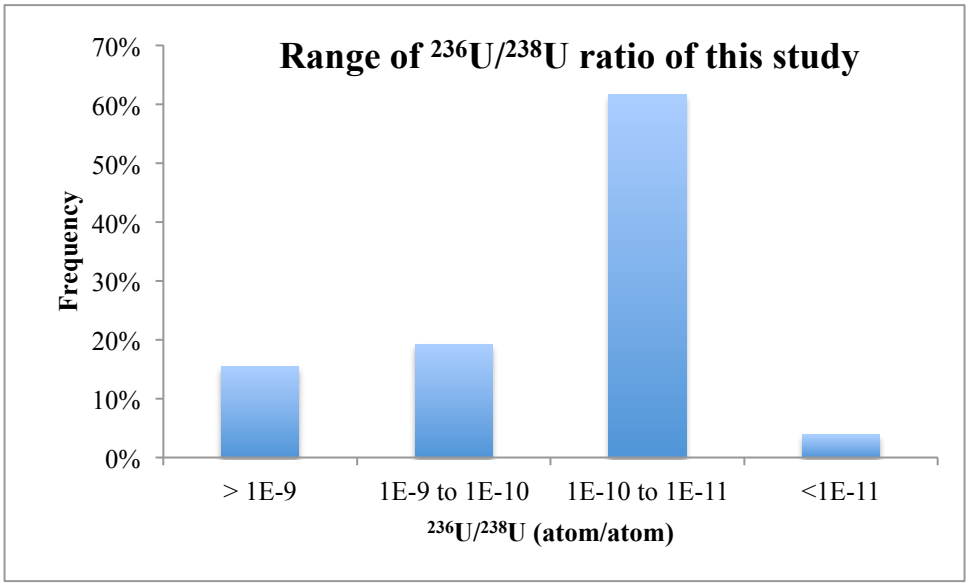

Figure 7.1 : Range and distribution of the $^{236}U/^{238}U$ atom ratios for the samples.

7.2 Comparison to other measurements

When compared to the ^{236}U measurements of previously ore samples found in literature, the same trends of distribution can be observed (Figure 7.2). A table of the published values can be found in Table A-1 in Annex A. Notice that the published values of $^{236}U/^{238}U$ used in this comparison originated from uranium ore deposits: 20 published values, varying in concentration from 1% to 74.5% U content, with the exception of one sample with concentration of 85ppm.

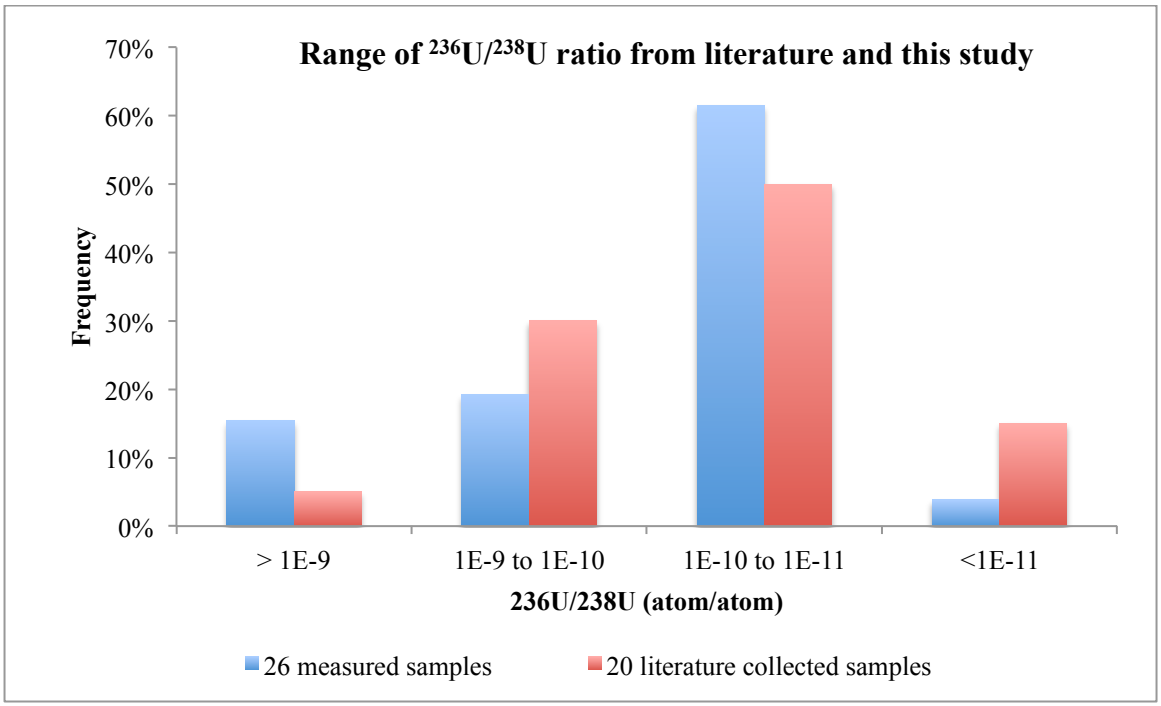

Figure 7.2 : Comparison in distribution between the 26 AMS measured samples and 20 measurements done in previous studies on uranium ore samples.

Figure 7.3 illustrates the range of both sets of values. The published values have the lowest $^{236}U/^{238}U$ atom-to-atom ratio measured of 1.03×10^{-12} and the highest ratio of 9.50×10^{-9}. Figure 7.3 shows that both data sets have the same range. Hence, in terms of the

range of values found in a uranium deposit, the AMS measurement results of this study are in agreement with the published values from previously tested samples.

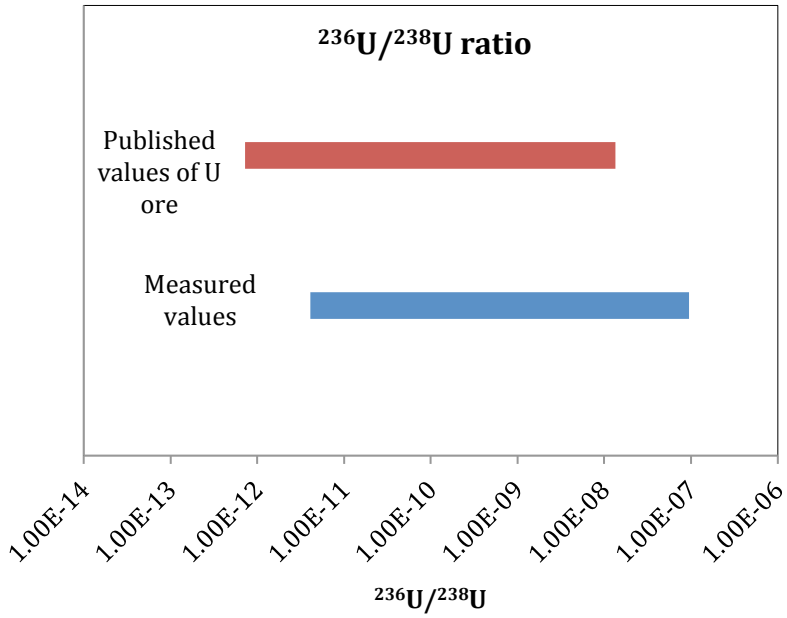

Figure 7.3: Comparison of the range of $^{236}U/^{238}U$ atom-to-atom ratio of the measured values of this study and published measurements

7.3 The AMS results

The 26 samples are presented in Figure 7.4 in terms of number of atoms/g of ^{236}U measured by AMS versus number of ^{238}U atoms/g measured at SRC. Note that both axes are expressed on the logarithmic scale and that the linear relationship in Figure 7.4 is between the logarithmic values of ^{236}U and ^{238}U. This is due to the fact that both isotopes have a log-normal distribution. The logarithmic relationship expresses the percent change of ^{236}U (atoms/g) to percent change of ^{238}U (atoms/g). This relation can be also expressed as: $\%\Delta^{236}U = 0.75 * \%\Delta^{238}U$, as it is in Figure 7.4 where $\%\Delta^{236}U$ and $\%\Delta^{238}U$ are the percent change in ^{236}U (atoms/g) and the percent change in ^{238}U (atoms/g) respectively

and 0.75 is the slope of the graph is Figure 7.4. The slope of 0.75 shows that even though both isotopes increase with grade, ^{236}U increases at a slower rate than ^{238}U.

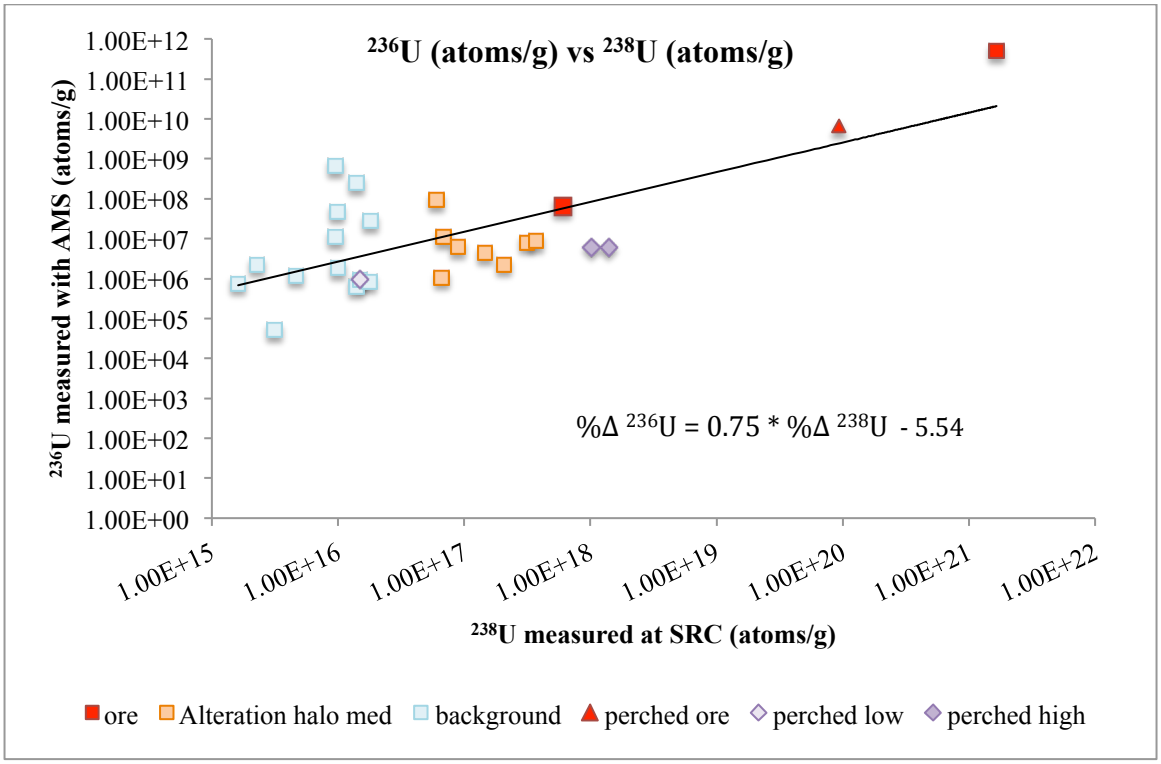

Figure 7.4: Concentration of ^{236}U (atoms/g) measured with the AMS vs the concentration of ^{238}U (atoms/g) measured at SRC. Note that the ^{236}U is calculated based on the $^{236}U/^{238}U$ measured with the AMS and the concentration of ^{238}U (atoms/g) measured at SRC. Both concentrations are expressed on the logarithmic scale and the linear relation is done on the log values of the concentration because they are normally distributed on the log scale as explained in Chapter 6.

Looking at the ore samples, notice that even though all three red samples in Figure 7.4 are from the ore, (ie the zone of mineralization), they vary in U content from 240ppm to 66.2%. This variability shows the heterogeneity of the mineralization, as the 66.2% and the 240ppm samples originated from the same core, from the main mineralization and are only ~1.4m apart.

The samples show that there is a distinctive increase in the amount of ^{236}U in the high concentration ore samples with the lowest value found in the two samples being at 6.6 x 10^9 atoms/g.

In the background and alteration halo samples, the ^{236}U concentration cannot be distinguished between the two populations, meaning that the range of ^{236}U (atoms/g) in background and alteration samples is the same and that within those ranges there is high variability. Alteration samples, as mentioned above, vary in U concentration from 10 to 200ppm and have a range of ^{236}U of ~$2*10^6$ to ~$9*10^7$(atoms/g). Background samples have a U concentration of less than 10ppm and have a range of ^{236}U of ~$6*10^5$ to $5*10^7$(atoms/g). The highest value of ^{236}U is 6.4 x 10^8 atoms/g measured in background sample CL-M-12, and this sample has a low concentration of 3.81ppm of U.

Comparing the distribution of the $^{236}U/^{238}U$ atom-to-atom ratio in Figure 7.5, it can be observed that the $^{236}U/^{238}U$ ratio does not increase or decrease with grade but varies between the samples within the same grade. Note that in Figure 7.5, the samples are ordered based on U concentration with the lowest concentration of U in sample CL-M-58 (0.64ppm) to the highest concentration of U in sample CL-M-40 (66.2%).

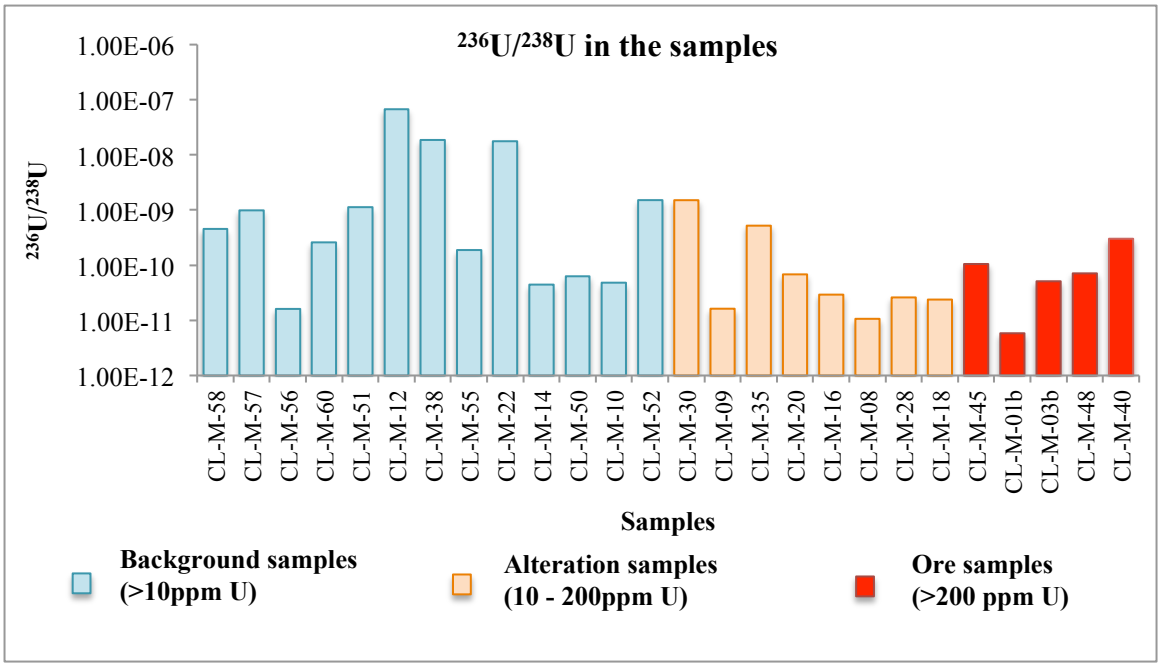

Figure 7.5: $^{236}U/^{238}U$ atom-to-atom ratio in the samples measured by AMS. Samples are ordered based on U concentration: Lowest concentration of U (CL-M-58 (0.64ppm)) to highest concentration of U (CL-M-40 (66.2%)). Note the logarithmic scale.

7.4 Conclusions from the AMS measurements

In conclusion, we can summarize our AMS results as follows:

1. Our samples have a range of $^{236}U/^{238}U$ atom-to-atom ratio varying from lowest 5.8×10^{-12} to highest of 6.7×10^{-8}. These results agree with the range of values of the $^{236}U/^{238}U$ atom-to-atom ratio measured in ore that are reported in previous publications.
2. Because ^{236}U and ^{236}U have a log-normal distribution, the linear regression done on their logarithmic values gives the expression $log(^{236}U) = -5.53716 + 0.74722 * log(^{238}U)$. This linear relationship represents the percent change of ^{236}U (atoms/g) to the percent change in ^{238}U (atoms/g).

3. Ore samples have the highest ^{236}U (atoms/g); alteration and background samples have almost the same range of ^{236}U (atoms/g) and cannot be distinguished by the amount of ^{236}U alone.
4. The $^{236}U/^{238}U$ atom-to-atom ratio does not increase with grade, but varies significantly from sample to sample within one grade.

8 Discussion

This chapter will discuss the results that were obtained with the prediction model developed as part of this study, described in Chapter 3 and 6 and the AMS measurements presented in Chapter 7. The two methods will be compared, pointing out the similarities and differences in results, and examining the possible reasons of divergence. The relevance of both measured and predicted results will be examined and compared to published results. This chapter will also examine the relation between the geology of the deposit and the $^{236}U/^{238}U$ ratio. Finally, improvements that can be brought to the prediction model and the AMS measurements will be assessed and discussed. To systematize all the ideas mentioned above, a number of questions will be approached and answered.

8.1 Results of AMS measurements versus the prediction model

Table 8-1 depicts the results presented in Chapter 6 obtained from the prediction model and the AMS measurements presented in Chapter 7 following the procedure and method described in Chapter 3 and 4. The discussion that follows will be based on these results.

		AMS results						Model results		
Grade	Sample ID	^{236}U atoms/g	error atoms/g	$^{236}U/^{238}U$ atom/atom	error atom/atom	^{236}U (pg/kg)	error (pg/kg)	^{236}U atoms/g	$^{236}U/^{238}U$ atom/atom	^{236}U (pg/kg)
Low Grade (<10ppm)	CL-M-58	7.68E+05	3.16E+04	1.76E-11	2.20E-11	0.30	0.01	1.23E+06	7.65E-10	0.48
	CL-M-57	2.25E+06	8.92E+04	3.66E-11	4.34E-11	0.88	0.03	1.86E+06	8.21E-10	0.73
	CL-M-56	5.04E+04	1.90E+03	1.61E-11	6.59E-13	0.02	0.001	1.49E+06	4.76E-10	0.59
	CL-M-60	1.18E+06	1.10E+05	2.57E-10	2.39E-11	0.46	0.04	1.16E+06	2.51E-10	0.46
	CL-M-51	1.07E+07	1.03E+06	5.25E-11	1.08E-10	4.18	0.40	6.16E+06	6.48E-10	2.41
	CL-M-12	6.39E+08	6.83E+07	6.68E-08	6.79E-09	250.36	26.77	4.80E+05	5.01E-11	0.19
	CL-M-38	4.77E+07	2.55E+07	4.82E-09	2.48E-09	18.68	9.98	4.39E+06	4.44E-10	1.72
	CL-M-55	1.85E+06	7.33E+04	4.16E-11	7.37E-12	0.73	0.03	3.71E+06	3.71E-10	1.46
	CL-M-22	2.49E+08	3.89E+07	1.79E-08	2.72E-09	97.75	15.23	4.64E+06	3.33E-10	1.82
	CL-M-14	6.23E+05	2.06E+04	4.43E-11	1.47E-12	0.24	0.01	6.92E+06	4.92E-10	2.71
	CL-M-50	9.43E+05	2.42E+05	6.35E-11	1.61E-11	0.37	0.09	4.41E+06	2.97E-10	1.73
	CL-M-10	8.42E+05	8.24E+04	4.76E-11	4.66E-12	0.33	0.03	1.40E+06	7.92E-11	0.55
	CL-M-52	2.76E+07	1.83E+06	1.35E-10	1.01E-10	10.82	0.72	6.51E+06	3.59E-10	2.55
Medium Grade (10ppm to 200ppm)	CL-M-30	9.04E+07	1.51E+06	1.51E-09	2.38E-11	35.44	0.59	2.71E+07	4.51E-10	10.61
	CL-M-09	1.08E+06	9.71E+04	1.62E-11	1.46E-12	0.42	0.04	9.12E+06	1.38E-10	3.57
	CL-M-35	1.09E+07	1.54E+06	1.59E-10	2.22E-11	4.26	0.60	2.26E+07	3.30E-10	8.84
	CL-M-20	6.12E+06	3.90E+05	6.81E-11	4.34E-12	2.40	0.15	2.21E+07	2.46E-10	8.68
	CL-M-16	4.29E+06	2.33E+05	2.92E-11	1.59E-12	1.68	0.09	4.46E+07	3.04E-10	17.49
	CL-M-08	2.18E+06	1.89E+05	1.06E-11	8.96E-13	0.85	0.07	2.19E+07	1.07E-10	8.57
	CL-M-28	8.16E+06	6.37E+05	2.60E-11	2.02E-12	3.20	0.25	4.28E+07	1.36E-10	16.76
	CL-M-18	8.72E+06	5.67E+05	2.38E-11	1.54E-12	3.42	0.22	6.12E+07	1.67E-10	23.97
High Grade (>200ppm)	CL-M-45	6.32E+07	4.46E+06	1.05E-10	7.38E-12	24.79	1.75	8.92E+06	1.48E-11	3.50
	CL-M-03b	5.91E+06	4.42E+06	5.83E-12	3.17E-12	2.32	1.73	4.21E+08	4.15E-10	164.96
	CL-M-01b	6.06E+06	2.80E+05	5.10E-11	2.76E-13	2.38	0.11	1.14E+09	8.17E-10	446.48
	CL-M-48	6.63E+09	9.80E+08	7.10E-11	1.05E-11	4028.32	384.09	3.88E+10	4.15E-10	15195.43
	CL-M-40	5.01E+11	1.35E+10	3.01E-10	8.10E+12	196369.39	5276.54	5.14E+11	3.09E-10	201660.78

Table 8-1: Table comparing the results from AMS measurements calculation from the prediction model. A more complete table can be found in the Annex B, Table B-4

1. **How do the results from the AMS measurements compare to the results from the prediction model?**

As mentioned in Chapter 7, due to low counts during the measurement of ^{236}U via AMS, only 26 samples out of the 60 initial samples were used. These 26 samples had greater than 100 counts of ^{236}U. Using thus this approach, we eliminated the samples that would induce very high uncertainties.

Figure 8.1 is a representation of the number of atoms/g of ^{236}U obtained via the model vs the number of atoms/g of ^{236}U measured using the AMS with the one-to-one line.

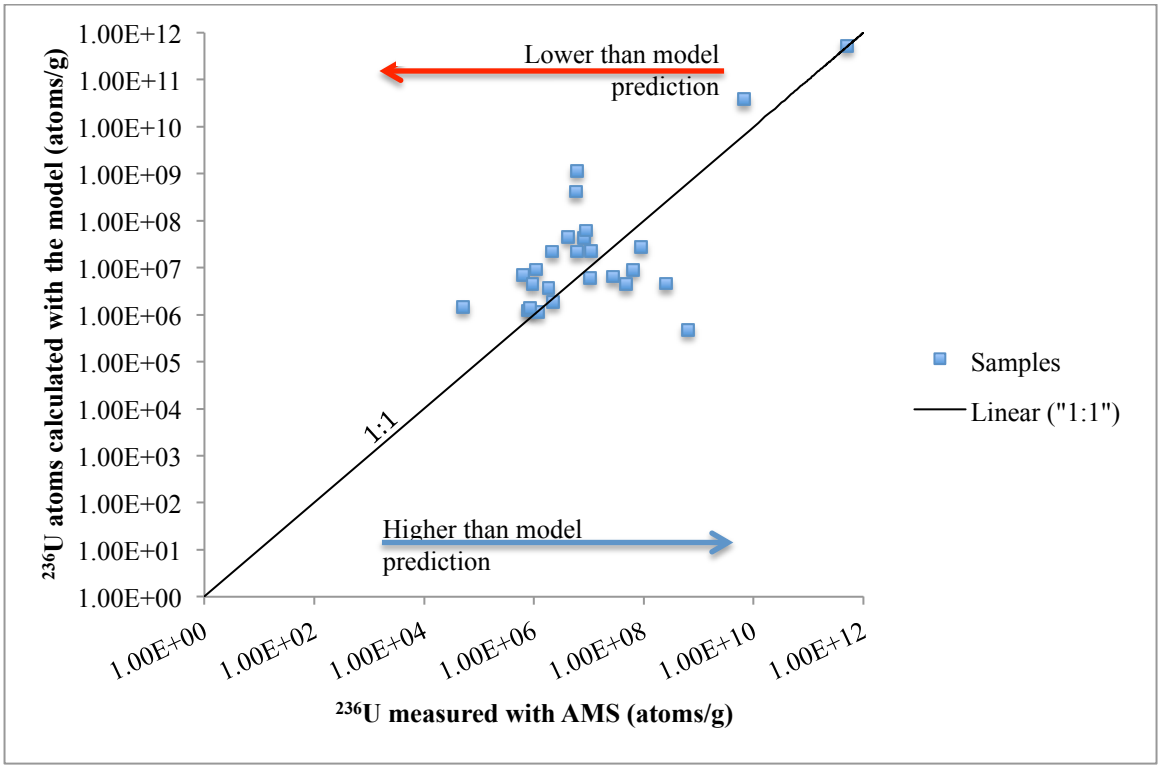

Figure 8.1: ^{236}U (atoms/g) prediction model vs AMS measurements with a one-to-one line. Note that both the concentration of ^{236}U (atoms/g) of the prediction model and the concentration of ^{236}U (atoms/g) of the AMS measurements are expressed on logarithmic scales as the values are wide-spread and that the error bars are smaller than the data symbols in this logarithmic visualization.

This comparison allows us to visually see if the prediction model and the AMS measurements are in agreement with one another. First, it can be seen that the results fall around the one-to-one line, meaning that the prediction and the measurement results agree with one another on average. 16 samples measured lower than the model predictions, 7 samples measured higher than the model and 3 samples measured close to the prediction. Statistically, with a paired t-test at a confidence level of 95%, the mean of the prediction model results compared to the mean of the AMS results show that there is no difference between the 2 populations; hence the hypothesis that there is no difference between them is accepted (this test can be found in the Annex D). Notice that the paired t-test was done on the logarithm values. This was done to eliminate skewing when the

distribution of the results is not normally distributed on a linear scale and there is a large span of values.

Figure 8.2 below, represents these same results but color-coded to the type of samples that they characterize, based on their origin and U concentration: "Ore" samples have more than 200 ppm U content, "alteration" samples have between 10 to 200ppm of U and "background" samples have a concentration of less than 10ppm U. All "perched" mineralization was collected from secondary mineralization situated in fractures above the main mineralization.

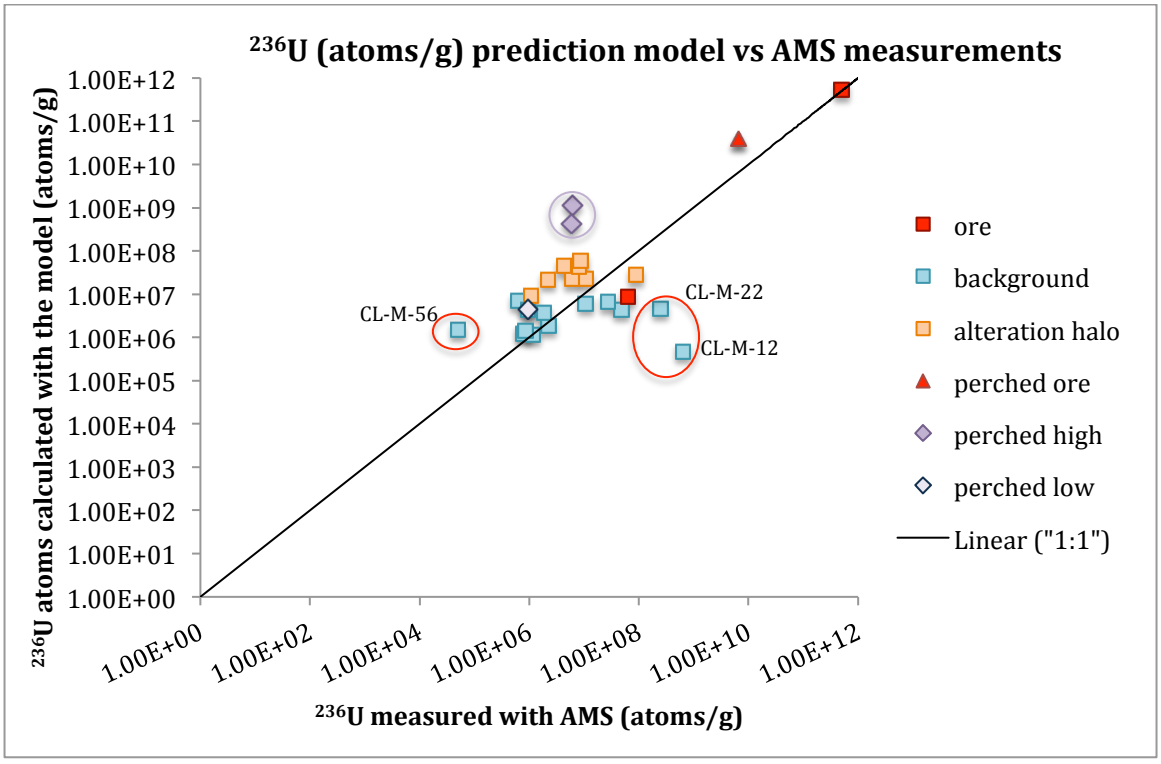

Figure 8.2 : Represents the same data as Figure 8.1, color-coded to the geology and U content of each sample. ^{236}U (atoms/g) prediction model vs AMS measurements with a one-to-one line. Note that both the concentration of ^{236}U (atoms/g) of the prediction model and the concentration of ^{236}U (atoms/g) of the AMS measurements are expressed on logarithmic scales as the values are wide-spread. The circled values represent outliners.

From Figure 8.2, we notice that five samples, encircled for clarity, are obvious outliners, meaning that the predicted result and the AMS measurement do not agree for these samples by more than a factor of 100. Two out of these five samples are collected from the vicinity of perched mineralization; these samples will be discussed when looking at the perched mineralization. The three remaining samples are background samples, with a low level of U content; these samples are named as CL-M-12, CL-M-22 AND CL-M-56 and will be referred to as sample 12, 22 and 56 from now on in this section.

Sample 56, as seen in Figure 8.2, tends to the left of the one-to-one line. This means that the measured amount of ^{236}U is lower than the predicted value. Samples 12 and 22 tend to the right of the one-to-one line implying that the measured value is greater than the predicted value.

These three background samples have been closely examined to see if they are abnormalities resulting from apparatus or processing. First, no differences with respect to the other samples during the processing have been recorded in any of the outliner samples and all samples had the same amount of tracer added. Sample 56 has an unusual high count of ^{233}U (tens of thousands of counts compared to thousands of counts in other samples) but a low count of ^{236}U. When looking at the procedure and at the results of the sample measurement, no striking anomalies were observed that would skew the data. This high result could indicate that this sample was not identified correctly or that a human mistake was made and extra tracer was added. Sample 12 shows that both ^{233}U and ^{236}U counts are unusually high compared to the other samples. This sample shows obvious extra counts for both isotopes and the reason could be cross contamination

during the measurement on the AMS machine. Sample 22 shows a slight increase in ^{233}U content compared to all the other samples, but a very high count of ^{236}U. As both 12 and 22 were part of the same set of measurements and that in general this run had very low counts, the unusual high ^{236}U in sample 22 could be due to heterogeneity within the sample and possibly a small high grade grain of uranium in the bulk rock core used for processing.

From the outliners, it can be seen that there are multiple issues that affect the ^{236}U counts and influence the results, such as heterogeneity of the sample, poisoning of the beam line in the AMS or even human error. Each sample needs to be looked individually to assess the factors that might influence the results.

When looking at the rest of the ^{236}U results, it can be noticed that:

a. The ore samples, from the main mineralization and the perched mineralization, all fall close to the one-to-one line showing a good agreement between the prediction model and the AMS measurements. These samples have the highest concentration of ^{236}U as predicted by the model and shown by the measurement with the exception of one sample, CL-M-45. This sample originated from the main ore zone, but had lower U content (~240ppm) compared to CL-M-40 (66.2% U concentration) that originated from the same mineralization and core and was only ~1.4m apart. The other ore sample CL-M-48, came from the perched mineralization with a concentration of 3.7% U. It is important to note that from

the SRC analyses of U concentration in table B-1, annex B, the heterogeneity of the main ore was visible as samples CL-M-40 and CL-M-45 have the highest and lowest concentration of U measured in the main ore.

b. The alteration halo samples plot higher in the model than the AMS measurements, with the exception of one sample, CL-M-30. The model predicts a range of ~$9*10^6$ to ~$6*10^7$, while the AMS results are ~$2*10^6$ to ~$9*10^7$.
c. Background samples plot on both sides of the one-to-one line. Excluding the outliners, the range predicted by the model is ~$1*10^6$ to ~$7*10^6$. The range measured with the AMS varies from ~$6*10^5$ to $5*10^7$.
d. For the samples collected from the perched mineralization, the model predicted higher content of ^{236}U than what was measured. The perched mineralization will be discussed in depth in a following question.

In general, the differences between the AMS measurements and the results predicted by the model can be explained by various factors:

a. *Sampling artefact*: The subsample of ore or rock that was used to measure the content of ^{236}U was not always identical to the subsample used for the U concentration measurement. In other words, it was not exactly the same sample used for both ^{236}U concentration and U concentration measurements. As mentioned in the sample preparation and processing of the model building chapter, to have a homogenized sample on a cm scale, we ground up about 500g of said core into sand. Two subsamples were taken from this well mixed sand. One was sent to SRC for elemental analyses including U, B, Sm and Gd

concentrations and the other subsample was processed to extract the U content and press it into targets for the AMS analyses. However, for the high-grade samples collected at Cigar Lake, a different method was used and each rock sample was split into two subsamples. One half of each sample was processed by the Cigar Lake team, homogenized on a large scale and sent to SRC. For the other half of the sample, less than 5 g of it was ground and used for the U extraction and AMS measurement. Consequently, in some cases, the AMS measured subsamples did not necessarily have the same concentrations of U as the subsamples analysed at SRC and used in the prediction model. This difference could have occurred due to the heterogeneity of distribution of elements in the ore and rock. If the concentration of U in the subsample that was measured with the AMS was higher than what was input in the prediction model, the prediction model would indicate a lower concentrations of ^{236}U than what was measured. On the other hand, if the concentration of U in the subsample that was measured with the AMS was lower than what was inputted in the prediction model, the prediction model will show higher concentrations of ^{236}U than what was measured.

b. *Calculation of the neutron flux in the prediction model*: In our project, we have used the neutron production based on the relationship between U and neutron production that (Fabryka-Martin et al., 1994) had found. This relationship, with correlation coefficient of 0.991, was established using nine samples of holes 220 and CS235L and a neutron coincidence counter at Los Alamos National

Laboratory. The methodology of the analyses is not available and on further investigation, it is unknown if both fission and (α,n) reactions were taken into account. Further more, this relationship was established for bulk average ore; this relationship might not apply to non-ore, closer to the surface samples.

When calculating the neutron flux, we assume that the neutron absorbers, α-emitters and α-neutron targets are homogenously distributed in the rock. In reality, as mentioned before, the rock is very heterogeneous. α-particles have a short range of only a few tens of microns and neutron yields from the alpha, neutron reactions are sensitive to the micro-distribution of elements. Therefore, neutron yields, the number of neutron produced, might depend more on the micro-local elemental composition than the bulk composition. The same idea can be applied to the neutron absorbers. Neutrons have a range of 0.5m in rock to less than 10cm in ore. We assume that the absorbers are also homogenously distributed in the rock but the deposit is very heterogeneous even on the cm scale and the micro-distribution of elements is important for the calculation of the flux. This implies that the neutron flux might be over-estimated or under-estimated depending on the micro-distribution of the elements within the sample. If the relationship found by Fabryka-Martin does not include neutron production also originating from (α,n) reactions, the neutron production rate might be underestimated. Predicting the history of a neutron is complex as it can undergo different interactions and as the elemental composition changes frequently along the neutrons path.

c. *Presence of a subset of elements that were not taken into account in the prediction model*: A subset of elements was used for the prediction of ^{236}U: (B, Sm, Gd and U). These elements, considered as the main neutron absorbers in the system were selected based on their higher neutron cross-section (their higher probability to absorb neutrons) as well as their overall concentration in the deposit. This allowed a first order estimation of where the neutrons were going and of the concentration of ^{236}U present in the bulk samples. When constructing the prediction model, we took into account the tests on the bulk composition of samples CS235L (done by Fabryka-Martin et al., (1994)), which revealed that the sum of cross-sections of these elements (U, B, Sm, Gd) would equal 95% of the total absorption cross-section. But, it is important to note that the presence of other elements such as Cl, Fe, As and water content could also impact the calculation, even if not by much. The presence of water can affect the thermalization of the neutrons and even the neutron absorption, as H is a high neutron absorber. Cl, Fe and As have smaller neutron absorption cross-section, but could be potentially important locally in terms of concentration. The elements mentioned above (Cl, Fe, As, H) were not taken into consideration in this study due to the difficulty of measurement and the complexity of estimation. Future studies of the formation of ^{236}U should examine the impact of these absorbers and attempt to include them for a more accurate result.

In conclusion, on average, the prediction model and the measurements agree statistically. However there are also some significant differences between the measurements and the model predictions. The differences can be explained by the restrictions we have put on the model (homogeneous, closed system, etc.) that in nature do not occur and by the fact that some other absorbers such as water, Cl, As and Fe were not taken into account in the model.

2. **What is the distribution of the main neutron absorbers U, B, Sm and Gd at Cigar Lake**

To visualize the distribution of the main neutron absorbers U, B, Sm and Gd at Cigar Lake, two depth profiles of their concentration were made. The profiles are shown in Figure 8.3 and 8.4.

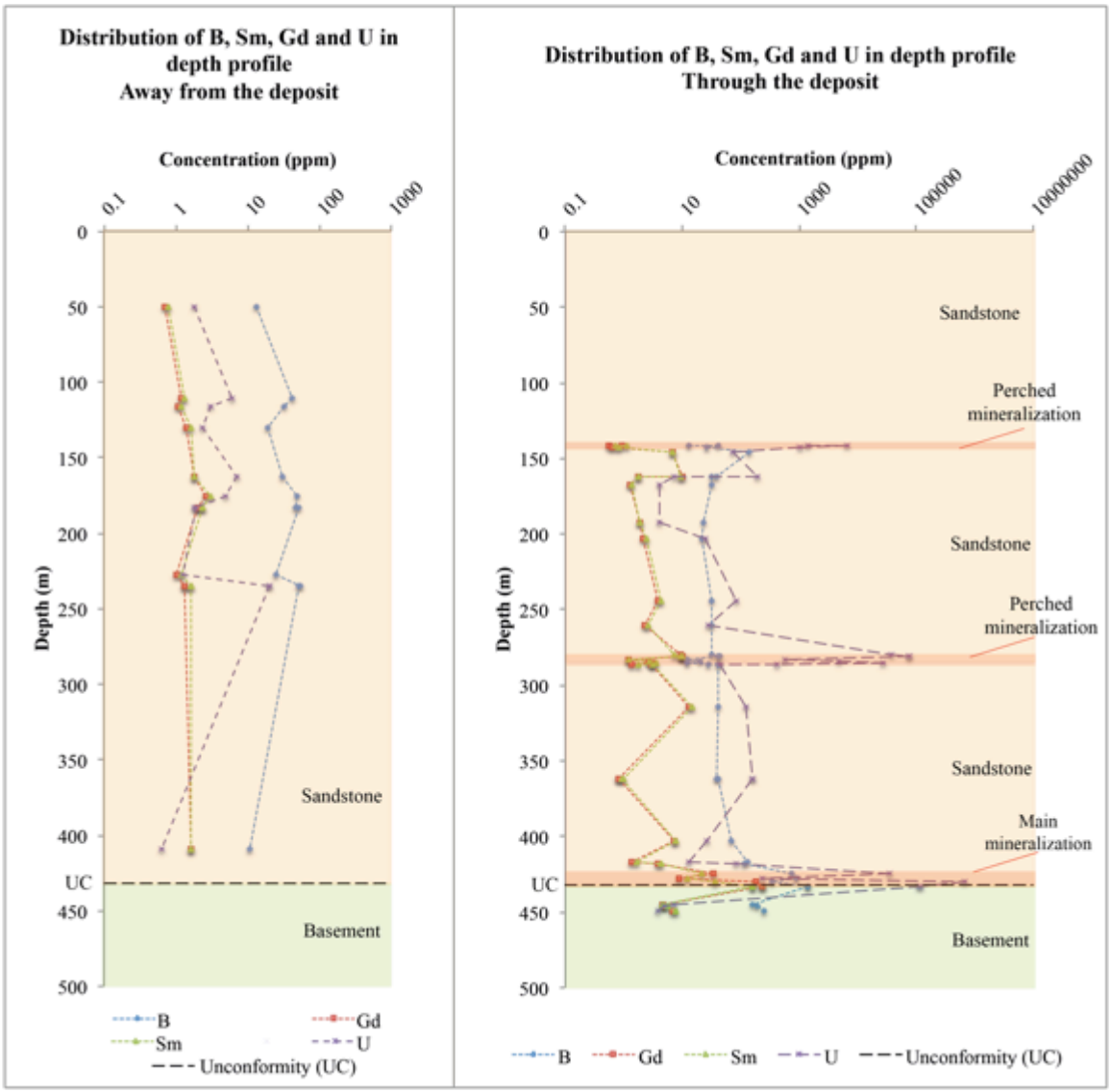

Figure 8.3 (left) and Figure 8.4(right): Profile of the concentration in ppm of U, B, Sm and Gd through non-mineralized sandstone away from known mineralization (Figure 8.3) and through mineralized ore (Figure 8.4). Note the logarithmic scale of concentrations.

Figure 8.3 illustrates the profile through the sandstone with no mineralization and includes all samples from cores CL 345, CL 346 and CL-07-271A, located away from the deposit. Figure 8.4 illustrates the second profile through mineralization. It includes all samples from cores CL 367, SF-747-08, SF-747-10 and SF-844-12 located above the mineralization and crossing through the mineralization. The core location is identified in

the site plan presented in Figure 5.6 from Chapter 5 and a list of the samples, including a description of each sample, the core it originated from and at which depth, can be found in Table B-1 in Annex B. The samples from core CL 353 located on the western pod were not used in these profiles as the core is located further away and interfered with the local perched mineralization observed above the eastern pod.

From Figures 8.3 and 8.4, we can observe the distribution of U, B, Sm and Gd. Note that the concentration in ppm is displayed on logarithmic scale on both figures as the concentration of all four elements varies on a large range. We can notice that:

a. The concentration of U varies throughout the profile at a small scale in Figure 8.3 and more drastically in Figure 8.4. In typical sandstone of the Athabasca basin with no mineralization shown in Figure 8.3, U concentration varies between < 1 and 10 ppm. In a mineralized profile as shown in Figure 8.4, U is of course high in the mineralization zone, whether main or perched, but also varies between 1 and 100ppm in the alteration zone above the deposit. Please note the mineralization sections of Figure 8.4, are delimited by the information found in the Cigar Lake core logs and pictures of each core. The variation in U concentration inside these sections shows the heterogeneity of the U distribution inside the ore. Note that in perched mineralization, the U concentrations vary from hundreds of ppm to thousands of ppm and that in the main ore U concentrations vary from thousand of ppm to tens of thousands of ppm.

b. Sm and Gd vary together and have almost the same concentration. Their concentrations vary between .5 to ~10ppm, and is higher around mineralization. In Figure 8.3, the concentration of Sm and Gd remain around 1ppm and varies minimally compared to the concentrations in the mineralized profile. The origin of the Sm and Gd was tested to verify if it was part of decay or had a different origin. Less than 1% of the Sm and Gd originated from U decay.

c. In the mineralized profile, B remains almost constant at about 50ppm in the altered sandstone. In perched mineralization, B reacts in two opposite ways: It increases to about 100ppm at the perched mineralization close to the surface but decreases to about 10ppm in the perched mineralization at depth ~280m. B increases drastically to ~1000ppm close and through the high mineralization as seen in Figure 8.4. In the non-mineralized profile, B remains between 1 and 50 ppm.

3. What conclusion can we make about the prediction model?

Since the prediction model and the AMS measurements agree on average on the concentration of ^{236}U in the samples, the model simulates the basic mechanism of the ^{236}U formation. This means that our model can predict a range of ^{236}U (atoms/g) for a sample at Cigar Lake based on its concentration of U, B Sm and Gd. Because of the heterogeneity of the ore body and its surroundings, a descriptive log of the samples and their emplacement in the ore body is required to fully interpret the model results. For

example a sample from within the ore body but with a much lower U content than the average for the high grade ore is predicted to have a low ^{236}U concentration.

As discussed in Chapter 6, the sensitivity of the model to variations in the elemental composition was tested by simulating a 5% change in the elemental composition of U, B, Sm and Gd. The test demonstrated that the error propagated to the calculated ^{236}U concentration was smaller than the error introduced in the elemental concentration with the exception of B and U. A 5% bias in the concentrations of either of these two elements introduced a maximum error of 5.4% and 9.3% respectively. This means that the prediction model is robust and the effect of biases in the elemental composition is limited with only a small propagation, without amplification.

Discrepancies between the model and the measured AMS results show that there are still factors that would need to be taken into account in the model for a future more accurate prediction. These include some minor neutron absorbers, the concept of closed system and the heterogeneity of the deposit. In all, despite these discrepancies, it can be considered that this simple model can be used as a first estimate of the ^{236}U content.

4. What conclusion can we make towards the AMS results?

From the AMS results presented in Chapter 7, multiple observations and conculsions can be made. Foremost, it is important to mention again that due to low current and hence high statistical error, only 26 out of the 60 original samples could be used. For this reason, the AMS results have limited the amount of samples that could be compared to the theoretical prediction model. The AMS measurement of ^{236}U is still in experimental phase at AELL. Additional work is needed to improve the radiochemical recovery of

^{236}U from large samples of rock. The errors and possible enhancements in the AMS measurement process were discussed in Chapter 4. Also, the reasons for the low counts have not yet been isolated and are still being investigated.

Figure 7.4, of the previous chapter, illustrates the relationship between ^{238}U (atoms/g) and ^{236}U (atoms/g). The AMS measurements show that:

a. High-grade ore samples have a characteristic high ^{236}U concentration. One exception was observed but note that this sample had a low U content even though it originated from the main mineralization as mentioned earlier.
b. Background and alteration halo samples measured with the AMS have similar ^{236}U concentrations and cannot be distinguished in terms of ^{236}U content. These samples range between $5*10^4$ to $1*10^8$ atoms of ^{236}U per g of rock, for a range of $1*10^{15}$ to $5*10^{17}$ atoms of ^{238}U per g of rock. In terms of concentration in ppm of U, this is equivalent to 0.64 to 146ppm respectively.

These results suggest that there is no distinction between background samples (samples far away from mineralization) and alteration halo samples (samples in the vicinity of the mineralization).

Notice in Figure 8.5 that the relationship between ^{236}U vs ^{238}U concentration in atoms/g shows a linear slope of 0.75 on the logarithmic values. As mentioned in Chapter 6, this relationship shows the percent change of ^{236}U to the percent change of ^{238}U, that can be written mathematically as : $\%\Delta^{236}U = 0.75 * \%\Delta^{238}U - 5.54$, where $\%\Delta^{236}U$ and

$\%\Delta^{238}U$ are the percent change in ^{236}U (atoms/g) (the logarithmic value of ^{236}U) and the percent change in ^{238}U (atoms/g) (the logarithmic value of ^{238}U) respectively and 0.75 is the slope of the graph in Figure 8.5. Since the slope of the regression is less than 1, this indicates that other factors are affecting the creation of ^{236}U and that although both ^{236}U and ^{238}U increase with grade, they do not increase 1:1 proportionally.

As discussed in Chapter 6, we tested the statistical relationship between the amount of U present in the samples and the neutron absorbers B, Sm and Gd. A statistical correlation was found between Gd and U. This correlation could explain why ^{236}U does not increase at the same rate as the grade of U increases, as Gd also increases with grade and hence absorbs available neutrons.

In conclusion, the method to measure and analyze ^{236}U using AMS at AELL needs improvements to allow higher currents and hence more ^{236}U counts. Consequently, fewer samples would be eliminated from the data analysis due to low counts. The possible inclusion of more samples could give a better picture of how and if the AMS measurements can be used reliably to study U deposits.

5. **Does the perched mineralization have a different signature than the main mineralization?**

In the perched mineralization zones, only four samples were considered, as all the rest of the samples gave low counts and had to be eliminated. These samples and their results are tabulated in table 8-2 below.

What we expected to see was that the ^{236}U content in perched mineralization would be lower than in the prediction model as the perched mineralization is a secondary event that happened after the main mineralization. This means that the ^{236}U, in this new closed system would start being formed later and there would be a bigger difference between the ^{238}U present and the ^{236}U present. When looking at the results, it can be observed that the ^{236}U content measured is in fact lower than the ^{236}U predicted. Unfortunately, with only four samples to evaluate and the fact that there are discrepancies expected as observed in the rest of the samples, no verdict can be made. It can only be concluded that we cannot exclude that there is a possibility that all perched mineralization could have lower ^{236}U content than the model prediction for the main mineralization.

		AMS results						Model results		
Grade	Sample ID	^{236}U atoms/g	error atoms/g	$^{236}U/^{238}U$ atom/atom	error atom/atom	^{236}U (pg/kg)	error (pg/kg)	^{236}U atoms/g	$^{236}U/^{238}U$ atom/atom	^{236}U (pg/kg)
Low Grade (<10ppm)	CL-M-50	9.43E+05	2.42E+05	6.35E-11	1.61E-11	0.37	0.09	4.41E+06	2.97E-10	1.73
High Grade (>200ppm)	CL-M-03b	5.91E+06	4.42E+06	5.83E-12	3.17E-12	2.32	1.73	4.21E+08	4.15E-10	164.96
	CL-M-01b	6.06E+06	2.80E+05	5.10E-11	2.76E-13	2.38	0.11	1.14E+09	8.17E-10	446.48
	CL-M-48	6.63E+09	9.80E+08	7.10E-11	1.05E-11	4028.32	384.09	3.88E+10	4.15E-10	15195.43

Table 2 -2: Samples originating from perched mineralization. Results of the AMS measurements and values obtained from the prediction model. A more complete table can be found in the Annex B, Table B-3

6. Where in the deposit is the ^{236}U / ^{238}U ratio highest?

The $^{236}U/^{238}U$ ratio varies widely between the different samples. Figure 7.5 of the previous chapter illustrates the $^{236}U/^{238}U$ ratio for all the samples with measurements done on the AMS.

Note that in Figure 7.5, samples are ordered based on U concentration with the lowest concentration of U in sample CL-M-58 (0.64ppm) to the highest concentration of U in sample CL-M-40 (66.2%) and that the $^{236}U/^{238}U$ ratio is expressed on logarithmic scale. The first thing that can be observed is that the $^{236}U/^{238}U$ ratio does not increase with grade

but varies throughout the samples and hence the grade. Because it does not increase or decrease with grade, the $^{236}U/^{238}U$ ratio shows the non-proportionality between ^{236}U and ^{238}U concentrations.

In summary, even though the sample with the most ^{238}U atoms/g has the most ^{236}U atoms/g as discussed in question 4, this is not reflected in the $^{236}U/^{238}U$ ratio. The $^{236}U/^{238}U$ ratio does not vary systematically between low and high-grade samples.

7. How do the values of the AMS measurements compare to published data?

As discussed in Chapter 7, the $^{236}U/^{238}U$ ratio measured by AMS in the samples, had a range of $5.8*10^{-12}$ to $6.7*10^{-8}$ (Figure 7.2). Figure 7.2 also shows that the range of our measured samples falls in the same range as the 20 samples of uranium ore collected from published studies (in red) referenced in table A-1 annex A. In these 20 samples, the lowest $^{236}U/^{238}U$ ratio measured was of $1.03*10^{-12}$ and the highest ratio of $9.50*10^{-9}$.

For a more comprehensive comparison on a larger scale, we looked at other available published values of the $^{236}U/^{238}U$ ratio. Figure 8.5 below illustrates the ranges of the $^{236}U/^{238}U$ ratio in normal crustal rock, natural waters, of anthropogenic origin, the published values of uranium ore samples, our values and the values measured from U mill extraction.

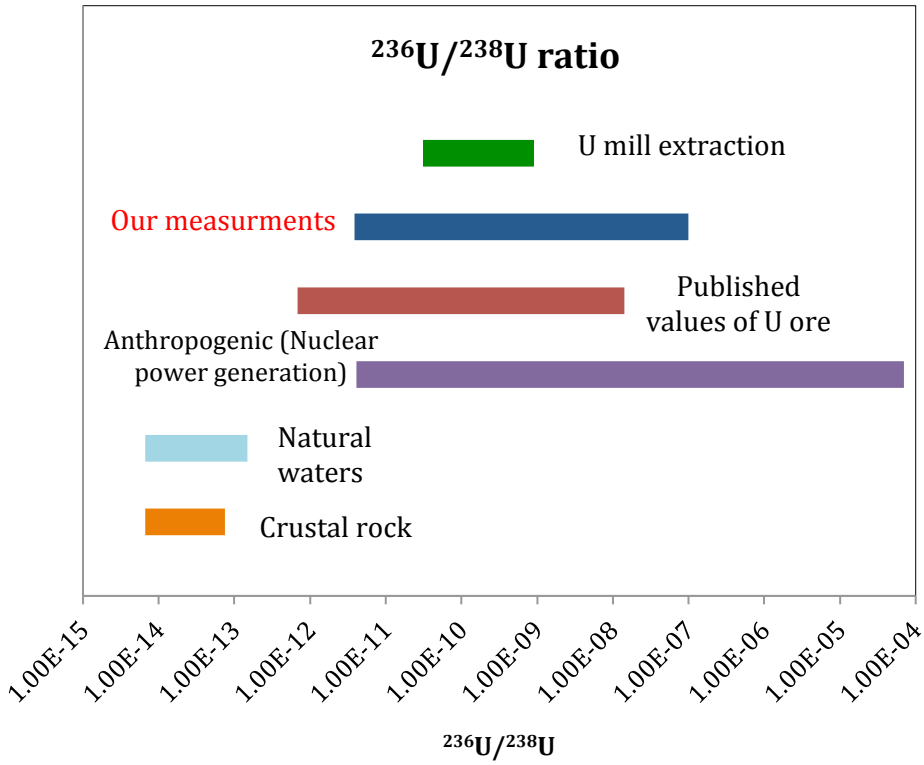

Figure 8.5: Compilation of the 236U/238U atom ratio of previously published studies and our AMS results. Note the logarithmic scale. (Berkovits et al., 2000; Hotchkis et al., 2000; Steier et al., 2008; Wilcken et al., 2007; Zhao et al., 1994)

From Figure 8.5, it is clear that our measurements of the $^{236}U/^{238}U$ atom ratio are in the same range as the comparable published values. Our measurements of the $^{236}U/^{238}U$ ratio are much higher than those of normal crustal rock. This is due to the fact that normal crustal rocks have a very low U content of about 1.8ppm (Steier et al., 2008). The values of $^{236}U/^{238}U$ atom ratio used for the compilation of Figure 8.8 and their reference can be found in table A-1 in Annex A.

Murphy et al. (2015) conducted a parallel study on $^{236}U/^{238}U$ atom ratio in U ore and concluded to a different trend then the one observed here. Their study was based on three sets of three samples from the South Australian Beverley North sandstone-hosted uranium deposits that varied in U concentration from 78.9 to 24,200 ppm. They

concluded that the $^{236}U/^{238}U$ atom ratio increased with grade. Please not that these conclusions were made based on only three samples per deposit and that there were exceptions. Even thought the trend observed and the conclusions made were not the same, the range of values obtained from the samples via AMS were similar.

We can conclude that the AMS measurement results of this study agree with other similar measurements done in previous studies of U ore samples.

8. Does ^{236}U (pg /kg rock) increase in zones with very high mineralization?

Please note that Figure 8.9 below represents the same data presented in Figure 8.5 but converted from atoms/g to pg/kg. This representation allows a better global visualization of the data as 1mg/kg=1ppm, hence 1pg/kg = $1*10^{-9}$ ppm.

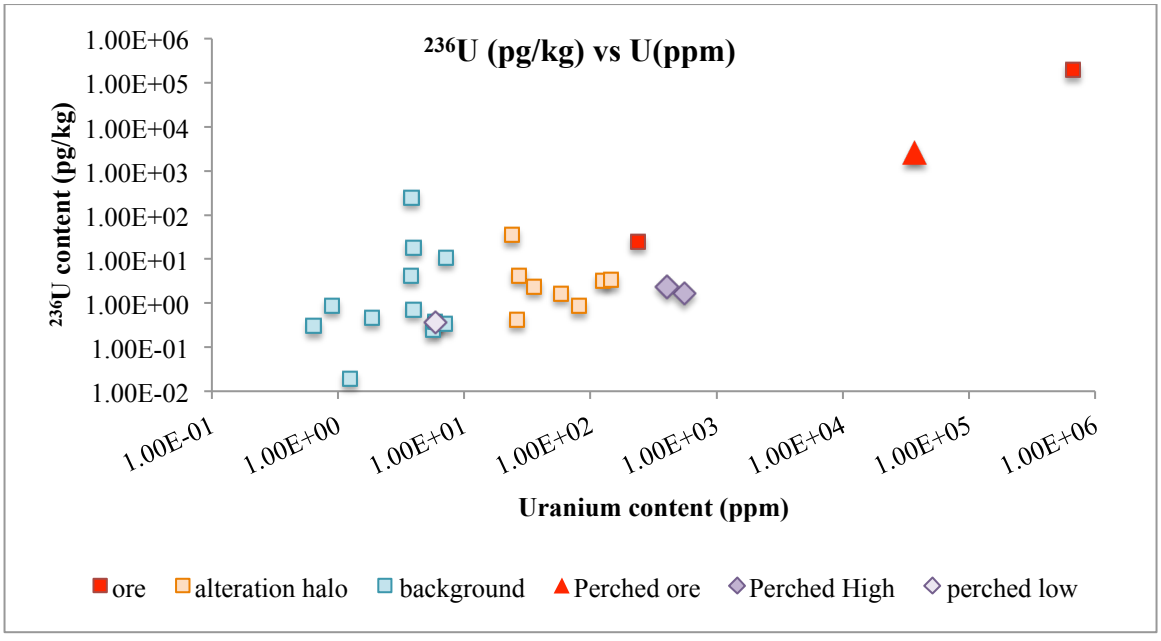

Figure 8.6: Concentration of ^{236}U (pg/kg) measured with the AMS vs the concentration of U (ppm) measured at SRC. Both concentrations are expressed on the logarithmic scale as they span on a wide range. Note that this Figure represents the same data presented in Figure 8.5 but converted from atoms/g to pg/kg.

In a very high mineralization zone, it is visible from Figure 8.9 that the amount of ^{236}U (pg/kg) increases as uranium grade increases. In a sample with ~4% ore, the content of ^{236}U is 100 times greater than in background or alteration halo samples. Our highest-grade sample of 60% uranium, recorded a ^{236}U amount of 0.2µg /kg, 10000 times the values of background or alteration halo samples. One of the samples collected from a highly mineralized zone had a low measured U content of 240 ppm. This value is similar to the amount that was also recorded in perched mineralization samples and this sample had a measured ^{236}U content (pg/kg) that is similar to background and alteration halo samples. The highest sample (66% U) and the lowest sample from the mineralization zone (240ppm U) were both collected from the same mineralization in the same core at only ~1.4m distance apart along the core. This implies that the content of ^{236}U (pg/kg) will be high in zones with the highest mineralization but that heterogeneity in the ore zone is important too and can affect the ^{236}U (pg/kg) content.

To visualize the distribution of ^{236}U at Cigar Lake, two depth profiles of ^{236}U (pg/kg) have been built using the AMS and the prediction model results. The first profile in Figure 8.10 below combines the samples located further away from the deposit from cores CL 345, CL 346 and CL-07-271A. The second profile illustrated in Figure 8.11 combines the samples located above the mineralization and crossing through the mineralization from cores CL 367, SF-747-08, SF-747-10 and SF-844-12. The core location is identified in the site plan presented in Figure 5.6 from Chapter 5 and the samples associated with them are identified in Table 8.1 at the beginning of this chapter. The four samples from core CL 353 located on the western pod were not used in these

profiles as the core is located further away and interferes with the local perched mineralization situated above the eastern pod.

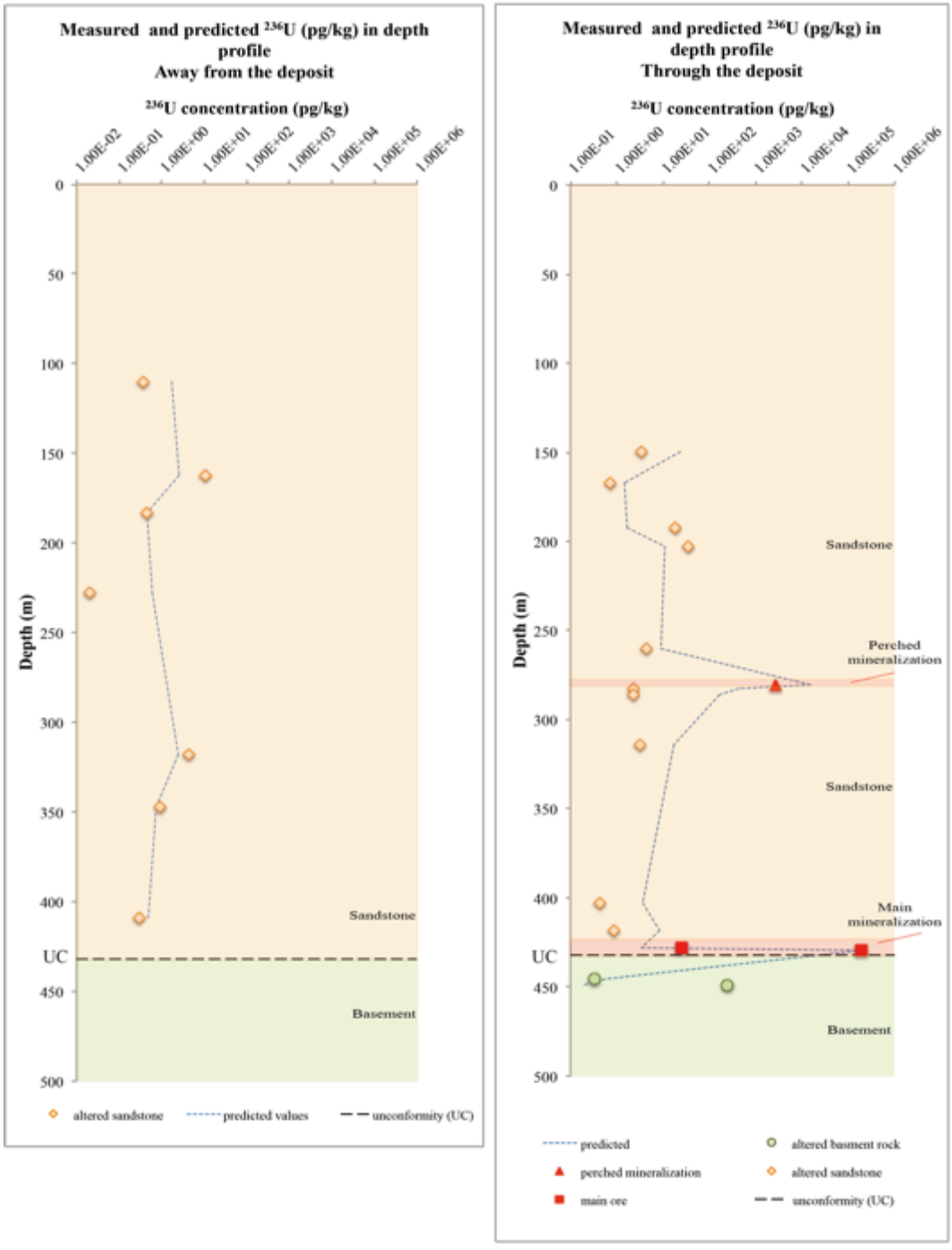

Figure 8.7 (on the left) and Figure 8.8 (on the right): Depth profile of the concentration in pg/kg of ^{236}U through non-mineralized sandstone away from known mineralization (Figure 8.10) and through mineralized ore (Figure 8.11). Note the logarithmic scale of concentrationThe ^{236}U concentration (pg/kg) of the measurements done with the AMS are illustrated as dots and the results of the prediction model are expressed as a dashed-line.

From Figures 8.10 and 8.11, we can see that:

a. The concentration of ^{236}U is low in altered sandstone away from the deposit (with concentrations of ^{236}U varying from 0.1 to 100 pg/kg) and is a little higher in altered sandstone on top of the mineralization (with concentrations of ^{236}U varying from ~ 0.5 to ~500 pg/kg).
b. The concentration of ^{236}U is high in perched mineralization, and main mineralization with concentration going up to 196369.39pg/kg which is equal to 0.196 ppb, round up to 0.2ppb.
c. By comparing Figures 8.10 and 8.11 to Figures 8.3 and 8.4, it is visible that the concentration of ^{236}U (pg/kg) has the same trend through the profile as U (ppm) does. This implies that the concentration of ^{236}U alone is not useful in the exploration of U, as its behaviour mirrors the one of U. Because the concentration of ^{236}U (pg/kg) compared to non-mineralized zones is not drastically higher in altered sandstone on top of mineralization or even in sandstone close to the mineralization, the concentration of ^{236}U by itself is unable to identify possible mineralization.

9. What are the next steps to further understand ^{236}U production in this environment?

To further understand the production of ^{236}U in an environment such as the Cigar Lake deposit, multiple refinements and further research could help clarify some of the mysteries that are still eluding us.

The prediction model can be further developed as to include other potential absorbers. The simplifications that were made can be waived so that the concepts of neutron thermalization, heterogeneity and the fact that the actual system is not an entirely closed system can be explored. The first step to further the research would be to use of a Monte-Carlo Neutron and Photon (MCNP) transport code to simulate the production rate of ^{236}U at Cigar Lake. The MCNP uses statistical techniques to predict the proportion of neutrons that will be absorbed in a given the environment. This simulation can be used to predict the range of concentration of ^{236}U.

As mentioned above, the analytical method, the AMS, was still experimental at the moment this study was conducted. Understanding the limitations of the AMS, the reason why low counts were recorded in so many samples and then fixing this issue are the next steps in the research. Future tests are needed to increase the count rate from AMS samples by testing different target materials such as the use of silicone instead of aluminum as the target-mixing agent. Studies need also to be conducted to understand the spiky backgrounds as mentioned in Chapter 4 and the drop in UF_5^- current in high-grade samples that leads to low counts. These studies are currently underway at AELL.

9 Conclusion

The objective of this research was to determine if the presence of the ^{236}U isotope in ores can be used as a reliable tracer for uranium high-grade deposits, with the hypothesis being that neutron production increases with ore grade. Thus, the production of ^{236}U, formed by neutron activation of ^{235}U, should presumably increase the $^{236}U/^{238}U$ atom ratio according to the grade of the ore.

As part of this research work, a prediction model based on the calculation of ^{236}U concentration from the physics that form this uranium isotope was developed. The in-situ ^{236}U prediction model used the elemental composition of samples from the well-studied Cigar Lake uranium deposit in northern Saskatchewan, Canada and analyzed at the Saskatchewan Research Center. The results of the model were then compared with measurements made on the same samples, but this time measured the ^{236}U concentration by accelerator mass spectrometry in the André E. Lalonde AMS Laboratory at the University of Ottawa.

The AMS successfully measured ^{236}U in the majority of samples. However, because the AMS analytical method for ^{236}U is still in the experimental stage, low source current was often encountered and as a result the measurement error in some samples was considered too large to be reliable. Nevertheless, during the course of this research the method for analyzing ^{236}U was much improved and allowed for better detection, Production of higher

source currents for U in the AMS source will be critical to improving the measurement of ^{236}U by AMS.

AMS measurements of samples from Cigar Lake showed ^{236}U concentration to vary between 0.02pg/kg and 0.2µg/kg while the $^{236}U/^{238}U$ atom ratio varies between 5.8×10^{-12} and 6.7×10^{-08}. Compared with previous studies our results exhibit a similar range of values and the $^{236}U/^{238}U$ atom ratio indicated above crustal rock values even in samples near the deposit and considered barren of U (less then 10ppm of U).

It was observed that ^{236}U concentration correlates directly with U concentration. In addition, regression analysis shows that the percent change of ^{238}U leads to a 0.72 percent (or 72%) change in ^{236}U, implying that ^{236}U increases at a slower rate than ^{238}U. As ^{236}U mimics the distribution of ^{238}U concentration, but at a much lower concentration, it was concluded that using only ^{236}U as a tracer provides no additional geospatial information on the deposit.

Significantly, the sample with the highest ^{238}U concentration had the highest ^{236}U concentration, but this is not reflected in the $^{236}U/^{238}U$ ratio. The $^{236}U/^{238}U$ ratio cannot identify or describe a low or high-grade sample as it varies significantly from sample to sample, and even in samples with the same ore grade. This, therefore, contradicts the working hypothesis of this study and also the conclusions of Murphy et al. (2015) suggesting that the $^{236}U/^{238}U$ atom ratio increases with grade. It is important to note that

in the Murphy et al. (2015) study, only nine samples were analyzed, and in which some samples measurements contradicted their own conclusions.

From the point of view of perched mineralization (i.e. secondary mineralization located in fractures above the main deposit) it was hypothesized that these samples would show lower concentrations of ^{236}U when measured with the AMS compared to the prediction model calculations. This is because secondary mineralization is younger than the main mineralization and thus ^{236}U would have had less time to accumulate. Although based on a limited number of samples, results here show that most perched mineralizing samples did in fact exhibit lower concentration of ^{236}U in AMS measurements compared to the prediction model. Unfortunately, the small number of samples coupled with the discrepancies between model and prediction model, makes any reliable conclusion questionable.

On average the ^{236}U prediction model and AMS measurements are statistically correlative. However, significant differences between AMS measurements and model predictions are noted, which most probably are the result of simplifications made in the model, including: homogeneity of the deposit, the estimation of the neutron flux and the restricted set of elements used in the calculation of ^{236}U, or even being a sample artifact. In itself, the prediction model can be considered robust since from the simulation of error introduced in the model in the elemental composition, only a small propagation of error is produced without amplification. Thus, the proposed model can provide a reasonable estimate of in-situ ^{236}U content.

Future developments for measuring ^{236}U by AMS should focus on solving the low source current issues. For prediction model, lifting some of the simplification and making the model more complex could allow a better calculation of ^{236}U and hence more precise results... In terms of using ^{236}U as a tracer in a natural U deposit, the results from this study are not encouraging, but may be better evaluated with a larger sample population for ^{236}U.

Annex A: $^{236}U/^{238}U$ found in literature

Table A - 1: Compilation of samples tested for $^{236}U/^{238}U$ in different environments.

Crustal rocks			
Sample#	**U**	**U236/U238**	**Comments**
	1.8 mg/kg	1.00E-14	calculated (cf Stier et al. 2008)
		5.00E-14	
Natural Waters			
Sample#	**U**	**U236/U238**	**Comments**
		1.00E-14	calculated (cf Stier et al. 2008)
		1.00E-13	
Anthropogenic (Nuclear power generation)			
Sample#	**U**	**U236/U238**	**Comments**
IAEA375	.002 mg	2.45E-06	soil proximal (100 km away) to Chernobyl (cf Hotchkis et al., 2000)
IAEA 135	0.004 mg	1.48E-06	Irish Sea sediment (cf Hotchkis et al., 2000); close proximity to Sellafield
IAEA 300	.015 mg	1.40E-08	Baltic Sea Sediment (cf Hotchkis et al 2000); "non-anthropogenic background"
Garigliano upstream average	2 ug/g	1.40E-09	river sediment from Garigliano river upstram from nuclear poer plant (Steir et al., 2008)
T2H	<1 ug/g	1.48E-06	1 g Salzburg soil 0.5 mm depth (Steir et al., 2008)
T2G	<1 ug/g	8.00E-07	1 g Salzburg soil 15 mm depth (Steir et al., 2008)
T2F	2 ug/g	3.90E-07	1 g Salzburg soil 25 mm depth (Steir et al., 2008)
Forstau_B	<0.001 ug/g	6.30E-08	1.5 L Salzburg rivulet water (Steir et al., 2008)
Forstau_F	<0.0011 ug/g	7.00E-08	1.5 L Salzburg rivulet water (Steir et al., 2008)
Forstau_G	<.001 ug/g	2.10E-08	1.5 L Salzburg well water (Steir et al., 2008)
Forstau_K	0.015 ug/g	4.40E-08	1.5 L Salzburg rivulet water (Steir et al., 2008)
Forstau_L	<.001 ug/g		1.5 L Salzburg rivulet water (Steir et al., 2008)
Forstau_P	<.001 ug/g	5.80E-08	1.5 L Salzburg rivulet water (Steir et al., 2008)
Forstau_R	<.001 ug/g	1.14E-07	1.5 L Salzburg rivulet water (Steir et al., 2008)
Forstau_T	0.003 ug/g	4.00E-08	1.5 L Salzburg rivulet water (Steir et al., 2008)
Gastein 1	0.1 ug/g	6.50E-12	2.5 L subsurface well water, Bad Gastein (Steir et al., 2008)
Gastein 2A	0.1 ug/g	6.20E-12	2.5 L subsurface well water, Bad Gastein (Steir et al., 2008)
Gastein 2B	0.1 ug/g	7.00E-12	2.5 L subsurface well water, Bad Gastein (Steir et al., 2008)
123 (piezo)		4.66E-05	contaminated waters near Chemical Processing Plant at Idaho National Laboratories (Zhao et al. 1997)
45 (piezo)		1.45E-05	contaminated waters near Chemical Processing Plant at Idaho National Laboratories (Zhao et al. 1997)
CFA-1		8.21E-07	contaminated waters near Chemical Processing Plant at Idaho National Laboratories (Zhao et al. 1997)
108			contaminated waters near Chemical Processing Plant at Idaho National Laboratories (Zhao et al. 1997)
Natural U ores			
Sample#	**U**	**U236/U238**	**Comments**
			(average of 2 samples and maximum value indicated value here; cf Hotchkis et al, 2000)
NIST 4321C	0.085 mg	9.50E-09	ore from Jakimov, Czech Republic (Steir, 2008); Pu and U information from Wicken et al 2008
ANU-0102	147000 ug/g	4.83E-11	ore from Val Redena, Italy (cf Steir et al., 2008); Pu and U information from Wicken et al 2008
ANU-099	203000 ug/g	1.23E-11	unknown origin (Steir et al., 2008); Pu and U information from Wicken et al 2008
ANU-267	426000 ug/g	6.04E-11	20 wt% U (Berkovits et al. 2000)
Schwartzwalder (USA)	200000 ug/g	1.20E-11	79 wt% U (Berkovits et al. 2000)
Osamu Utsumi (Brazil)	790000 ug/g	1.80E-11	48 wt% U (Berkovits et al. 2000)
Joachimsthal (Bohemia)a	480000 ug/g	7.30E-11	50 wt% U (Berkovits et al. 2000)
Joachimsthal (Bohemia)	500000 ug/g	3.30E-10	63 wt% U (Berkovits et al. 2000)
Cigar Lake (Canada)	630000 ug/g	3.30E-10	14% U assumed in the measurement (Zhao et al. 1994)
Cigar Lake (Canada)	140000 ug/g	5.60E-10	from Wilcken et al. 2008
ANU104 (Radium Hill Aus; Davidite)	17800 ug/g	1.02E-11	from Wilcken et al. 2008
ANU103 (Billeroo Prospect Aus; davidite)	19900 ug/g	1.03E-12	from Wilcken et al. 2008
ANU094 (val Vadello ITA; pitch)	20400 ug/g	8.20E-12	from Wilcken et al. 2008
ANU093 (Bergamnon ITA; pitch)	24600 ug/g	8.14E-11	from Wilcken et al. 2008
ANU105 (Radium Hill Aus; davidite/carnotite)	28500 ug/g	1.35E-12	from Wilcken et al. 2008
ANU101 (Novo-mesto Czech; pitch)	372000 ug/g	6.55E-11	from Wilcken et al. 2008
ANU108 (Oklo zone 9 Gabon)	679000 ug/g	1.80E-10	from Wilcken et al. 2008
ANU097 (Nabarlek, Aus)	692000 ug/g	2.29E-10	from Wilcken et al. 2008
ANU109 (Oklo Zone 9 Gabon)	706000 ug/g	1.53E-10	from Wilcken et al. 2008
AMU096 (Zambia; Pitch)	745000 ug/g	6.05E-11	from Murphy et al., 2015
PRC015-23	173 ug/g	2.63E-12	from Murphy et al., 2015
PRC015-24	24200 ug/g	1.57E-12	from Murphy et al., 2015
PRC015-25	2253 ug/g	2.43E-12	from Murphy et al., 2015
PRC023-15	895 ug/g	3.64E-12	from Murphy et al., 2015
PRC023-16	4797 ug/g	3.85E-12	from Murphy et al., 2015
PRC023-19	403 ug/g	3.24E-12	from Murphy et al., 2015
PRC019-03	610 ug/g	1.41E-12	from Murphy et al., 2015
PRC021-11	7876 ug/g	9.09E-12	from Murphy et al., 2015
PRC021-12	78.9 ug/g	5.58E-12	
U Mill extractions			
Sample#	**U**	**U236/U238**	**Comments**
Vienna-KkU	500000 ug/g	6.98E-11	uranyl nitrate (Uranfabrik Joachimsthal) U Vienna (Steir et al., 2008)
U3O8 MB		5.25E-11	U3O8 (Uranfabrik Joachimsthal) stored at TU Wein (Steir et al., 2008)
Kk-Yranylacetat		9.50E-11	(Steir et al., 2008)
Lot2061		6.05E-10	yellowcake (Steir et al., 2008)
Lot2063		4.65E-11	yellowcake (Steir et al., 2008)
BL-5	70900	2.42E-10	(Beaverlodge mill concentrate of ~ 7%; cf Wicken et al. 2008)

Annex B: Elemental composition and analyses

Table B - 1: Samples collected at Cigar Lake with description and emplacement and elemental composition as analyzed at Saskatchewan Research Center (SRC)

Sample ID	hole ID	Depth (m)	Description	U (ppm)	B (ppm)	Gd (ppm)	Sm (ppm)
CL-M-01	SF-747-08	282.8	sandstone w/ visible structures	555	12	1.17	1.23
CL-M-02	SF-747-08	283.7	mineralization, sharp contacts, locally porous w/ inclusions of sand. (from 283-285.3)	4900	20	2.63	2.74
CL-M-03	SF-747-08	286	sandstone w/ visible structures	404	28	1.36	1.78
CL-M-04	SF-747-04	141.5	fractured sandstone	1450	13	0.55	0.73
CL-M-05	SF-747-04	141.8	grainy crumbly dark mineralization w/ clear contact below 141.7 to 142.1m	6730	40	0.94	1.13
CL-M-06	SF-747-04	142.4	sandstone, heavy hem staining, clear contact w/ min	1020	26	0.63	0.83
CL-M-07	SF-737-10	416.7	sandstone increase in hematite stain.	13	127	1.4	1.7
CL-M-08	SF-737-10	418.4	silicified sandstone, hematite staining (beginning of hem cap)	81.5	115	3.8	4.4
CL-M-09	SF-737-10	402.6	sandstone w/ large amount of clay	26.4	69	7.2	7.8
CL-M-10	SF-737-10	445.4	basement rock, metapelites, very strained sphalerite visible	7.04	158	4.5	4.5
CL-M-11	SF-737-10	446	basement rock, metapelites, very strained sphalerite visible	4.9	192	4.5	5.5

CL-M-12	SF-737-10	449	basement rock, metapelites, very strained sphalerite visible	3.81	250	6.9	7.6
CL-M-13	CL 353	341.3	dark, weathered and strained. (340 -341.5)	3220	51	4	4
CL-M-14	CL 353	122.7	unfractured sandstone, visible structures, local hematite	5.6	23	1.2	1.5
CL-M-16	CL 353	284.5	fracture in sandstone w/ dark material on the fault plain	58.4	32	3	4.1
CL-M-17	CL 353	441.5	basement rock, metapelites, very strained	32.5	382	5	4.4
CL-M-18	CL 353	149.6	sandstone visible structure and hem laminations	146	62	5.1	4.1
CL-M-19	CL 353	173.2	sandstone w/ sharp contact of intense hem staining	7.16	51	2.6	2.4
CL-M-20	CL 353	188.6	fractured sandstone w/ brittle plains and dissilicified material	35.8	50	1.6	1.8
CL-M-22	CL 353	161.5	silicified sandstone	5.56	35	1.6	1.8
CL-M-23	CL 353	393.5	sandstone, locally dicilissified high clay content.	65.9	40	1.5	1.8
CL-M-24	CL 353	139	silicified sandstone w/ oxidation	8.33	32	1.2	1.5
CL-M-25	CL 353	419.6	sandstone w/ darker large grains, oxidized and weathered	279	124	1.6	1.9
CL-M-27	SF-844-12	286.5	sandstone with visible structure light hem staining and oxidation	43.9	41	3	3.2
CL-M-28	SF-844-12	314.3	sandstone with visible structure light hem staining and oxidation	125	41	13.3	15.1
CL-M-29	SF-844-12	162	fracture in sandstone w/ dark material on the fault plain	189	38	10.1	9.4

CL-M-30	SF-844-12	202.75	dissilicified sandstone, heavy clay	23.9	21	2.2	2.4
CL-M-31	SF-844-12	361.8	min in fracture, locally disilicified weathered	162	39	0.8	1
CL-M-33	SF-844-12	146	sandstone visible structure and hem laminations	73.3	139	7	6.8
CL-M-34	SF-844-12	244.6	sandstone, darker in color, with hem staining	86	31	3.9	4.2
CL-M-35	SF-844-12	259.9	sandstone w/ visible structures	27.2	32	2.3	2.6
CL-M-36	CL 345	130.4	fracture in sandstone w/ drark material on the fault plain	2.39	19	1.4	1.6
CL-M-37	CL 346	116	sandstone visible structure and hem laminations	3.01	33	1.1	1.2
CL-M-38	CL 367	192	sandstone, with hem staining local oxidation	3.94	23	1.9	1.9
CL-M-39	CL 07-271A	50.1	sandstone	1.77	13	0.7	0.8
CL-M-40	SF-737-10	429.6	mineralization silicified (min from 423.8 - 433.4)	662000	348	177	35.7
CL-M-41/ CL-M-42	SF-737-10	424.1	top of ore (main mineralization) vary dark (min from 423.8 - 433.4)	34000	743	34.2	22.1
CL-M-43	SF-737-10	432.9	ore in basement at the unconformity (unconformity at 432.1m) (min from 423.8 - 433.4)	114000	1400	226	159
CL-M-44/ CL-M-45	SF-737-10	428	mineralization, very dark (min from 423.8 - 433.4)	240	924	9.03	11.8
CL-M-46/ CL-M-47	SF-737-08	284.8	mineralization, locally porous	26900	12	3.18	3.64
CL-M-48	SF-737-08	280.3	mineralization, locally porous w/ inclusions of sand. (278-281)	37200	32	9.28	7.3

CL-M-49	SF-737-08	280.7	mineralization, locally porous w/ inclusions of sand. (278-281)	75100	44	10.1	9.74
CL-M-50	CL 07-271A	110.1	sandstone	5.91	42	1.2	1.3
CL-M-51	CL 07-271A	318	sandstone visible structure high hem staining	3.78	17	1	1.3
CL-M-52	CL 07-271A	162.1	sandstone	7.22	31	1.8	1.8
CL-M-53	CL 07-271A	235.2	fracture in sandstone w/ dark material on the fault plain	20.4	55	1.3	1.6
CL-M-54	CL 367	110.6	sandstone visible structure and hem laminations	3.57	8	0.8	1
CL-M-55	CL 367	167	sandstone visible structure and hem laminations	3.98	32	1.3	1.4
CL-M-56	CL 345	227.7	sandstone visible structure high hem staining	1.25	25	1	1.2
CL-M-57	CL 345	347	sandstone visible structure high hem staining (rock is dark red) end in sharp contacts	0.9	10	1.5	1.9
CL-M-58	CL 345	409	coarse grain sandstone w/ local sharp and intense hem staining	0.64	11	1.6	1.6
CL-M-59	CL 345	175	sandstone w/ hem laminations	4.88	50	2.6	3.1
CL-M-60	CL 346	183	sandstone unfractured	1.85	47	2	2.3

Table B - 2: Results of the prediction model

Sample ID	^{236}U (atoms/g)	$^{236}U/^{238}U$ (atom/atom)	^{238}U (atoms/g)
CL-M-01	1.139E+09	8.172E-10	1.394E+18
CL-M-02	6.151E+09	4.998E-10	1.231E+19
CL-M-03	4.209E+08	4.148E-10	1.015E+18
CL-M-04	3.372E+09	9.259E-10	3.642E+18
CL-M-05	6.566E+09	3.885E-10	1.690E+19
CL-M-06	1.287E+09	5.023E-10	2.562E+18
CL-M-07	3.463E+06	1.061E-10	3.265E+16
CL-M-08	2.186E+07	1.068E-10	2.047E+17
CL-M-09	9.117E+06	1.375E-10	6.630E+16
CL-M-10	1.400E+06	7.916E-11	1.768E+16
CL-M-11	8.167E+05	6.636E-11	1.231E+16
CL-M-12	4.798E+05	5.014E-11	9.569E+15
CL-M-13	1.840E+09	2.275E-10	8.087E+18
CL-M-14	6.924E+06	4.923E-10	1.406E+16
CL-M-16	4.462E+07	3.042E-10	1.467E+17
CL-M-17	2.860E+06	3.504E-11	8.162E+16
CL-M-18	6.116E+07	1.668E-10	3.667E+17
CL-M-19	4.039E+06	2.246E-10	1.798E+16
CL-M-20	2.215E+07	2.463E-10	8.991E+16
CL-M-22	4.644E+06	3.326E-10	1.396E+16

CL-M-23	4.981E+07	3.010E-10	1.655E+17
CL-M-24	7.848E+06	3.751E-10	2.092E+16
CL-M-25	7.631E+07	1.089E-10	7.007E+17
CL-M-27	2.835E+07	2.571E-10	1.103E+17
CL-M-28	4.277E+07	1.362E-10	3.139E+17
CL-M-29	7.957E+07	1.676E-10	4.747E+17
CL-M-30	2.707E+07	4.509E-10	6.002E+16
CL-M-31	1.353E+08	3.326E-10	4.069E+17
CL-M-33	1.524E+07	8.276E-11	1.841E+17
CL-M-34	6.203E+07	2.872E-10	2.160E+17
CL-M-35	2.255E+07	3.301E-10	6.831E+16
CL-M-36	3.312E+06	5.518E-10	6.002E+15
CL-M-37	2.804E+06	3.709E-10	7.559E+15
CL-M-38	4.392E+06	4.439E-10	9.895E+15
CL-M-39	3.856E+06	8.673E-10	4.445E+15
CL-M-40	5.145E+11	3.095E-10	1.663E+21
CL-M-41/ CL-M-42	3.324E+09	3.892E-11	8.539E+19
CL-M-43	9.900E+09	3.458E-11	2.863E+20
CL-M-44/ CL-M-45	8.923E+06	1.480E-11	6.027E+17
CL-M-46/ CL-M-47	5.437E+10	8.047E-10	6.756E+19
CL-M-48	3.877E+10	4.150E-10	9.343E+19
CL-M-49	9.388E+10	4.977E-10	1.886E+20
CL-M-50	4.413E+06	2.973E-10	1.484E+16

CL-M-51	6.157E+06	6.485E-10	9.493E+15
CL-M-52	6.515E+06	3.593E-10	1.813E+16
CL-M-53	1.186E+07	2.316E-10	5.123E+16
CL-M-54	1.071E+07	1.194E-09	8.966E+15
CL-M-55	3.713E+06	3.715E-10	9.995E+15
CL-M-56	1.493E+06	4.756E-10	3.139E+15
CL-M-57	1.855E+06	8.208E-10	2.260E+15
CL-M-58	1.230E+06	7.650E-10	1.607E+15
CL-M-59	2.781E+06	2.269E-10	1.226E+16
CL-M-60	1.165E+06	2.507E-10	4.646E+15

Table B - 3: Counts and $^{236}U/^{238}U$ ratio measruments

		^{233}U NET	^{233}U, ^{236}U counts					Note
	Amount sample digist	fg/mg	^{233}U	^{236}U	^{233}U	^{236}U	$^{236}U/^{238}U$	
Sample ID	g	Oxide	counts	counts	live time	live time	atom/atom	
CL-M-01a	10.02	10.45	49	24	9.709	19.417	3.09E-12	eliminated due to low count
CL-M-01b	13.94	23.47	435	259	9.709	19.417	5.10E-11	
CL-M-02a	10.2	7.11	39	99	9.709	19.417	7.72E-12	eliminated due to low count
CL-M-02b	10.07	2.41	0	18	9.709	19.417	9.22E-12	eliminated due to low count
CL-M-03a	10.26	10.82	16	27	9.709	19.417	2.38E-11	eliminated due to low count
CL-M-03b	10.25	118.5	10770	464	9.709	19.417	5.83E-12	
CL-M-04a	10.06	15.64	19	13	9.709	19.417	5.78E-12	eliminated due to low count
CL-M-04b	10.2	11.23	16	16	9.709	19.417	5.68E-12	eliminated due to low count
CL-M-05a	3.665	88.38	144	19	9.709	19.417	4.88E-12	eliminated due to low count
CL-M-05b	2.86	50.26	28	6	9.709	19.417	3.24E-12	eliminated due to low count
CL-M-06a	10	16.07	32	61	9.709	19.417	3.32E-11	eliminated due to low count
CL-M-06b	10.22	16.19	34	25	9.709	19.417	8.30E-12	eliminated due to low count
CL-M-07	11.18	22.98	397	16	9.709	19.417	1.30E-11	eliminated due to low count
CL-M-08	12.67	111.6	7278	144	9.709	19.417	1.06E-11	
CL-M-09	10.67	114.6	15289	124	9.709	19.417	1.62E-11	
CL-M-10	11.3	21.5	3138	108	9.709	19.417	4.76E-11	
CL-M-11	12.7	22.6	1954	87	9.709	19.417	7.93E-11	eliminated due to low count
CL-M-12	10.62	120.08	1406	17746	9.709	19.417	6.68E-08	
CL-M-13	5.533	17.69	6	58	9.709	19.417	2.58E-11	eliminated due to low count
CL-M-14	99.97	93.1	20318	960	9.709	19.417	4.43E-11	
CL-M-15	14.17	18.56	24	405	9.709	19.417	3.10E-10	
CL-M-16	10.17	104.7	11094	349	9.709	19.417	2.92E-11	
CL-M-17	10.11	109.03	364	8	9.709	19.417	1.50E-11	eliminated due to low count
CL-M-18	13.86	16.1	776	341	9.709	19.417	2.38E-11	
CL-M-19	10.75	21.47	364	7	9.709	19.417	1.79E-10	eliminated due to low count
CL-M-20	13.23	18.9	1091	318	9.709	19.417	6.81E-11	
CL-M-22	10.81	22.02	591	9113	9.709	19.417	1.79E-08	
CL-M-23	12.45	120.51	175	1	9.709	19.417	1.73E-12	eliminated due to low count
CL-M-24	12.48	109.56	807	43	9.709	19.417	1.08E-10	eliminated due to low count
CL-M-25	4.781	70.88	39	6	9.709	19.417	3.05E-12	eliminated due to low count
CL-M-26	4.82	38.97	354	728	9.709	19.417	9.40E-09	
CL-M-27	101.97	UNKNOWN	796	69	9.709	19.417	1.71E-11	Spilled eliminated due to low count
CL-M-27i*	100	103.6	3470	64	9.709	19.417		composite sample, mix of 21 and 27
CL-M-28	10.03	20.60	375	165	9.709	19.417	2.60E-11	
CL-M-29	10.6	17.83	67	41	9.709	19.417	1.28E-11	eliminated due to low count
CL-M-30	10.7	20.36	250	4002	9.709	19.417	1.51E-09	
CL-M-31	4.795	129.81	197	5	9.709	19.417	3.83E-12	eliminated due to low count
CL-M-32	10.5	57.26	559	19	9.709	19.417	8.24E-12	eliminated due to low count
CL-M-33	10.51	94.37	686	20	9.709	19.417	1.15E-11	eliminated due to low count
CL-M-34	10.53	25.10	246	4	9.709	19.417	1.33E-12	eliminated due to low count
CL-M-35	10.67	21.48	506	550	9.709	19.417	5.20E-10	
CL-M-37	11.65	112.91	2028	43	9.709	19.417	2.70E-10	eliminated due to low count
CL-M-38	6.44	82.81	2251	1029	9.709	19.417	1.86E-08	
CL-M-39	10.47	21.18	485	7	9.709	19.417	5.90E-12	eliminated due to low count
CL-M-40	1.442	4.91	1	1385	9.709	19.417	3.01E-10	
CL-M-41	1.03	13.29	3	21	9.709	19.417	1.10E-11	eliminated due to low count
CL-M-42	1.025	17.45	10	28	9.709	19.417	7.49E-12	eliminated due to low count
CL-M-43	1.442	96.53	74	58	9.709	19.417	7.76E-11	eliminated due to low count
CL-M-44	1.042	6.57	6	97	9.709	19.417	5.19E-11	eliminated due to low count
CL-M-45	1.482	4.24	2	202	9.709	19.417	1.05E-10	
CL-M-46	3.002	4.23	0	59	9.709	19.417	3.49E-11	eliminated due to low count
CL-M-47	2.9	13.82	5	52	9.709	19.417	1.57E-11	eliminated due to low count
CL-M-48	6.5	60.02	22	110	9.709	19.417	1.10E-10	
CL-M-49	5.785	56.70	29	24	9.709	19.417	1.64E-11	eliminated due to low count
CL-M-50	8.73	68.12	2510	212	9.709	19.417	6.35E-11	
CL-M-51	100.13	9.7	250	190	9.709	19.417	1.12E-09	
CL-M-52	101.96	10.2	213	448	9.709	19.417	1.21E-09	
CL-M-55	100.53	9.9	3529	468	9.709	19.417	1.49E-10	
CL-M-56	99.86	130.5	188291	704	9.709	19.417	1.61E-11	
CL-M-57	100.13	9.4	2904	488	9.709	19.417	8.07E-10	
CL-M-58	100.15	9.7	4916	269	9.709	19.417	3.14E-10	
CL-M-59	11.67	101.4	11149	42	9.709	19.417	3.66E-11	eliminated due to low count
CL-M-60	10.92	123.1	12469	116	9.709	19.417	2.54E-10	

Table B - 1: Complete results Table, Complementary to Table 8-1 and Table 8-2

					SRC Analyses			AMS results						Model results		
Grade	Sample ID	Sample info	hole ID	Depth (m)	U (ppm)	^{238}U ppm	^{238}U atoms/g	^{236}U atoms/g	error atoms/g	^{236}U/^{238}U atom/atom	error atom/atom	^{236}U (pg/kg)	error (pg/kg)	^{236}U atoms/g	^{236}U/^{238}U atom/atom	^{236}U (pg/kg)
Low Grade (<10ppm)	CL-M-58	unfractioned core, almost ar the surface, sandstone, background levels	CL 345	409	0.64	0.64	1.61E+15	7.68E+05	4.81E+04	4.48E-10	3.35E-11	0.30	0.02	1.23E+06	7.65E-10	0.48
	CL-M-57	unfractioned core, almost ar the surface, sandstone, background levels	CL 345	347	0.9	0.89	2.26E+15	2.25E+06	1.10E+05	9.94E-10	5.35E-11	0.88	0.04	1.86E+06	8.21E-10	0.73
	CL-M-56	unfractioned core, almost ar the surface, sandstone, background levels	CL 345	227.7	1.25	1.24	3.14E+15	5.04E+04	1.90E+03	1.61E-11	6.59E-13	0.02	0.001	1.49E+06	4.76E-10	0.59
	CL-M-60	sandstone away from minalization, low background levels	CL 346	183	1.85	1.82	4.60E+15	1.18E+06	1.10E+05	2.57E-10	2.39E-11	0.46	0.04	1.16E+06	2.51E-10	0.46
	CL-M-51	sandstone away from minalization, low background levels	CL-07-271A	318	3.78	3.75	9.49E+15	1.07E+07	1.03E+06	1.12E-09	1.08E-10	4.18	0.40	6.16E+06	6.48E-10	2.41
	CL-M-12	alteration halo, below main mineralization, low grade	SF-737-10	449	3.81	3.78	9.57E+15	6.39E+08	8.17E+06	6.68E-08	5.01E-10	250.36	3.20	4.80E+05	5.01E-11	0.19
	CL-M-38	unfractioned core, almost ar the surface, sandstone, background levels	CL 367	192	3.94	3.91	9.90E+15	4.77E+07	2.55E+07	1.86E-08	5.80E-10	18.68	0.70	4.39E+06	4.44E-10	1.72
	CL-M-55	sandstone away from minalization, low background levels	CL 367	167	3.98	3.95	1.00E+16	1.85E+06	9.12E+04	1.86E-10	9.17E-12	0.73	0.03	3.71E+06	3.71E-10	1.46
	CL-M-22	sandstone away from minalization, low background levels	CL 353	161.5	5.56	5.52	1.40E+16	2.49E+08	3.52E+06	1.79E-08	2.72E-09	97.75	1.38	4.64E+06	3.33E-10	1.82
	CL-M-14	sandstone away from minalization, low background levels	CL 353	122.7	5.60	5.56	1.41E+16	6.23E+05	2.06E+04	4.43E-11	1.47E-12	0.24	0.01	6.92E+06	4.92E-10	2.71
	CL-M-50	perched mineralization in core way from deposit	CL-07-271A	110.1	5.91	5.87	1.48E+16	9.43E+05	2.42E+05	6.35E-11	4.35E-12	0.37	0.03	4.41E+06	2.97E-10	1.73
	CL-M-10	alteration halo, below main mineralization, low grade	SF-737-10	445.4	7.04	6.99	1.77E+16	8.42E+05	8.24E+04	4.76E-11	4.66E-12	0.33	0.03	1.40E+06	7.92E-11	0.55
	CL-M-52	sandstone away from minalization, low background levels	CL-07-271A	162.1	7.22	7.17	1.81E+16	2.76E+07	2.30E+06	1.52E-09	1.27E-10	10.82	0.90	6.51E+06	3.59E-10	2.55
Medium Grade (10ppm to 200ppm)	CL-M-30	alteration halo, above main mineralization, mid grade	SF-844-12	202.75	23.90	23.73	6.00E+16	9.04E+07	1.51E+06	1.51E-09	2.38E-11	35.44	0.59	2.71E+07	4.51E-10	10.61
	CL-M-09	alteration halo, above main mineralization, mid grade	SF-737-10	402.6	26.40	26.21	6.63E+16	1.08E+06	9.71E+04	1.62E-11	1.46E-12	0.42	0.04	9.12E+06	1.38E-10	3.57
	CL-M-35	Sandstone, above mineralization, lower mid-grade	SF-844-12	259.9	27.20	8.27	6.83E+16	1.96E+06	8.67E+05	5.20E-10	2.22E-11	5.52	0.34	2.26E+07	3.30E-10	8.84
	CL-M-20	Sandstone, above mineralization, lower mid-grade	CL 353	188.6	35.80	35.54	8.99E+16	6.12E+06	3.90E+05	6.81E-11	4.34E-12	2.40	0.15	2.21E+07	2.46E-10	8.68
	CL-M-16	alteration halo, below main mineralization, mid grade	CL 353	284.5	58.40	57.98	1.47E+17	4.29E+06	2.33E+05	2.92E-11	1.59E-12	1.68	0.09	4.46E+07	3.04E-10	17.49
	CL-M-08	Sandstone, above mineralization, mid-grade	SF-737-10	418.4	81.50	80.91	2.05E+17	2.18E+06	1.83E+05	1.06E-11	8.96E-13	0.85	0.07	2.19E+07	1.07E-10	8.57
	CL-M-28	Sandstone, above mineralization, lower mid-grade	SF-844-12	314.3	125.00	124.10	3.14E+17	8.16E+06	6.37E+05	2.60E-11	2.02E-12	3.20	0.25	4.28E+07	1.36E-10	16.76
	CL-M-18	Sandstone, above mineralization, mid-grade	SF-844-12	149.6	146.00	144.95	3.67E+17	8.72E+06	5.67E+05	2.38E-11	1.54E-12	3.42	0.22	6.12E+07	1.67E-10	23.97
High Grade (>200ppm)	CL-M-45	ore	SF-737-10	428	240.00	238.27	6.03E+17	6.32E+07	4.46E+06	1.05E-10	7.38E-12	24.79	1.75	8.92E+06	1.48E-11	3.50
	CL-M-03b	alteration halo above of perched mineralization, high grade sample	SF-747-08	286	404.00	401.09	1.01E+18	5.91E+06	4.42E+06	5.83E-12	2.76E-13	2.32	1.73	4.21E+08	4.15E-10	164.96
	CL-M-01b	alteration halo above of perched mineralization, high grade sample	SF-747-08	282.8	555.00	551.00	1.39E+18	6.06E+06	2.80E+05	5.10E-11	3.17E-12	2.38	0.11	1.14E+09	8.17E-10	446.48
	CL-M-48	ore, high grade perched	SF-747-08	280.3	37200.00	36932.16	9.34E+19	1.03E+10	9.80E+08	7.10E-11	1.05E-11	4028.32	384.09	3.88E+10	4.15E-10	15195.43
	CL-M-40	ore, high grade	SF-737-10	429.6	662000.00	657233.60	1.66E+21	5.01E+11	1.35E+10	3.01E-10	8.10E-12	196369.39	5276.54	5.14E+11	3.09E-10	201660.78

Annex C : Tunning setup

Table C- 1 : $^{236}UO^{-} \rightarrow {}^{236}U^{+3}$ SSI Run

Common	Setting	Date	Last: (2016-05-24)
Tuning target	(U)Fe_2O_3+Si (1:2 wt); Or Cu-pin	SO-110 Y-steerer	235 → 235
Pilot tuning beam and record	$^{238}U^{16}O^{-} \rightarrow {}^{238}U^{+3}$; Or $^{235}U^{16}O^{-} \rightarrow {}^{235}U^{+3}$	LE X1-steerer	271.7
Tuning bouncer DC voltage (V)	349; 772	LE X2-sterer	-47.0
Spike Isotope	^{233}U, ^{238}U	LE Y1-steerer	10.0
Cs (°C) and V_{tgt}/V_{ext}	IC=18A, 110°C and 7/28	LE Y2-sterer	40.2
Quick-cool setting	Off	HE X1-steerer	699
Terminal voltage (kV)	2500; Or 2532.58	HE X2-sterer	-1769
Stripper pressure (mBar)	1.5e-2	HE Y1-steerer	1277
Slit-Err Cup Selection (In or Out)	n/a	HE Y2-sterer	-1236
GIC pressure (mBar)	10.00	EA1 (kV)	3.956
dE amplifier gain	20-12.00	MA1 (current A)	148.916
Ef amplifier gain	40-12.00	MA1 (field Tesla)	0.788060*(+10)*
LE off-axis in-cup (left) - Position	n/a	MA2 (current A)	208.069
LE off-axis out-cup (right) - Position	n/a	MA2 (field Tesla)	1.145580
HE off-axis in-cup (left) - Position	n/a	EA2 (kV)	78.886 ($^{235}U^{+3}$)
HE off-axis out-cup (right) - Position	034.9 for $^{238}U^{+3}$ FC	MA3 (current A)	135.124
LE off-axis in-cup (left) - Range	n/a	SO-110 Lens (kV)	10.85 → 10.00
LE off-axis out-cup (right) - Range	n/a	BI Lens (kV)	26.264 → 26.381
HE off-axis in-cup (left) - Range	n/a	ACC Lens (kV)	59.95
HE off-axis out-cup (right) - Range	100nA	ACC Q-Pole focus (%)	49.30
Slits at MA1 object plane	1.00 / 1.00	ACC Q-Pole astigmatism (%)	-0.38
Aperture at MA1 object plane	Out	HE Q-Pole focus (%)	38.50
Slits at MA1 focal plane	1.00 / 1.00	HE Q-Pole astigmatism (%)	0.70
Aperture at MA1 focal plane	Out	RI Foil Q-Pole focus (%)	0
Slits at MA2 object plane	0.75 / 0.75	RI Foil Q-Pole astigmatism (%)	0
Aperture at MA2 object plane	In	RI ESA Q-Pole focus (%)	40.0
Aperture at MA2 exit	In	RI ESA Q-Pole astigmatism (%)	5.5
Slits at MA2 focal plane	0.75 / 0.75		
Aperture at MA2 focal plane	In	GIC/RI/ACC/BI/SO-110	1.37/1.50/6.77/5.88/8.62
Slits at EA2 exit	**0.50 / 0.50** **(E/ΔE > 500 with FW10%M)**		
Slits at GIC	**1.25 / 1.25**		

Major Steps

1. Tune $^{238}U^{16}O^{-} \rightarrow {}^{238}U^{+3}$ to MA2 with all steering and focusing
2. Tune to GIC FC with rest first (MA3 manual only), then with SO-110 Y-steerer and LE lenses
3. Record transmission, save settings for $^{238}U^{16}O^{-} \rightarrow {}^{238}U^{+3}$, and calculate for other isotopes
4. On a Cu-pin target, record new MPA using $^{235}U^{16}O^{-} \rightarrow {}^{235}U^{+3}$; Or skip Step 1-3, start here directly
5. Optional, tune V_T for off-axis cup beams if necessary, open 888 meter
6. Optional, scan EA2 covering wide scatter tails for $^{233}U^{+3}$ and $^{236}U^{+3}$ for final determination and background assessment
7. Set all parameter files and start the run with the spike isotope first, with 2 blocks for first pass
8. Starting 2nd pass, cycle with 10 blocks (10.0 minutes) per pass, in order of $^{233}U^{+3}$ (10s), $^{236}U^{+3}$ (20s), $^{238}U^{+3}$ (current); Or cycle with 10 blocks (12.75 minutes) per pass, in order of $^{233}U^{+3}$ (20s), $^{236}U^{+3}$ (20s), $^{234}U^{+3}$ (10s)
9. If ionizer gets poisoned badly, increase Cs reservoir temperature to 120°C; go back as soon as it starts recovering
10. After ionizer recovery, must retune MA1&2, SO-110 Y-steerer and LE lenses

References

Alexandre, P., Kyser, K., Jiricka, D., 2009. Critical geochemical and mineralogical factors for the formation of unconformity-related uranium deposits:Comparison between barren and mineralized systems in the athabasca basin, Canada. Econ. Geol. 104, 413–435. doi:10.2113/gsecongeo.104.3.413

Berkovits, D., Feldstein, H., Ghelberg, S., Hershkowitz, A., Navon, E., Paul, M., 2000. 236U in uranium minerals and standards. Nucl. Instrum. Methods Phys. Res. Sect. B Beam Interact. Mater. At., 8th International Conference on Accelerator Mass Spectrometry 172, 372–376. doi:10.1016/S0168-583X(00)00152-X

Berman, R.G., Ryan, J.J., Tella, S., Sanborn-Barrie, M., Stern, R.A., Aspler, L., Hanmer, S., Davis, W.J., 2000. The case of multiple metamorphic events in the Western Churchill Province: evidence from linked thermobarometric and in-situ SHRIMP data, and jury deliberations, in: GeoCanada 2000: The Millennium Geoscience Summit. Presented at the Joint Meeting of the Canadian Geophysical Union, Canadian Society of Exploration Geophysicists, Canadian Society of Petroleum Geologists, Canadian Well Logging Society, Geological Association of Canada, and the Mineralogical Association of Canada, Calgary, Alberta, Canada.

Bishop, C.S., Mainville, A.G., Yesnik, L.D., 2016. Cigar Lake Operation, Northern Saskatchewan, Canada; National Instrument 43-101 Technical report.

Boiron, M.-C., Cathelineau, M., Richard, A., 2010. Fluid flows and metal deposition near basement cover unconformity: Lessons and analogies from Pb-Zn-F-Ba systems for the understanding of Proterozoic U deposits. Geofluids 10, 270–292. doi:10.1111/j.1468-8123.2010.00289.x

Briesmeister, J., 1986. MCNP—A general purpose Monte Carlo code for neutron and photon transport, Version 3A, Los Alamos National Laboratory Report LA-7396-M. Los Alamos, NM.

Bruneton, P., 1993. Geological environment of the Cigar Lake uranium deposit. Can. J. Earth Sci. 30, 653–673.

Bruneton, P., 1987. Geology of the Cigar Lake Uranium Deposit (Saskatchewan, Canada). Econ. Miner. Sask. 99–119.

Card, C.D., Pana, D., Portella, P., Thomas, D.J., Annesley, I., 2007. Basement rocks to the Athabasca Basin, Saskatchewan and Alberta. EXTECH IV Geol. Uranium Explor. Technol. Proterozoic Athabasca Basin Sask. Alta. Ed CW Jefferson G Delaney Geol. Surv. Can. Bull. 588 P 69–87 Also Sask. Geol. Soc. Spec. Publ. 18 Geol. Assoc. Can. Miner. Depos. Div. Spec. Publ. 4 69–87.

Cornett, R.J., Fabryka-Martin, J., Cramer, J.J., Andrew, H.R., Koslowsky, V.T., 2010. 36Cl production and mobility in the Cigar Lake uranium deposit. Nucl. Inst Methods Phys. Res. B 268, 1189–1192. doi:10.1016/j.nimb.2009.10.130

Cornett, R.J., Cramer, J., Andrews, H.R., Chant, L.A., Davies, W., Greiner, B.F., Imahori, Y., Koslowsky, V., McKay, J., Milton, G.M., Milton, J.C.D., 1996. In situ production of 36Cl in uranium ore: A hydrogeological assessment tool. Water Resour. Res. 32, 1511–1518. doi:10.1029/95WR03821

Cramer, J.J., 1986. Sandstone-hosted uranium deposits in northern Saskatchewan as natural analogs to nuclear fuel waste disposal vaults. Chem. Geol. 55, 269–279. doi:10.1016/0009-2541(86)90029-X

Cumming, G.L., Krstic, D., 1992. The age of unconformity-related uranium mineralization in the Athabasca Basin, northern Saskatchewan. Can. J. Earth Sci. 29, 1623–1639.

Curtis, D., Fabryka-Martin, J., Dixon, P., Cramer, J., 1999. Nature's uncommon elements: plutonium and technetium. Geochim. Cosmochim. Acta 63, 275–285. doi:10.1016/S0016-7037(98)00282-8

Derome, D., Cathelineau, M., Lhomme, T., Curley, M., 2003. Fluid inclusion evidence of the differential migration of H2 and O2in the McArthur River unconformity-type uranium deposit (Saskatchewan, Canada). Possible role on post-ore modifications of the host rocks. J. Geochem. Explor. 78–79, 525–530. doi:10.1016/S0375-6742(03)00114-6

Ensslin, N., 1991. The Origin of Neutron Radiation, in: Passive Non-Destructive Assay of Nuclear Materials, NUREG/CR-5550. Nuclear Regulatory Commission, pp. 337–356.

Fabryka-Martin, J., 1988. Production of Radionuclides in the earth and their hydrogeologic significance, with emphasis on chlorine-36 and iodine-129 (Ph.D.). University of Arizona, Arizona.

Fabryka-Martin, J., Curtis, D.B., 1993. Geochemistry of 239Pu, 129I, 99Tc amd 36Cl (No. 15), Aligator Rivers Analogu Project Final report. Los Alamos National Laboratory, Los Alamos, New Mexico, Usa.

Fabryka-Martin, J., Curtis, D.B., Dixon, P., Rokop, D.J., Roensch, F., Aguilar, R., Attrep, M., 1994. Natural nuclear pruducts in the Cigar Lake deposit, in: J.J. Cramer and J.A.T. Smellie Final Report of the AECL/SKB Cigar Lake Analog Study, Report AECL-10851, COG-93-147, SKB TR 94-04 Atomic Energy of Canada Limited. Whiteshell Laboratories, Pinawa, Manitoba.

Farquharson, C.G., Craven, J.A., 2009. Three-dimensional inversion of magnetotelluric data for mineral exploration: An example from the McArthur River uranium deposit, Saskatchewan, Canada. J. Appl. Geophys. 68, 450–458. doi:10.1016/j.jappgeo.2008.02.002

Fayek, M., Kyser, T.K., 1997. Characterization of multiple fluid-flow events and rare-earth-element mobility associated with formation of unconformity-type uranium deposits in the Athabasca Basin, Saskatchewan. Can. Mineral. 35, 627–658.

Fouques, J.-P., Fowler, M.G., Knipping, H.D., Schimann, K., 1986. Cigar Lake Uranium Deposit: Discovery and General Characteristics. (Article) [LE GISEMENT D'URANIUM DE CIGAR LAKE: DECOUVERTE ET CARACTERISTIQUES GENERALES.]. CIM Bull. 79, 70–82.

Gaboreau, S., Cuney, M., Quirt, D., Beaufort, D., Patrier, P., Mathieu, R., 2007. Significance of aluminum phosphate-sulfate minerals associated with U unconformity-type deposits: The Athabasca basin, Canada. Am. Mineral. 92, 267–280. doi:10.2138/am.2007.2277

Hanmer, S., 1997. Geology of the Striding-Athabasca mylonite zone, northern Saskatchewan and southeastern district of Mackenzie, Northwest Territories. Bull. - Geol. Surv. Can. 501.

Hecht, L., Cuney, M., 2000. Hydrothermal alteration of monazite in the Precambrian crystalline basement of the Athabasca Basin (Saskatchewan, Canada): implications for the formation of unconformity-related uranium deposits. Miner. Deposita 35, 0791–0795.

Hoeve, J., Quirt, D., 1984. Mineralization and Host Rock Alteration in Relation to Clay Mineral Diagenesis and Evolution of the Middle-Proterozoic, Athabasca Basin, Northern Saskatchewan, Canada. Saskatchewan Research Council, SRC Technical Report 187.

Hoffman, P.F., 1988. United plates of America, the birth of a craton: Early Proterozoic assembly and growth of Laurentia. Annu. Rev. Earth Planet. Sci. Vol 16 543–603.

Hotchkis, M.A.., Child, D., Fink, D., Jacobsen, G.., Lee, P.., Mino, N., Smith, A.., Tuniz, C., 2000. Measurement of 236U in environmental media. Nucl. Inst Methods Phys. Res. B 172, 659–665. doi:10.1016/S0168-583X(00)00146-4

IAEA UDEPO [WWW Document], 2017. URL https://infcis.iaea.org/UDEPO/UDEPOMAin.asp?NameFilter=&Region=The%20World&Country=All&Type=All&Status=All&Order=1&Page=1&IncludeSearch=0&RightP=List&Table=1 (accessed 11.30.16).

Jefferson, C.W., Thomas, D.J., Gandhi, S.S., Ramaekers, P., Delaney, G., Brisbin, D., Cutts, C., Portella, P., Olson, R.A., 2007. Unconformity-associated uranium deposits of the Athabasca basin, Saskatchewan and Alberta. Bull. Geol. Surv. Can. 23–67.

Kieser, W.E., Zhao, X.-L., Clark, I.D., Cornett, R.J., Litherland, A.E., Klein, M., Mous, D.J.W., Alary, J.-F., 2015. The André E. Lalonde AMS Laboratory – The new accelerator mass spectrometry facility at the University of Ottawa. Nucl. Inst Methods Phys. Res. B 361, 110–114. doi:10.1016/j.nimb.2015.03.014

Klein, M., Mous, D.J., Gottdang, A., 2004. FAST AND ACCURATE SEQUENTIAL INJECTION AMS WITH GATED FARADAY CUP CURRENT MEASUREMENT. RADIOCARBON 46, 77–82.

Kotzer, T.G., Kyser, T.K., 1995. Petrogenesis of the Proterozoic Athabasca Basin, northern Saskatchewan, Canada, and its relation to diagenesis, hydrothermal uranium mineralization and paleohydrogeology. Chem. Geol. 120, 45–89. doi:10.1016/0009-2541(94)00114-N

Krane, K.S., 1988. Introductory Nuclear Physics, 3rd Edition. ed. John Wiley & Sons.inc.

Mercadier, J., Cuney, M., Cathelineau, M., Lacorde, M., 2011. U redox fronts and kaolinisation in basement-hosted unconformity-related U ores of the Athabasca Basin (Canada): Late U remobilisation by meteoric fluids. Miner. Deposita 46, 105–135. doi:10.1007/s00126-010-0314-7

Mercadier, J., Richard, A., Boiron, M.-C., Cathelineau, M., Cuney, M., 2010. Migration of brines in the basement rocks of the Athabasca Basin through microfracture networks (P-Patch U deposit, Canada). LITHOS 115, 121–136. doi:10.1016/j.lithos.2009.11.010

Mercadier, J., Richard, A., Cathelineau, M., 2012. Boron- and magnesium-rich marine brines at the origin of giant unconformity-related uranium deposits:δ11B evidence from Mg-tourmalines. Geology 40, 231–234. doi:10.1130/G32509.1

Murphy, M.J., Froehlich, M.B., Fifield, L.K., Turner, S.P., Schaefer, B.F., 2015. In-situ production of natural 236U in groundwaters and ores in high-grade uranium deposits. Chem. Geol. 410, 213–222. doi:10.1016/j.chemgeo.2015.06.024

Percival, J.B.M., Bell, K., Torrance, J.K., 1993. Clay mineralogy and isotope geochemistry of the alteration halo at Cigar lake uranium deposit. Can. J. Earth Sci. 30, 689–704.

Philippe, S., Lancelot, J.R., Clauer, N., Pacquet, A., 1993. Formation and evolution of the Cigar Lake uranium deposit based on U- Pb and K-Ar isotope systematics. Can. J. Earth Sci. 30, 720–730.

Ramaekers, P., Jefferson, C.W., Yeo, G.M., Collier, B., Long, D.G.F., Drever, G., McHardy, S., Jiricka, D., Cutts, C., Wheatley, K., Catuneanu, O., Bernier, S., Kupsch, B., Post, R.T., 2007. Revised geological map and stratigraphy of the Athabasca group, Saskatchewan and Alberta. Bull. Geol. Surv. Can. 155–191.

Richard, A., Banks, D., Mercadier, J., Boiron, M.-C., Cuney, M., Cathelineau, M., 2011. An evaporated seawater origin for the ore-forming brines in unconformity-related uranium deposits (Athabasca Basin, Canada): Cl/Br and d37Cl analysis of fluid inclusions. Geochim. Cosmochim. 75, 2791–2810.

Richard, A., Cathelineau, M., Boiron, M.-C., Mercadier, J., Banks, D., Cuney, M., 2016. Metal-rich fluid inclusions provide new insights into unconformity-related U deposits (Athabasca Basin and Basement, Canada). Miner. Deposita 51, 249–270. doi:10.1007/s00126-015-0601-4

Richard, A., Pettke, T., Cathelineau, M., Boiron, M., Mercadier, J., Cuney, M., Derome, D., 2010. Brine-rock interaction in the Athabasca basement (McArthur River U deposit, Canada): Consequences for fluid chemistry and uranium uptake. Terra Nova 22, 303–308. doi:10.1111/j.1365-3121.2010.00947.x

Rokop, D.J., Metta, D.N., Stevens, C.M., 1972. 236U/238U measurements in three terrestrial minerals and one processed ore. Int. J. Mass Spectrom. Ion Phys. 8, 259–264. doi:10.1016/0020-7381(72)83016-X

Rucklidge, J.C., Wilson, G.C., Kilius, L.R., 1990. AMS advances in the geosciences and heavy-element analysis. Nucl. Inst Methods Phys. Res. B 45, 565–569. doi:10.1016/0168-583X(90)90901-6

Sauvé, D.C., 2016. Measurement of 236U, 137Cs, and 129I in the Labrador and Beaufort Seas (M.Sc.). University of Ottawa, Ottawa, Ontario.

Sibbald, T.I.I., 1985. Geology and genesis of the Athabasca basin uranium deposits. Summ. Investig. 1985 Sask. Geol. Surv. Sask. Energy Mines Misc. Rep. 133–156.

Southon, J.R., Nelson, D.E., Vogel, J.S., 1990. Injection systems for AMS: simultaneous versus sequential. Nucl. Inst Methods Phys. Res. B 52, 370–374. doi:10.1016/0168-583X(90)90439-2

Srncik, M., Mayer, K., Hrnecek, E., Wallenius, M., Varga, Z., Steier, P., Wallner, G., 2011. Investigation of the 236U/238U isotope abundance ratio in uranium ores and yellow cake samples. Radiochim. Acta Int. J. Chem. Asp. Nucl. Sci. Technol. 99, 335–339. doi:10.1524/ract.2011.1840

Steier, P., Bichler, M., Keith Fifield, L., Golser, R., Kutschera, W., Priller, A., Quinto, F., Richter, S., Srncik, M., Terrasi, P., Wacker, L., Wallner, A., Wallner, G., Wilcken, K.M., Maria Wild, E., 2008. Natural and anthropogenic 236U in environmental

samples. Nucl. Inst Methods Phys. Res. B 266, 2246–2250. doi:10.1016/j.nimb.2008.03.002

Thomas, D.J., Matthews, R.B., Sopuck, V., 2000. Athabasca Basin (Canada) unconformity - type deposits: Exploration model, current mine developments and exploration directions. Geol. Ore Depos. 2000 Gt. Basin Geol. Soc. Nev. Symp. Reno Nev. May 15-18 2000 Proc. 1, 103–126.

Tran, H.T., 2001. Tectonic evolution of the Paleoproterozoic Wollaston Group in the Cree Lake Zone, northern Saskatchewan, Canada (Ph.D.). University of Regina, Regina, Saskatchewan.

Wilcken, K.M., Barrows, T.T., Fifield, L.K., Tims, S.G., Steier, P., 2007. AMS of natural 236U and 239Pu produced in uranium ores. Nucl. Instrum. Methods Phys. Res. Sect. B Beam Interact. Mater. At., Accelerator Mass SpectrometryProceedings of the Tenth International Conference on Accelerator Mass Spectrometry 259, 727–732. doi:10.1016/j.nimb.2007.01.210

Wilcken, K.M., Fifield, L.K., Barrows, T.T., Tims, S.G., Gladkis, L.G., 2008. Nucleogenic 36Cl, 236U and 239Pu in uranium ores. Nucl. Instrum. Methods Phys. Res. Sect. B Beam Interact. Mater. At. 266, 3614–3624. doi:10.1016/j.nimb.2008.06.009

Yeo, G.M., Delaney, G., 2007. The Wollaston Supergroup, stratigraphy and metallogeny of a Paleoproterozoic Wilson cycle in the Trans-Hudson Orogen, Saskatchewan. EXTECH IV Geol. Uranium Explor. Technol. Proterozoic Athabasca Basin Sask. Alta. Ed CW Jefferson G Delaney Geol. Surv. Can. Bull. 588 P 89–117 Also Sask. Geol. Soc. Spec. Publ. 18 Geol. Assoc. Can. Miner. Depos. Div. Spec. Publ. 4 Bulletin 588, 89–117

Zhao, X.-L., Kilius, L.R., Litherland, A.E., Beasley, T., 1997. AMS measurments of environmental U-236 Preliminary results and perspectives. Nucl. Inst Methods Phys. Res. B 126, 297–300.

Zhao, X.-L., Nadeau, M.-J., Kilius, L.R., Litherland, A.E., 1994. Detection of naturally occurring 236U in uranium ore. Earth Planet. Sci. Lett. 124, 241–244. doi:10.1016/0012-821X(94)00090-5